



# Title

Hamzah Hussain

University College London  
Department of Physics and Astronomy

Submitted to University College London in fulfilment  
of the requirements for the award of the degree of Doctor of Philosophy

Submitted 2020

# Declaration

I, Hamzah Hussain confirm that the work presented in this thesis is my own. Where information has been derived from other sources, I confirm that this has been indicated in the thesis.

# Abstract

# Acknowledgements

# Contents

# List of Figures

# List of Tables



# Chapter 1

## Introduction

Although neutrinos are the most abundant matter particles in the known Universe, their low interaction cross sections have made the neutrino one of the most mysterious particles in the Standard Model (SM) of particle physics. Historically, the Standard Model has been extremely successful at accurately predicting a number of parameters, most recently however, the discovery of neutrino oscillation was beyond any Standard Model prediction for the neutrino. Neutrinos were known to exist in three different flavour eigenstates,  $\nu_e$ ,  $\nu_\mu$  and  $\nu_\tau$  however the phenomenon of neutrino oscillation allows the neutrinos to mix between the different flavour eigenstates. Most importantly, the observation of neutrino oscillation proved that neutrinos were in fact massive particles, contradictory to the standard model prediction of massless neutrinos. Additionally, this raised the question of whether the non-zero neutrino mass is a Dirac or Majorana mass. If the neutrino has a Dirac mass, like the other Standard Model fermions, then the neutrino and anti-neutrino would be distinctly unique particles, whereas if the neutrino has a Majorana mass, the neutrino would be its' own antiparticle.

One such method for investigating the nature of neutrino mass is to examine the beyond Standard Model (BSM) interaction of neutrinoless double beta decay ( $0\nu\beta\beta$ ). Neutrinoless double beta decay is a hypothesised nuclear decay and the neutrinoless analogue of two neutrino double beta decay ( $2\nu\beta\beta$ ), which is an exotic rare nuclear decay resulting in the emission of two beta electrons and two associated neutrinos from the same nucleus. Observing neutrinoless double beta decay would affirm the Majorana nature of the neutrino whilst providing additional insight into the absolute neutrino mass scale and hierarchy.

Many experiments have been developed to probe and measure the hypothetical  $0\nu\beta\beta$  decay including the SuperNEMO detector, which is the successor to the previous NEMO-3 experiment that ran and collected data for number of different double beta decaying isotopes between 2003 and 2011. The complete SuperNEMO detector design comprises of 20 smaller demonstrator modules, each holding between 5 and 7 Kg of the double beta decaying isotope  $^{82}\text{Se}$ . Currently a single SuperNEMO demonstrator module is undergoing construction and commissioning in the Laboratoire Souterrain de Modane. The demonstrator module combines unique tracking and calorimetry techniques in order to study the 6.25 Kg of  $^{82}\text{Se}$  source foil located at the centre of the demonstrator. The tracking capabilities of the SuperNEMO demonstrator allows the trajectory of reconstructed charged particles to be determined with high accuracy in three dimensions and the segmented calorimeters allows for the energies of individual particles to be measured. Also, there is the option

to apply a magnetic field to the tracker volume, in order to identify particles via their curvature in response to the applied field. Reconstructed particle kinematics combined with particle identification can be used to efficiently reject multiple backgrounds, however the currently proposed magnetic field may in fact not provide the best performance for the demonstrator module and there is also the possibility of taking data without turning on the magnetic field from the beginning.

A short description of each chapter is provided below:

- i The first chapter includes an introduction to neutrino phenomenology as well as the underlying physics of double beta decay.
- ii Chapter two overviews the SuperNEMO experiment and demonstrator module, including the relevant backgrounds for  $^{82}\text{Se}$  double beta decay. Also, the definition of the realistic magnetic field is given \*\*\*
- iii Chapter three gives a description of the different analysis techniques used in the thesis, including the internal software package Falaise. Additionally, the reconstructed topologies of different particles are described and how they come together to measure particles in particular decay channels. Finally, the tools needed to estimate the total signal and background contributions as well as the overall sensitivity of the study are given.
- iv Chapter four provides an in depth description of the double beta decay event selection used to determine if a reconstructed event has a double beta topology. Furthermore, the detection efficiency for  $0\nu\beta\beta$  and the contribution from the irreversible background  $2\nu\beta\beta$  are discussed.
- v In chapter six, descriptions for the different classifications of backgrounds are provided and the contribution of those backgrounds to the  $^{82}\text{Se}$  sensitivity are shown.
- vi Chapter 7 discusses the optimization process for reducing the prominent backgrounds from the previous chapter and provides estimations for the overall sensitivity using the statistical approximations discussed in the analysis techniques chapter.
- vii The final chapter concludes the magnetic field study, providing suggestions for how to approach the installation of the magnetic field or whether a magnetic field should in fact be used with the SuperNEMO demonstrator module, based on the results of the study.

## 1.1 Author's Contributions

# Chapter 2

## Neutrino Phenomenology and Double Beta Decay

The neutrino was first proposed by Wolfgang Pauli in 1930, following observations of continuous energy spectra from  $\beta$  decay electrons. Pauli suggested the existence of a small uncharged particle, emitted alongside the  $\beta$  electron, allowing the decay to conserve energy, momentum and spin. Enrico Fermi coined the name neutrino in reference to the similarly uncharged neutron, following its discovery by James Chadwick in 1932.

Having no electric or colour charge made the neutrino very difficult to identify from low intensity beta decaying isotopes and it wasn't until the 1950s that experimental evidence of the neutrino was first discovered at the Savannah River Nuclear Reactor. Cowan and Reines erected a nearby detector and successfully used the giant flux of antineutrinos coming from the reactor to illustrate the process of inverse beta decay, winning them the 1995 Nobel Prize.

Over the following half a century further breakthroughs were made in the field of neutrino physics, including the discovery of multiple neutrino flavours,  $\nu_{electron}$ ,  $\nu_{muon}$  and  $\nu_{tau}$ , corresponding to the three charged leptons. In the late 1960s, the Homestake experiment first measured the incoming solar neutrino flux as roughly 1/3 to 1/2 of the hypothesised flux, ultimately resulting in the discovery of neutrino oscillation and non-zero neutrino mass.

### 2.1 The Standard Model Neutrino

The Standard Model of particle physics describes fundamental particles and their interactions through the three underlying forces, the electromagnetic, the strong nuclear and the weak nuclear force. It is a renormalizable quantum field theory with an  $SU(3) \times SU(2) \times U(1)$  symmetry representing the strong, weak and electromagnetic interactions respectively.

$$\underbrace{SU(3)}_{Strong} \times \underbrace{SU(2) \times U(1)}_{Electroweak}$$

Predictions made by the Standard Model have been experimentally probed and proven to a high degree of accuracy, although the model falls short in certain aspects, in particular, the non-zero mass of neutrinos. Within the Standard Model neutrinos are massless, but we know, from observing oscillations, this is false. Fermions cannot have an explicit gauge invariant mass term

in the Standard Model Lagrangian and only gain their mass via spontaneous symmetry breaking. The absence of the right handed neutrino (or left handed anti-neutrino) does not allow the neutrino to couple to the Higgs and so the neutrino does not gain a Yukawa mass term from the Standard Model spontaneous symmetry breaking.

The origin of neutrino mass is still unclear however we know the Standard Model is wrong and neutrinos do have a non-zero mass.

Mass dirac vs Major \*\*\*

## 2.2 Origins of Neutrino Mass

Neutrino oscillation was first proposed by Bruno Pontecorvo in 1948 [?], akin to the oscillation observed with Kaons

$$K^0 \longleftrightarrow \bar{K}^0$$

However, this proposal was rejected, as a massless neutrino would not be expected to oscillate. Results from the Homestake experiment indicated a deficit in the number of expected solar neutrinos, with only 1/3 of the expected number being measured during the experiment.

Electron neutrinos produced by proton-proton fusion in the centre of the sun were used to induce the radiochemical transmutation of  $^{37}\text{Cl}$  into  $^{37}\text{Ar}$  via the inverse beta process



Many tons of a  $^{37}\text{Cl}$  containing compound were used to interact with the solar neutrinos and the resulting  $^{37}\text{Ar}$  gas was collected and measured to estimate the number of neutrinos that interacted with the  $^{37}\text{Cl}$ . The deficit of electron neutrinos found in the Homestake experiment was later dubbed the "Solar neutrino problem" and it wasn't until the end of the 20th century when experiments such as Kamiokande-II and SNO (Sudbury Neutrino Observatory) validated the results of the Homestake experiment and determined the number of solar electron neutrinos was suppressed as a result of neutrino oscillation [?].

Pontecorvos initial proposal was proven and the neutrino was shown to have a non-zero mass contradictory to the Standard Model expectation. In response to the proposal of neutrino oscillations, theorists have postulated

The implication of this discovery

Oscillation -¿ Higgs coupling...?

Three flavour states from Z invisible width

PMNS

### 2.2.1 Neutrino Mixing and Oscillation Phenomenology

Neutrinos are produced in weak decays and are emitted in their weak flavour eigenstates  $\nu_e, \nu_\mu$  and  $\nu_\tau$ . The flavour eigenstates propagate as plane waves corresponding to superpositions of the mass eigenstates  $\nu_1, \nu_2$  and  $\nu_3$ . The mixing between the flavour states and the mass states is given by the PMNS (Pontecorvo-Maki-Nakagawa-Sakata) matrix

$$\text{PMNS} = \begin{pmatrix} U_{e1} & U_{e2} & U_{e3} \\ U_{\mu1} & U_{\mu2} & U_{\mu3} \\ U_{\tau1} & U_{\tau2} & U_{\tau3} \end{pmatrix} = \underbrace{\begin{pmatrix} 1 & 0 & 0 \\ 0 & c_{23} & s_{23} \\ 0 & -s_{23} & c_{23} \end{pmatrix}}_{\text{Atmospheric}} \underbrace{\begin{pmatrix} c_{13} & 0 & s_{13}e^{-i\delta} \\ 0 & 1 & 0 \\ -s_{13}e^{i\delta} & 0 & c_{13} \end{pmatrix}}_{\text{Cross-mixing}} \underbrace{\begin{pmatrix} c_{12} & s_{12} & 0 \\ -s_{12} & c_{12} & 0 \\ 0 & 0 & 1 \end{pmatrix}}_{\text{Solar}}$$

which relates the triplet states via

$$\begin{pmatrix} \nu_e \\ \nu_\mu \\ \nu_\tau \end{pmatrix} = \begin{pmatrix} U_{e1} & U_{e2} & U_{e3} \\ U_{\mu1} & U_{\mu2} & U_{\mu3} \\ U_{\tau1} & U_{\tau2} & U_{\tau3} \end{pmatrix} \begin{pmatrix} \nu_1 \\ \nu_2 \\ \nu_3 \end{pmatrix}$$

The PMNS matrix is a unitary 3x3 matrix which encompasses the contributions  
 Neutrino oscillation infers neutrino mass implicitly and doesn't  
 Oscillation doesn't provide an explicit mass

### 2.2.2 The Mikheyev – Smirnov – Wolfenstein Effect

mass density of sun increased oscillation

## 2.3 Constraints on Neutrino Mass

### 2.3.1 Cosmological Constraints

### 2.3.2 Neutrinoless Double Beta Decay ( $0\nu\beta\beta$ ) Constraints

### 2.3.3 Mass Hierarchy

## 2.4 Open Questions on the Nature of Neutrinos

### 2.4.1 Dirac & Majorana Mass

### 2.4.2 See-Saw Mass Mechanism

### 2.4.3 CP Violation

## 2.5 The Physics of Double Beta Decay

### 2.5.1 Neutrinoless Double Beta Decay

### 2.5.2 Single and Higher State Dominance

### 2.5.3 Nuclear Matrix Elements

Phenomenology

# Chapter 3

## The SuperNEMO Demonstrator

SuperNEMO is the successor to the NEMO-3 experiment which ran from 2003-2011 collecting data for following double beta decaying isotopes,  $^{100}\text{Mo}$ ,  $^{82}\text{Se}$ ,  $^{130}\text{Te}$ ,  $^{116}\text{Cd}$ ,  $^{150}\text{Nd}$ ,  $^{96}\text{Zr}$  and  $^{48}\text{Ca}$ . Unlike NEMO-3 however, SuperNEMO will focus solely on the isotope  $^{82}\text{Se}$ .

SuperNEMO is located in the underground laboratory, Laboratoire Souterrain de Modane (LSM), located within the Frejus road tunnel linking Modane to Bardonnecchia. The underground location helps to protect the detector from cosmic radiation and further protection comes in the form of iron and water shielding which reduces the impact of the natural radiation found in the surrounding rock.

NEMO-3 used a cylindrical design, divided into 20 equal sections of isotopic source material whereas SuperNEMO uses a modular structure, with the source located at the centre of the detector, surrounded by the tracker and calorimeters. The structure of the detector allows charged particle tracks and energies to be determined as they propagate through the volume of the tracker before finally coming to rest within the calorimeters.

During detector operation, it is expected for the detector to use a magnetic field, applied to the tracker volume to determine the charged of the particles passing through the detector. However, prior to activating the magnetic coil, the influence of different magnetic field configurations will be investigated in this thesis to determine the optimum magnetic field choice for the detectors operational lifetime.

SuperNEMO structure also allows scaling, exchanging isotopes that can be processed into foils  
\*\*\*

\*\*\*shielding\*\*\*

SuperNEMO utilises a

### 3.1 The SuperNEMO Demonstrator Design

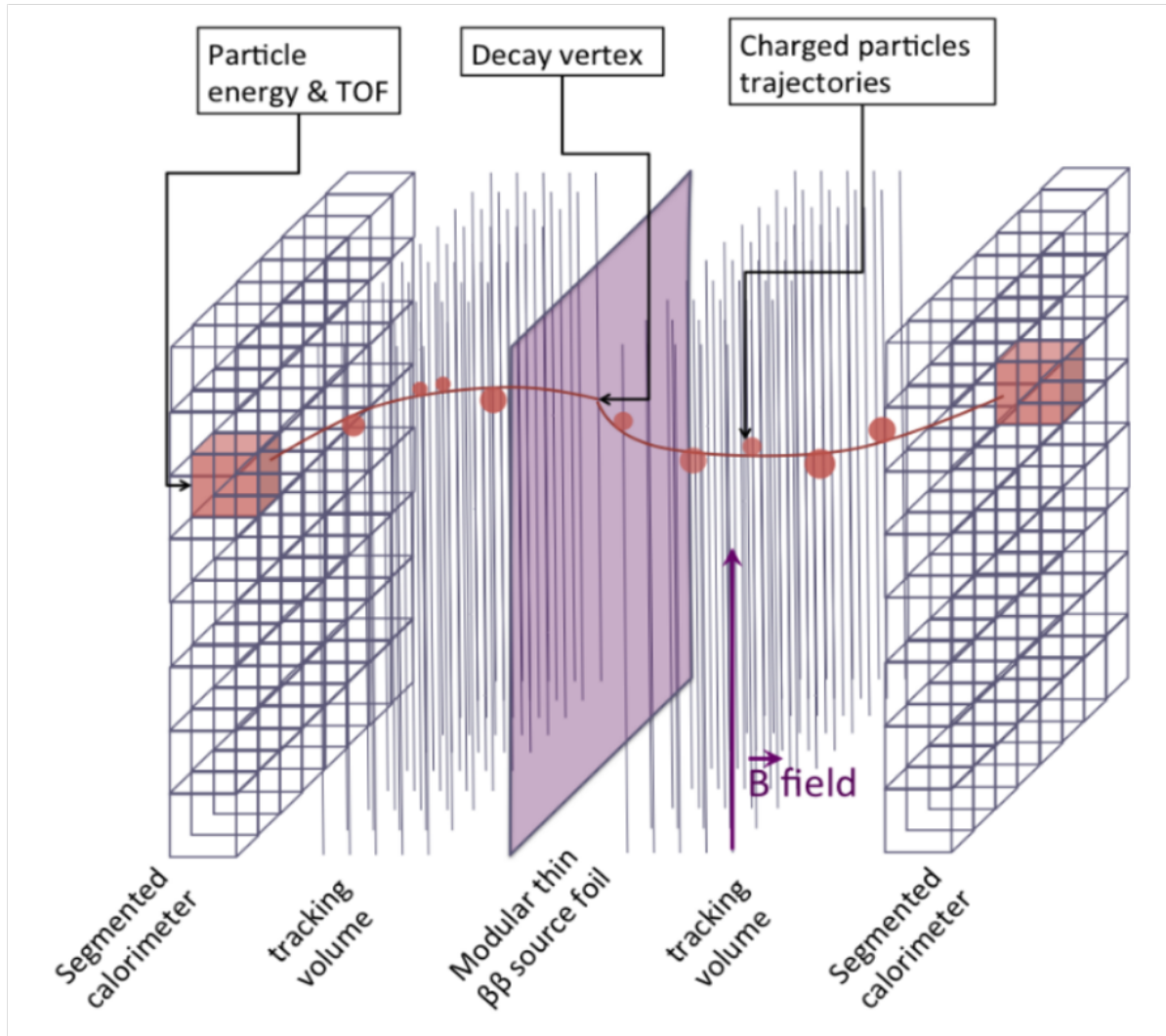


Figure 1: DemonsDetector

Unlike previous double beta decay experiments, SuperNEMO (and NEMO-3) uses a source-tracker-calorimeter structure allowing both the particle energy and the associated trajectory to be determined. The structure of the detector provides multiple advantages compared to other double beta decay experiments including,

- i Being able to identify and differentiate all natural radioactive particles, that is, the electron, positron, photon and alpha particle. Furthermore it is possible for SuperNEMO to identify muons that may cross the detector
- ii Identifying multiple particles allows for a variety of decay channels to be investigated, primarily



the two electron channel for double beta decay as well as the  $1e1\alpha$  channel for BiPo measurements or other background decay channels.

- iii State dominance of the  $^{82}\text{Se}$  decay and whether the decay is dominated by a single intermediate state or many higher energy intermediate states
- iv Can be easily scaled to increase the exposure of  $^{82}\text{Se}$  or perhaps investigate other double beta decaying isotopes

However there are also a number of disadvantages as a result of the detector design including,

- i Low source mass, limited by the thickness of the source foil. If the source foil is too thick it will inhibit the emission of electrons from inside the foil reducing the detection efficiency.
- ii Lower detection efficiency and energy resolution compared to germanium and bolometer experiments.

### 3.1.1 Detector Structure

As mentioned, the SuperNEMO detector uses a modular source-tracker-calorimeter with the use of a passive source, that is, a source that is not part of detection unlike the proposed for the germanium experiment LEGEND <sup>\*\*\*ref\*\*</sup>.

The source foil is located at the centre of the detector, surrounded by the tracker volume and finally the calorimeters. The source foil is a thin, mechanically processed foil, that is enriched in  $^{82}\text{Se}$ . The narrowness of the foil allows for improved emission of charged particles from the source foil and into the tracker chamber. In total the source foil mass was measured to be approximately 6.23Kg of enriched  $^{82}\text{Se}$ , whilst being approximately 2.7m in length.

$^{82}\text{Se}$  was selected as the isotope of choice for the SuperNEMO demonstrator, amongst the isotopes used in the NEMO-3 detector because of its relatively high decay energy, reasonable  $2\nu\beta\beta$  half-life, high natural abundance, ease of enrichment and reasonable phase space factor. The properties of the isotopes used in NEMO-3 are shown below

The low decay energy removes a large amount of the low energy backgrounds whilst the remaining factors ensure the availability of  $^{82}\text{Se}$  with a frequent amount of decays.

<sup>\*\*\*cu foil, used for external bg, 34 foils in total, covered in mylar \*\*\*</sup>

To track the trajectories of the charged particles propagating from the source foil, each side of the surrounding tracker chamber comprises of 113 columns of nine drift cells, totalling 2034 cells for both sides of the tracker. Each drift cell contains a central anode wire which is run at a high voltage, surrounded by eight grounded field shaping wires and two ring shaped cathodes at on either end of the cell.

tracker chamber surrounding the source foil <sup>\*\*\*</sup> planar to source foil unlike rounded nemo 3

Isotope	$Q_{\beta\beta}$ (MeV)	$G_{0\nu}$ ( $10^{-15}y^{-1}$ )	$T_{1/2}^{2\nu}$ (y)	$\eta$ (%)
$^{48}\text{Ca}$	4.273	24.81	$6.37^{+0.56}_{-0.69} {}^{+1.21}_{-0.89} 10^{19}$ (NEMO-3)	0.187
$^{76}\text{Ge}$	2.039	2.363	$1.926 \pm 0.094 10^{21}$ (GERDA)	7.8
$^{82}\text{Se}$	2.995	10.16	$9.6 \pm 0.3 \pm 1.0 10^{19}$ (NEMO-3)	9.2
$^{96}\text{Zr}$	3.350	20.58	$2.35 \pm 0.14 \pm 0.16 10^{19}$ (NEMO-3)	2.8
$^{100}\text{Mo}$	3.035	15.92	$6.93 \pm 0.04 10^{18}$ (NEMO-3)	9.6
$^{116}\text{Cd}$	2.809	16.70	$2.8 \pm 0.1 \pm 0.3 10^{19}$ (NEMO-3)	7.6
$^{130}\text{Te}$	2.530	14.22	$6.9 \pm 0.9 10^{20}$ (NEMO-3)	34.5
$^{136}\text{Xe}$	2.458	14.58	$2.165 \pm 0.016 \pm 0.059 10^{21}$ (EXO-200)	8.9
$^{150}\text{Nd}$	3.367	63.03	$9.11^{+0.25}_{-0.22} \pm 0.63 10^{18}$ (NEMO-3)	5.6

Figure 2: Isotope Properties

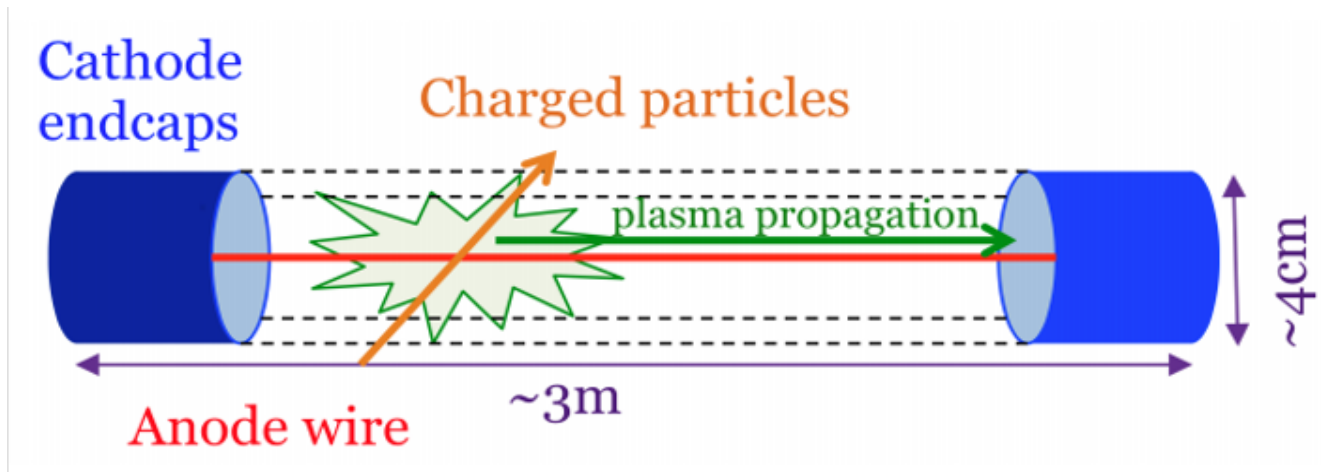


Figure 3: TrackerCells

The tracker is filled with gas, a mixture of He (95%), ethyl alcohol (4%) and Ar (1%). As charged particles enter the tracker chamber they ionize the gas and the time taken for the ionized electron shower to drift towards the anode infers the distance of the charged particle from the centre of the cell. Tracker cells are run in Geiger mode, so that \*\*\*\*Geiger definition \*\*\*

Additionally, the two cathode end caps measure how far along the the tracker cell the charged particle was when generating the electronic shower. The combination of these two mechanisms allows the trajectory of the particle to be determined in three dimensions.

The final component of the SuperNEMO demonstrator module structure is the calorimeter wall, which surrounds the tracker. Calorimeters or optical modules (OMs) measure the energy of the charged particles that are emitted from the source foil and come to rest within the calorimeters. Each calorimeter consists of a plastic scintillator as well as a photomultiplier tube (PMT).

The plastic scintillator is made of POPOP (1,4-di-(5-phenyl-2-oxazolyl)benzene) doped polystyrene,

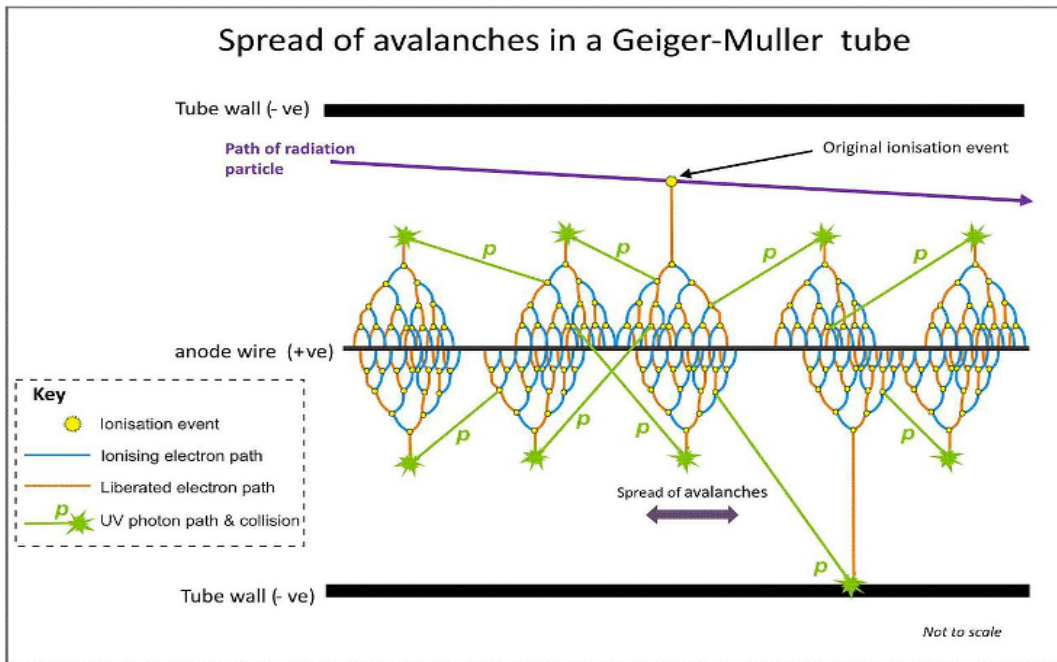
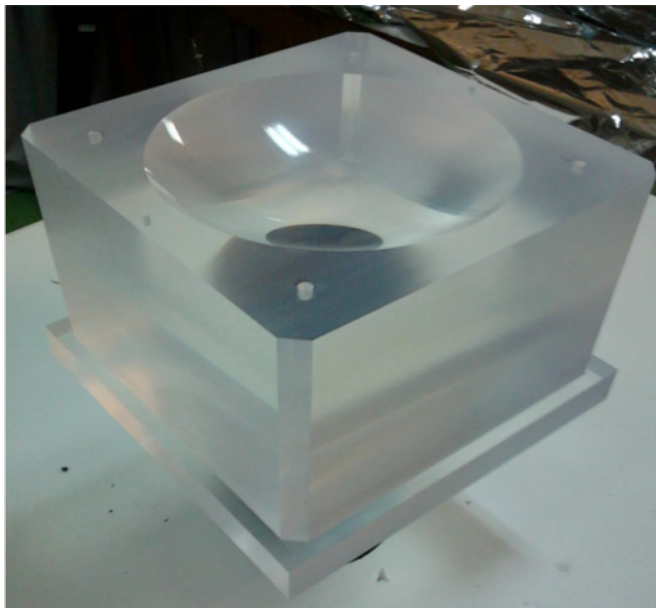


Figure 4: GeigerMechanismtrum



(a) ScintCurve



(b) OM

which acts as a wavelength shifter and PTP (para-terphenyl) which increases the light yield during ionization. When an incident particle strikes the plastic scintillator block, it loses energy from multiple scatterings, resulting in a number of photons being emitted proportional to the incident

particle energy. Scintillator blocks are wrapped in both aluminised mylar to increase light collection and protect against UV radiation from the tracker or adjacent OMs and teflon to increase photon collection efficiency.

8.3% energy res FWHM at 1 MeV

Hamamatsu PMTs were recycled from NEMO-3 for use in SuperNEMO and come in two sizes, 8" and 5". The 8" calorimeters provide improved energy resolution and thus mostly confined to the parts of the calorimeter wall with the greatest particle flux. By carving the plastic scintillators, the PMT bulbs can be coupled to them using radiopure glue.

There are a total of six calorimeter walls for SuperNEMO, two of each of the following; Main wall, X wall and the Gamma Veto or Veto wall. Each wall is comprised of a different number of calorimeters with the corresponding PMT size,

- i Main wall: 220 8" calorimeters and 40 5" calorimeters.
- ii X wall: 64 5" calorimeters.
- iii Veto wall: 32 5" calorimeters.

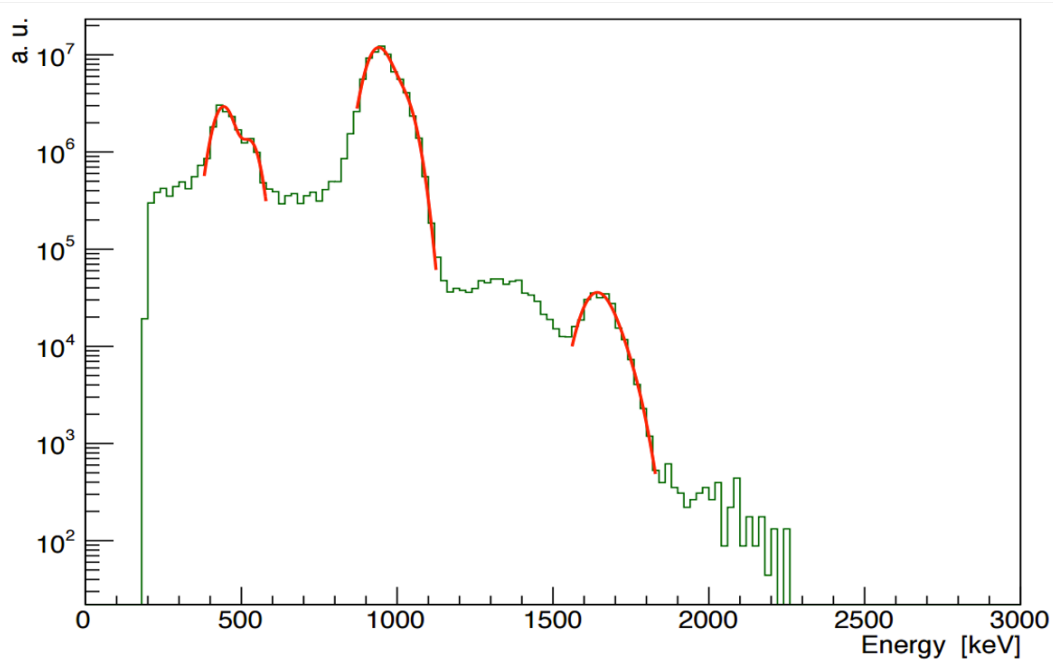
so the total number is doubled for each type of wall.

Unlike NEMO-3 calorimeters, light guides are also used with the calorimeters to further increase the collection efficiency of incident photons. Importantly, the presence of the light guides significantly alters the applied magnetic field inside of the tracker chamber, resulting in a significant non-uniformity of the field. The impact of this will be discussed later\*\*\*.

### 3.1.2 Commissioning Progress

Multiple calibration methods will be used to determine the energy and time responses of the detector to known sources. To perform energy calibration for SuperNEMO,  $^{207}\text{Bi}$  will be deployed within the detector to obtain an absolute energy measurement.  $^{207}\text{Bi}$  undergoes a number of internal conversions, resulting in the emission of electron calibration lines with energies of at 482, 976 and 1682 keV.

For each source, a droplet of  $^{207}\text{Bi}$  in between two layers of mylar will be encapsulated by a radiopure copper frame, following which they will be inserted into the gaps between the source foils via an automatic source deployment system. Calibration is expected to be performed regularly during detector operation to ensure energy measurements are accurate. The  $^{207}\text{Bi}$  internal conversions will be reconstructed from the location of the copper frames to the calorimeters to determine the measure energies compared to the true  $^{207}\text{Bi}$  internal conversion lines. For the purposes of investigating the sensitivity of the experiment to neutrinoless double beta decay in the  $^{82}\text{Se}$  region of interest (2.8-3.2 MeV) the greatest internal conversion energy of 1682 keV will provide the best degree of calibration at those energies.

Figure 6:  $^{207}\text{Bi}$  Spectrum

Alongside the  $^{207}\text{Bi}$  deployment close to the source foil, a light injection system (LIS) will also be deployed to perform both time calibration and measure gain for the optical modules. The light injection system uses pulses of ultraviolet light from light emitting diodes, through optical fibres to illuminate OMs and measure their gain. The length of all fibres will be maintained at 20m to avoid any systematic time differences.  $^{241}\text{Am}$  is used as a source with a reference OM to monitor and maintain the light level. In total, the LIS will allow any variations in gain from voltage fluctuations be tracked and corrected with a precision of 1% alongside the time calibration.

Additional time calibration will be performed using  $^{60}\text{Co}$ , which produces two photons, the first being of energy 1.17 MeV and the second, 1.33 MeV. The two photons are emitted almost simultaneously ( $\Delta t = 0.41\text{ps}$ ) from the source at a separation much lower than the time resolution of the PMTs. However, by placing the  $^{60}\text{Co}$  source behind the main wall in one of nine different positions, at known distances from two PMTs, the energies and time separation of the two photons can be measured to determine the offset of the PMTs.

Current status \*\*\*

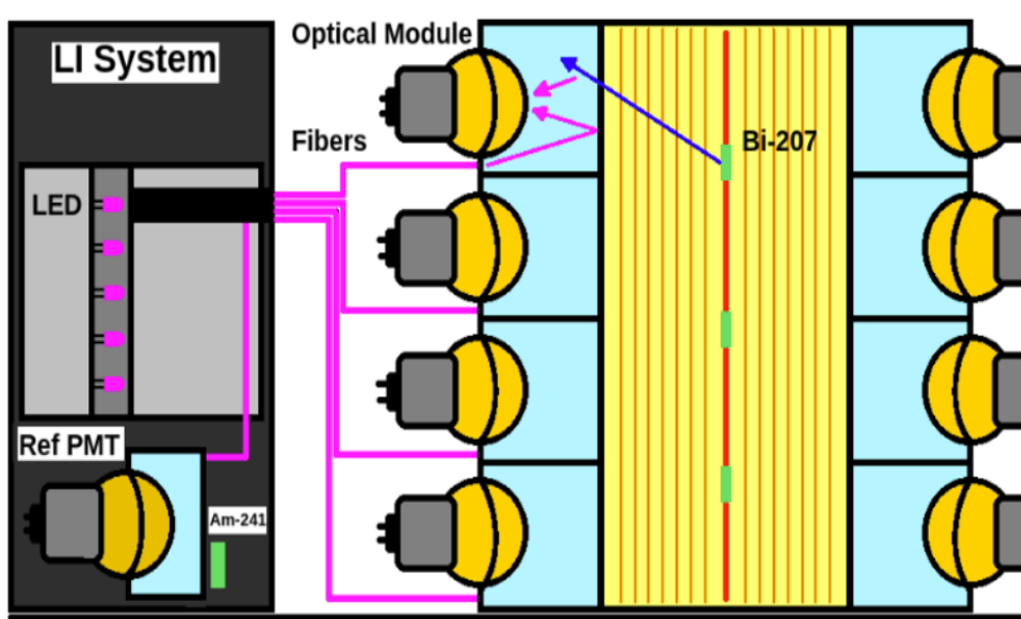


Figure 7: LIS

### 3.1.3 Detector Calibration

### 3.1.4 Expected Sensitivity

## 3.2 Backgrounds Sources

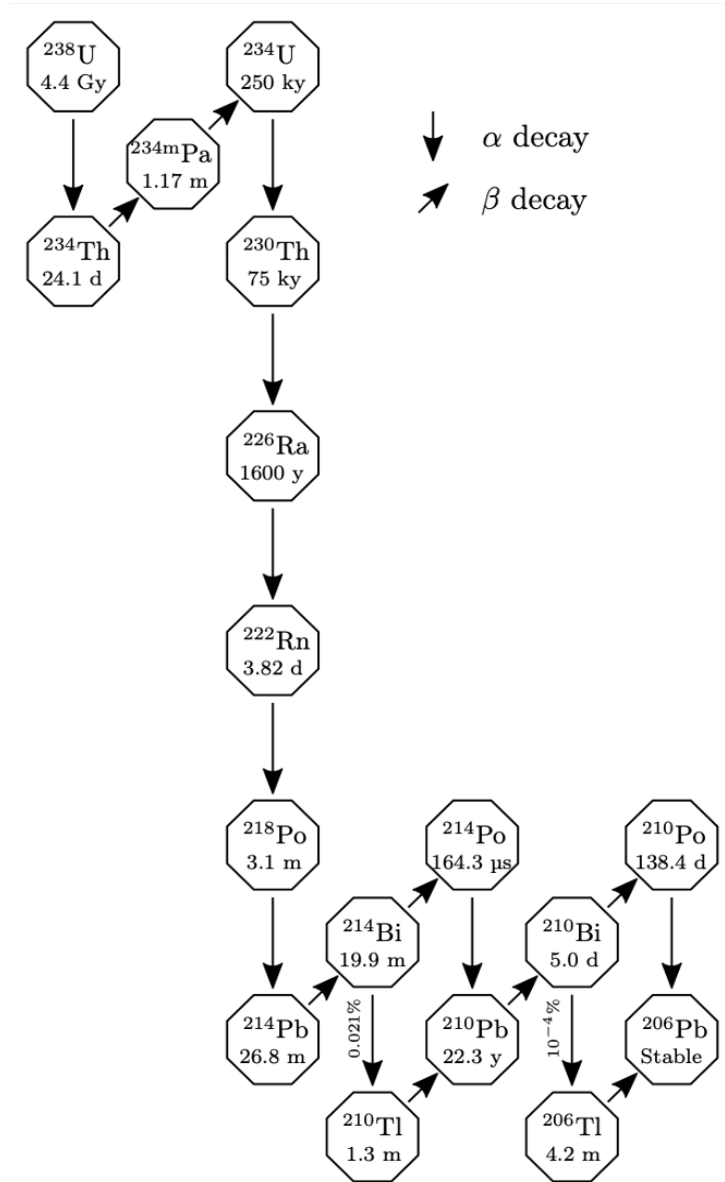


Figure 8: Bi214DecayScheme

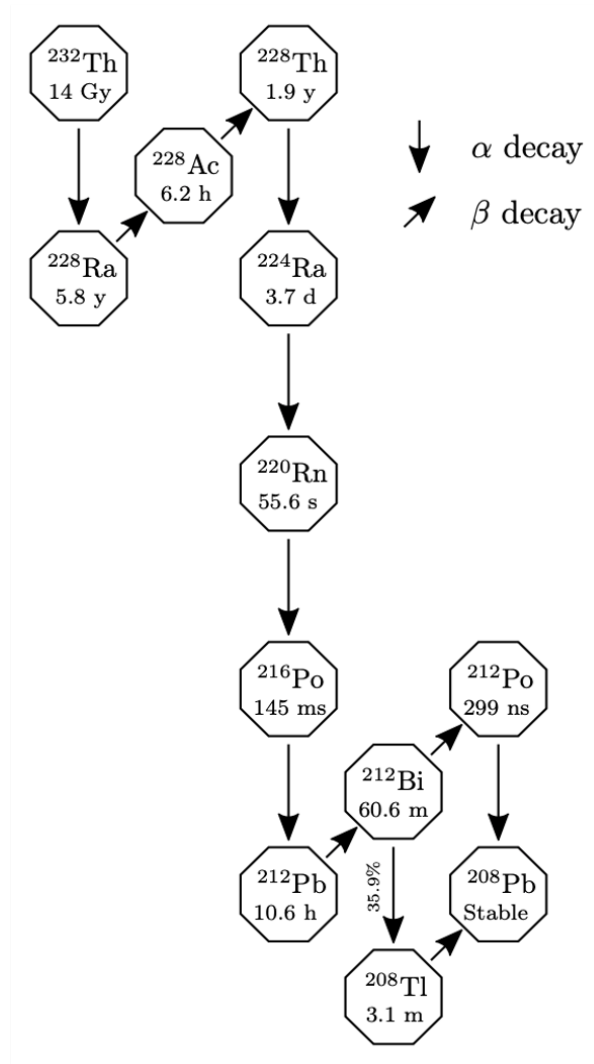


Figure 9: Tl208DecayScheme

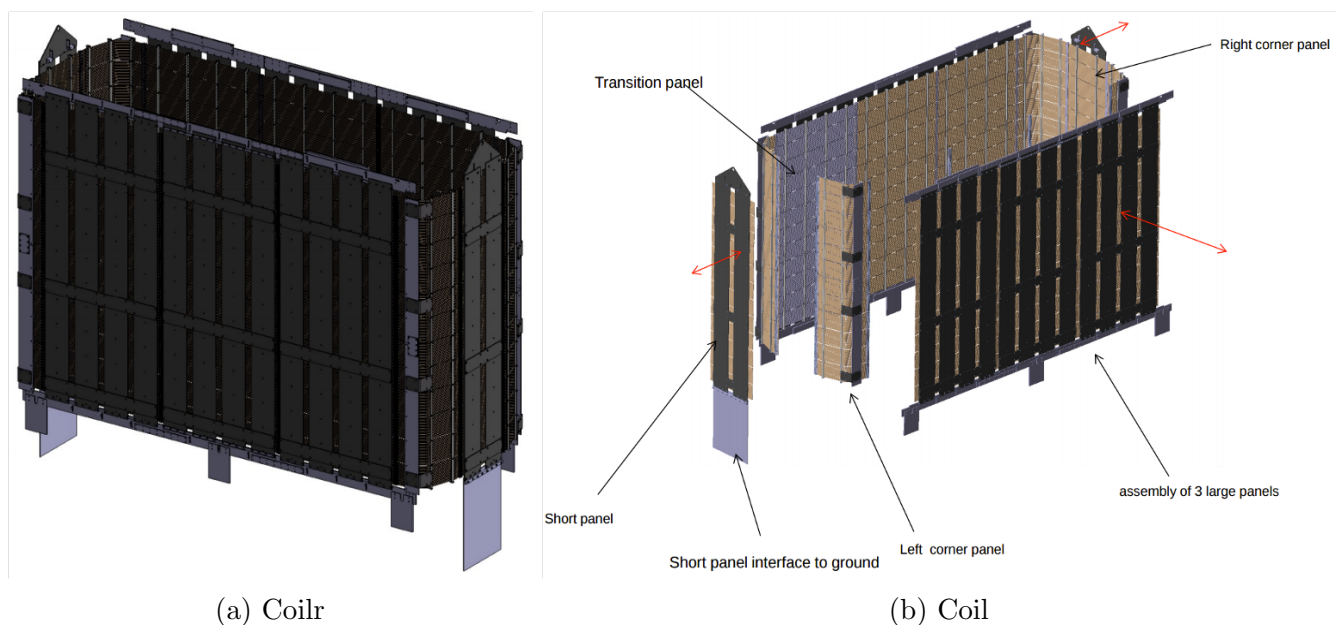


### 3.2.1 Other DBD Experiments

\*\*\*

### 3.2.2 Magnetic Coil and Shielding

The magnetic field for the SuperNEMO detector will be generated by a copper magnetic coil, recycled from old NEMO-3 copper rods. The coil will be built to surround the detector ensuring the magnetic flux is contained within the tracker volume.



The presence of magnetic field inside the glass of a PMT significantly reduces the performance of the PMT even at very low field strengths, figure ??

Unlike NEMO-3, SuperNEMO does not use a light guide with the OMs as the PMTs are directly coupled to the plastic scintillators as shown in figure \*\*\*\*ref \*\*\*. As a result, the PMTs are exposed to the tracker volume and the potential magnetic flux. To prevent the PMT performance being reduced by the magnetic field, iron shields will be used to protect the PMTs and remove any magnetic field from within their volume.

Furthermore, it is expected that the coil will be used to generate a magnetic field of approximately 25 Gauss. However it is possible for the strength of the magnetic field to be adjusted by altering the current inside of the coil. The purpose of the magnetic field applied to the tracker volume is to help determine the charge of any particle propagating through the tracker by measuring the magnetic field induced curvature of the particle. Electrons from  $^{82}\text{Se}$  double beta decay are of relatively low energy and so do not require high magnetic field strengths to curve them, however it

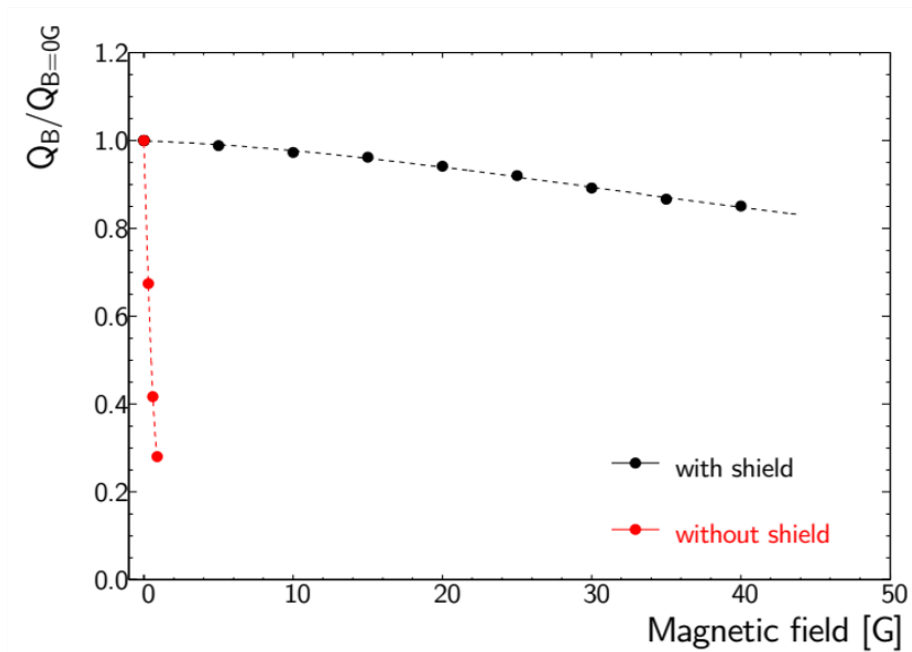


Figure 11: A

may be pertinent to use a different field strength if it results in an increase in the detection efficiency of  $0\nu\beta\beta$ .

### 3.3 Motivation for Magnetic Field Studies

The magnetic field allows electrons and positrons to be differentiated by the directionality of their associated track curvatures. It provides a useful tool for removing significant backgrounds, in particular photons with energy greater or equal to 1.02 MeV, which are capable of pair producing an electron positron pair. Other sources of positrons include rare positron emitting decays however they are seldom observed and not expected to be problematic.

\*\*\*pair produce/ show electron curvature \*\*\*

Photon flux inside the detector is extremely high as illustrated by table \*\*\* table of photon flux for different sources\*\*\* so positron identification is a priority. However it may be possible to use the detector without a magnetic field. Removing or reducing the strength of the magnetic field may increase the number of expected background events, however it may also increase the signal reconstruction efficiency, resulting in a net gain in sensitivity. By reducing the positron generating backgrounds by other means, it may be possible to increase the signal efficiency without significantly increasing the background that comes with having a reduced or no field.

Initially, three magnetic field configurations were selected, including the uniform field, no field and the realistic field. The uniform field is defined as having a nominal 25 Gauss field, with uniform strength and shape throughout every part of the detector. No field is characterised by having no magnetic field (0 Gauss) throughout the detector and corresponds to having the magnetic field turned off. The realistic field is a mathematically computed field, representing the shape and strength of the field we expect to see during operation with a nominal 25 Gauss applied via a magnetic coil.

By comparing the detection efficiency of the three magnetic field configurations, a decision can be made as to when or if activating the magnetic field will increase our sensitivity to  $^{82}\text{Se}$  neutrinoless double beta decay. Maximising our sensitivity increases the probability of observing the decay, whilst simultaneously improving the precision of nuclear matrix elements and setting better limits on the decay itself.

### 3.3.1 The Realistic Field

Unlike NEMO-3, magnetic shields are required for the SuperNEMO demonstrator module as a consequence of the detector geometry exposing the PMTs to magnetic flux. The removal of a light-guide coupled to the surface of the PMTs exposes the vacuum tube of the PMT to the magnetic field inside the tracker volume. As shown in figure \*\*\* the presence of a magnetic field is extremely detrimental to the performance of a PMT and so the shielding should ensure that all magnetic flux is removed from the volume of the PMTs.

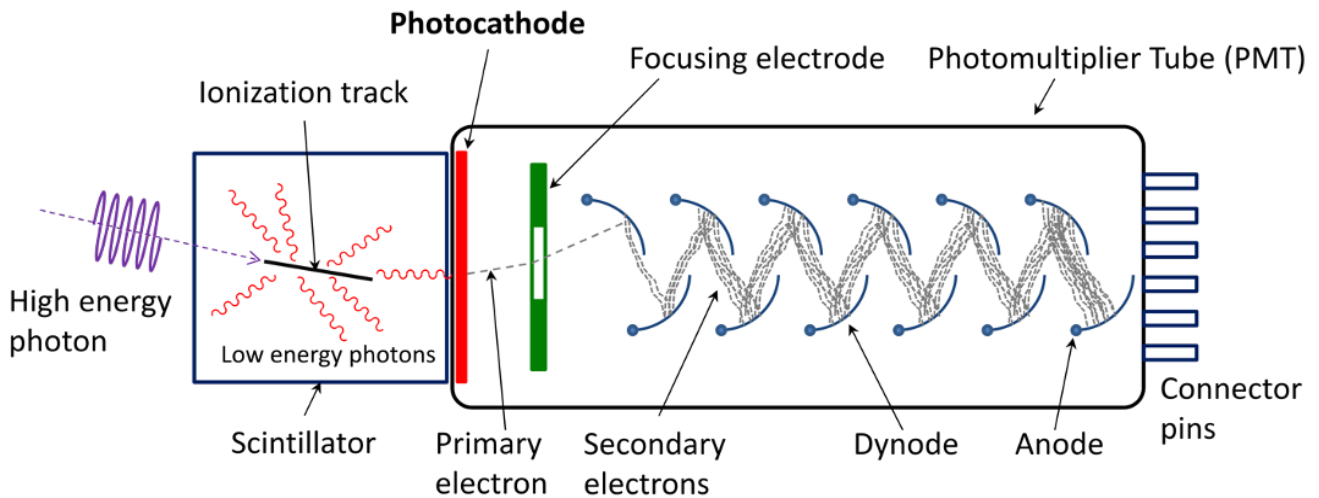


Figure 12: A

\*\*\*from wiki

The working mechanism of a PMT involves incoming photons generating photoelectrons that are focused onto the the first dynode. Secondary electron emission from the dynodes carries a charge which is collected by the anode. The collected current provides an output signal to indicate a hit to the calorimeter.

With the addition of a magnetic field, the low energy photoelectron trajectories are altered, reducing the collection efficiency of the dynodes. Even at a field strength of 1 Gauss the reduction in collection efficiency results in a complete loss of signal. Furthermore, there is the possibility of PMT components, in particular, the dynode substrate and the electrode, being permanently magnetised following exposure to weak magnetic fields for long periods of time. The residual magnetization can result in a change to the gain of a PMT, ultimately reducing performance. Over the length of time taken for detector operation any changes in the gain of PMTs should be monitored to ensure the precision of energy measurements are maintained.

As a result of using the magnetic shields however, the shape and strength of the field is altered so that is it no longer uniform in shape or strength. As mentioned earlier, the expected magnetic field is labelled the realistic field and represents the magnetic field altered by the magnetic shielding to protect the PMTs against the magnetic flux in the tracker. The shape and strength of the realistic field is shown in the image below

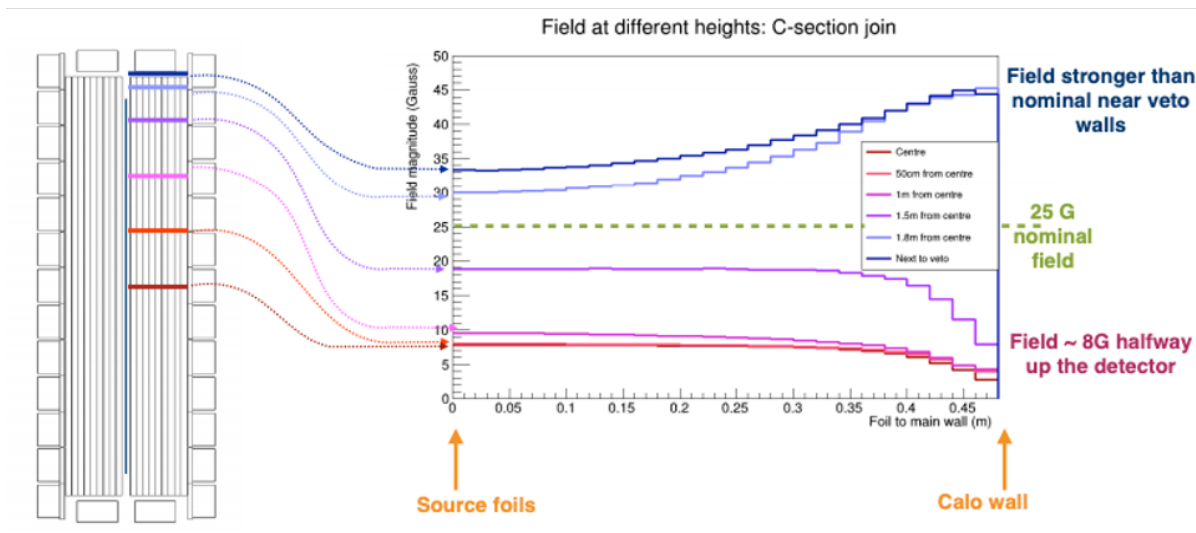


Figure 13: A

The main aim of the magnetic field analysis described in this thesis is to compare the performance of the three field configurations to determine which of the three fields is most advantageous for use during and throughout the detectors operational lifetime. Although the uniform field does not correctly depict the non-uniformity of the magnetic field during operation, it provides a nominal representation to compare to the other magnetic fields. Furthermore, by scaling the magnetic field applied by the coil, it is possible to increase the field strength of the realistic field so that it more

closely resembles the uniform field and a more direct comparison can be made.

\*\*\*\*as shown by scaled field\*\*\*\*

No field examines the performance of the detector without an applied magnetic field. If no field displays an increased performance over the realistic and uniform fields it may be advantageous to run the detector without a magnetic field and to remove pair produced backgrounds through other avenues. Additionally, there is the option to run the detector without the magnetic field for a short period of time and to determine at what point, if at all, to turn on the magnetic field during experimentation. Once the magnetic field is turned on, it is impossible to reverse the effects of the applied field on the detector components even if the field is later turned off and so it is important to identify what approach to take and if or when the magnetic field should be applied, as applying the field is irreversible.

\*\*\*maybe more detail on shields, relative permeability, vs field inside field \*\*\* maybe include pic of own magnetic field in 3D

### 3.3.2 Magnetic Shield Testing

Prior to installation, individual magnetic shields were tested to ascertain whether they were still able to significantly reduce magnetic flux from within the volume inside. To measure the efficiency at which the shields remove magnetic flux from within their own volume, the magnetic field with and without shielding was measured. A copper solenoid was connected to a controlled current source to generate a magnetic field. The solenoid was coiled around an impermeable container to retain the field inside of the container. A magnetometer was used to measure the field strength within the container. The field was calibrated to 25G following each measurement and the magnetometer measured the field strength, with and without shielding to determine the influence of the shield on the magnetic field inside of it.

Over 250 shields were tested, both for 8" and 5" PMTs, with the majority expelling over 95% ( $B < 1.25\text{G}$ ) of the magnetic field within the shielded volume. Once tested the shields were packed and shipped to the LSM to be installed as part of the detector.



Figure 14: A

# Chapter 4

## Analysis Techniques

### 4.1 Falaise

Falaise provides the overarching software environment and is used as the primary tool for the simulation, processing and analysis of data for the SuperNEMO collaboration. Falaise uses the DECAY0 event generator in combination with GEANT4 and the C++ Bayeux library to generate and propagate particles throughout the depiction of the detector geometry.

Falaise is comprised of four principal components:

i Flsimulate

The primary tool for simulating data

ii Flreconstruct

Pipeline structure used to process the output from flsimulate and produce reconstructed data

iii Flvisualize

Event viewer for the visualization of the detector geometry, simulated and reconstructed data

iv LibFalaise

The core libraries

Data production follows the route displayed in figure ???. Firstly, events are simulated, after which the simulated data is processed via a reconstruction pipeline to generate reconstructed data.

The reconstructed data represents the real data we expect to take during detector operation.



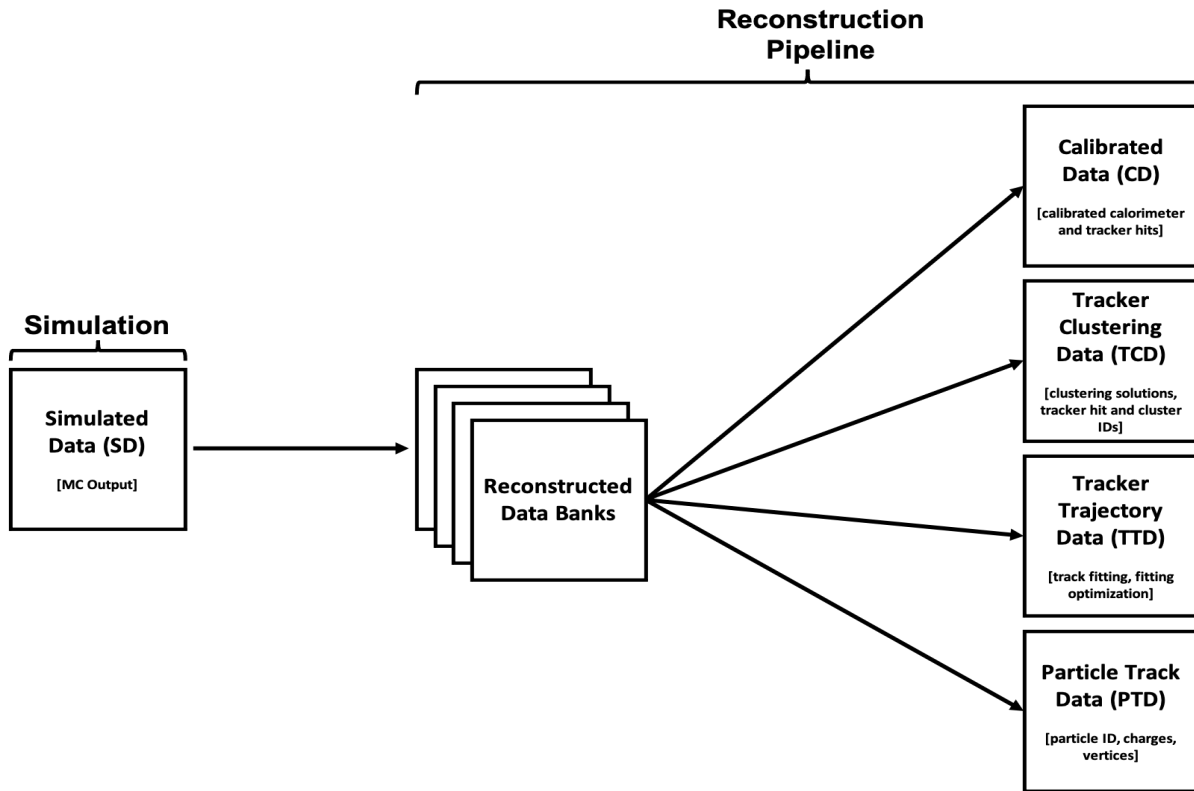


Figure 15: Visualization of the Falaise pipeline structure, beginning with simulation and ending with the stored data banks for reconstructed data.

#### 4.1.1 Simulation

Fsimulate is the main simulation tool for SuperNEMO. Fsimulate is a command line program which accepts a configuration file that provides instructions for simulating events. The configuration file allows the user to determine multiple criterion for simulation, including;

- i The initial decay particle
- ii The availability of raw data for secondary particles (those which interact with the primary decay particle)
- iii Location of the decay vertex
- iv Number of simulations
- v Magnetic field configuration

The DECAY0 event generator is responsible for generating the initial radioactive decay particle with appropriate energies, timing, kinematics and branching ratios. Propagation of decay particles

through the detector is determined by the object-oriented toolkit GEANT4 [?], which simulates the interactions of decay particles with the detector geometry and materials. GEANT4 also manages detector hits, tracks and visualisation for each simulated event. Flsimulate provides a default output file type of Boost over Root I/O (.brio) as suitable input for both reconstruction (flreconstruct) and visualization (flvisualize).

### 4.1.2 Reconstruction



The simulated output is processed with flreconstruct, using a customizable reconstruction pipeline which runs through the raw data. Modules can be sequentially selected to generate and fill multiple data banks with reconstructed data. The four primary data banks are displayed in figure ??, with example data types given. Reconstructed data provides an accurate depiction of the real data that would be processed during detector operation. However, the reconstructed data may not be necessarily representative of the true simulated data. By simulating and reconstructing different decays, we can measure the efficiency at which we are able to correctly reconstruct simulated data in various decay channels.

An additional factor for reconstruction is the fitting type used by the TrackFit pipeline module. Charged particles can either be fitted with a straight track or a helical track, determined by the  $\chi^2$  of the proposed track. The track with the lowest  $\chi^2$  is selected from amongst the calculated tracks and is fitted to the simulated track. For no field simulations we expect the charged particle tracks to be straight and so helical fitting may not be necessary. However, removing helical fitting from no field simulations led to a sharp decrease in the track fitting efficiency of charged particles, as solely allowing straight line fitting increased the rate of mis-reconstructions. For gamma tracking an alternative tracking module, GammaTracking, is used, which does not allow for alternative track types to be fitted.

### 4.1.3 Visualization

Event display visualization of both raw and reconstructed data is possible using the GUI display, flvisualize. Flvisualize provides an interface for both 2D and expansive 3D visual projections of the detector. Visualised data is shown within the framework of the detector to allow for visual analysis of simulations. The left hand panel of flvisualize provides a 2D display of either the top, side or front of the detector. The second panel displays a 3D projection of the detector including all three spatial dimensions. Flvisualize also provides multiple panels, including a 'Tracks' panel, which displays reconstructed data structures with selective visuals, allowing the user to determine which visuals they wish to display. The remaining panels, 'Options' and 'Selections', provide additional functions however they are unimportant.



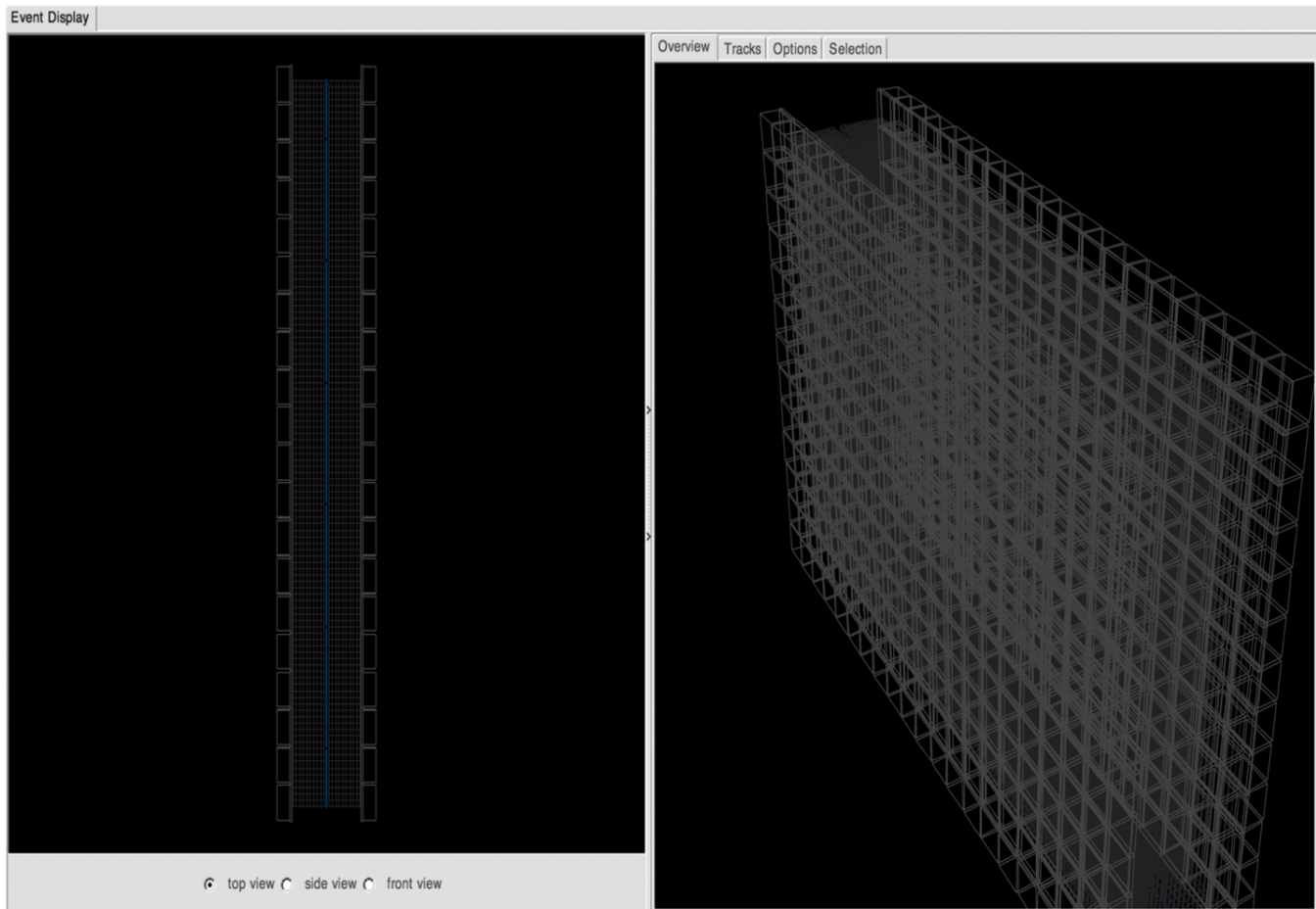


Figure 16: User interface of the Flvisualize tool used for visually displaying simulated and reconstructed events. The left hand side displays a 2D top view of the detector whereas the right hand side displays a 3D projection of the detector parallel to the foil.

#### 4.1.4 Secondary Particle Information

Secondary particle information provides increased true/GEANT level information, including additional insight into the properties of simulated particles, both primary and secondary. Secondary particle information provides the following:

- i Particle designation (electron/positron/photon) for all true simulated particle tracks
- ii Particle classification (primary or secondary) contingent on if the particle originated from the initial decay (primary) or from any other source (secondary)
- iii Number of true GEANT level hits for each particle track
- iv Simulated true track visuals in flvisualize

Additional simulations, with access to secondary particle information, were simulated in order to shed more light on the underlying mechanism behind the considerable number of double beta candidate events from external  $^{208}\text{Tl}$ . Understanding the underlying mechanism allowed for the background to be explicitly targeted and removed, in order to reduce the total background contamination, as will be discussed in chapter ??.

#### 4.1.5 Sensitivity Module

Sensitivity Module is a Falaise pipeline module which converts stored data from the Falaise data banks into easily readable ROOT nTuples. Sensitivity Module uses the output from fireconstruct to generate nTuples containing both simulated and reconstructed data. The combination of true and reconstructed data forms can be used to validate an analysis, by ensuring the true data supports inferences made using the reconstructed data.

Sensitivity Module can be uniquely compiled to add supplementary nTuple branches, containing a multitude of variables that may not already be encompassed into the pipeline. This allows additional parameters to be investigated as long as they can be computed from the Falaise data banks. By establishing the parameters necessary for identifying double beta decays, the selected parameters can be used to devise a double beta candidate cut flow.

The cut flow is a sequential application of data cuts, to determine the number of events in a particular **decay channel**. Events that pass all of the selected cuts are labelled as candidate events for the corresponding decay channel. During experimentation, the cut flow will be used on real data to probe various channels. By measuring the efficiency of reconstructing backgrounds in the two electron channel, the contribution of individual backgrounds to the  $0\nu\beta\beta$  sensitivity can be determined.

## 4.2 Reconstructed Topologies



To identify double beta candidate events from reconstructed data, the reconstructed topology of charged particles must first be established so that the corresponding cuts can be identified and applied to the Sensitivity Module root nTuples. A double beta candidate event has a two electron topology, so only the reconstructed topology of an electron is needed. For the multitude of different backgrounds channels, the reconstructed topologies of the positron, photon and alpha particle are necessary.



Particles in the Falaise environment are identified by a select number of predefined parameters including the following,

- i Reconstructed track: A number of tracker hits, greater than three, that are successfully reconstructed as a single track.
- ii Vertex: The initial reconstructed position of the decay, usually extrapolated from the first detector hit back to the source foil.
- iii Associated calorimeter hit: A calorimeter hit, with a defined energy that corresponds to a charged particle track. The associated tracks should belong to the same particle as the calorimeter hit.
- iv Unassociated calorimeter hit: A calorimeter hit, with a defined energy, without a corresponding charged particle track. The calorimeter hit should be isolated from any charged particle track.
- v Delayed track: A delayed track can have fewer than three tracker hits, however, the timing of the hits should be much later than the initial decay time determined by the first tracker hit.
- vi Time of flight (TOF) : The associated timing information for a particle striking a calorimeter and whether the timing corresponds to a gamma or charged particle. The Sensitivity Module cuts for TOF are the Internal and External probabilities.



The predefined parameters are used as the basis for defining the various reconstructed particle topologies in the Falaise environment, which can be combined to probe specific decay channels, including the  $2e$  channel for  $0\nu\beta\beta$  as well as the various relevant background channels.

### 4.2.1 Electrons and Positrons

Electrons are the primary particles for double beta decay so it is vital they are identified and differentiated from other particle topologies. Within the Falaise environment, the light charged particles (electron/positron) are characterized by a curved reconstructed track, with a vertex on the source foil and an associated calorimeter hit, as defined above. The subtle difference between the particle topology of an electron and a positron is the curvature of the track under an applied magnetic field as shown in figure ???. As a result of its' positive charge, the positron curves in the

opposite direction to the electron; clockwise from a top down perspective. Whereas the negatively charged track curves anti-clockwise from a top down view. The curvature of the charged particle is also dependant upon the direction of travel, as shown by equation ??,

$$\vec{F} = q\vec{v} \times \vec{B} \quad (1)$$

the direction of curvature for a positron travelling from the calorimeter to the source is identical to the direction of curvature for an electron travelling from the source to the calorimeters and vice versa. Charged particles travelling from the calorimeters to the foil can still be differentiated from source electrons by using timing and time of flight cuts.

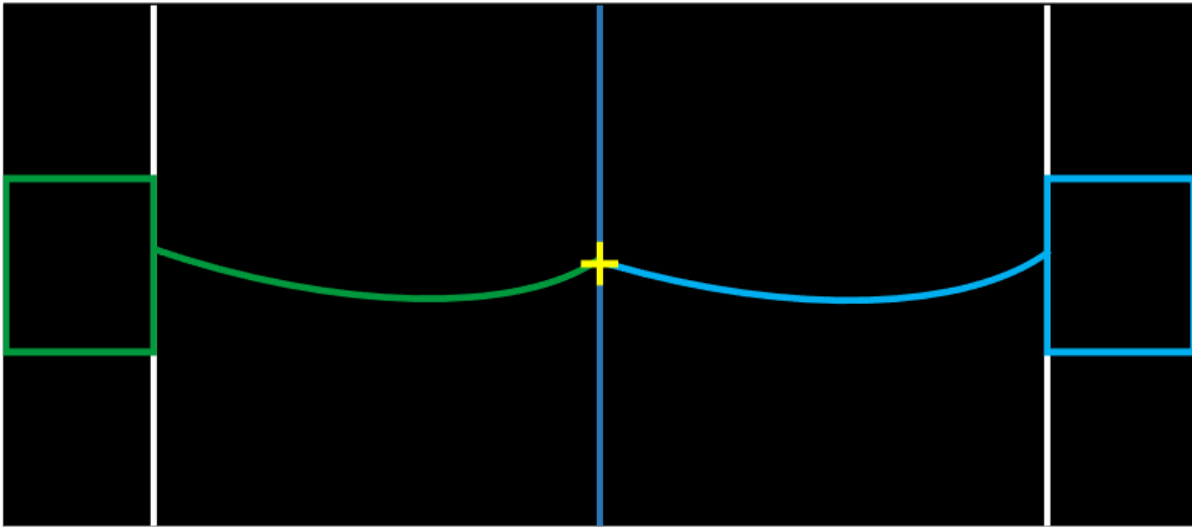


Figure 17: Representation of a reconstructed event with two charged particle tracks, the first belonging to an electron (blue track) and the second to a positron (green track), with an initial decay vertex on the source foil.

Electrons and positrons are identical under reconstruction until the charge is identified. For no field there is no separation of charge and so electrons and positrons cannot be differentiated. By separating electrons and positrons, double beta candidate events that involve positrons can be identified and removed.

#### 4.2.2 Gammas

When attempting to identify and measure the activities of selected backgrounds, it is important to establish the reconstructed topology of particles other than the electron and positron. Neutrinos are of course undetectable by the SuperNEMO demonstrator however the detector does allow for

both photons and alpha particles to be identified. The beta decay of  $^{208}\text{Tl}$  results in the emission of multiple photons alongside the beta electron and  $^{214}\text{Bi}$  beta decay is followed by the emission of a delayed alpha particle (figures ?? and ??). Establishing the additional particles that constitute these background decays helps to identify and remove them, reducing the total background count.

Unlike electrons and positrons, photons do not leave tracks in the detector and can only be identified by unassociated calorimeter hits, that is, calorimeter hits with no associated track or initial vertex. Furthermore, the time of flight cuts (internal and external probabilities) can be used to determine whether the timing of the unassociated calorimeter hit corresponds to that of a photon or an electron travelling from the source foil to the calorimeter. Calorimeter hits with energies lower than the detector trigger energy of 50 keV are labelled as noise regardless of whether there is an associated track or not. Reconstructed gammas often have noise hits close to the stricken calorimeter, however if the energies of these hits are below 50 keV, again the hits are labelled as noise. In the Falaise environment gammas can be identified by a yellow calorimeter hit with a dashed yellow originating at the particle source, as illustrated in figure ??.

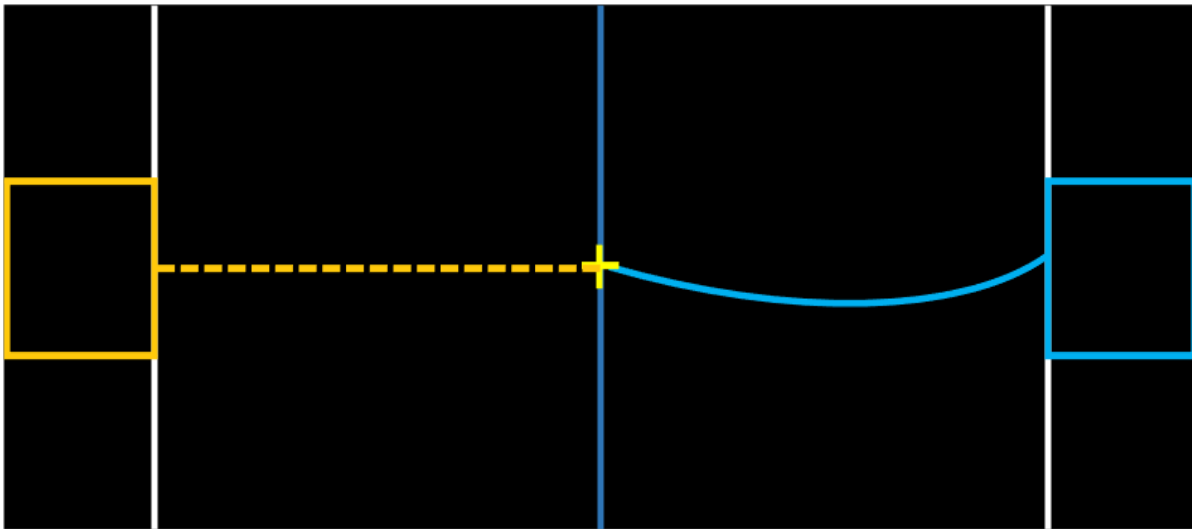


Figure 18: Representation of a reconstructed event with one electron (blue track) as well as a photon (yellow calorimeter hit with an unassociated/dashed track), with an initial decay vertex on the source foil.

### 4.2.3 Alphas

Alpha particles have short straight delayed tracks, confined to the tracker volume. As mentioned earlier in the chapter, the number of tracker hits for a reconstructed alpha can be fewer than the three tracker hits required for a charged particle track. For non delayed tracker hits that are not part of a larger track, the hits are registered as noise, whereas isolated delayed hits which are

reconstructed as alphas. The large mass of the alpha particle suppresses its propagation through the tracker and it rapidly loses its energy within the tracker in close vicinity to the source foil. The short red track in figure ?? demonstrates a typical reconstructed delayed alpha track alongside an electron. The main source of alpha particles for SuperNEMO is the beta decay of  $^{214}\text{Bi}$  to  $^{214}\text{Po}$ , which emits a delayed alpha,  $164.3 \mu\text{s}$  after the initial electron emission. By identifying reconstructed alpha particles the BiPo activity within the detector can be measured in the  $1e1\alpha$  channel.

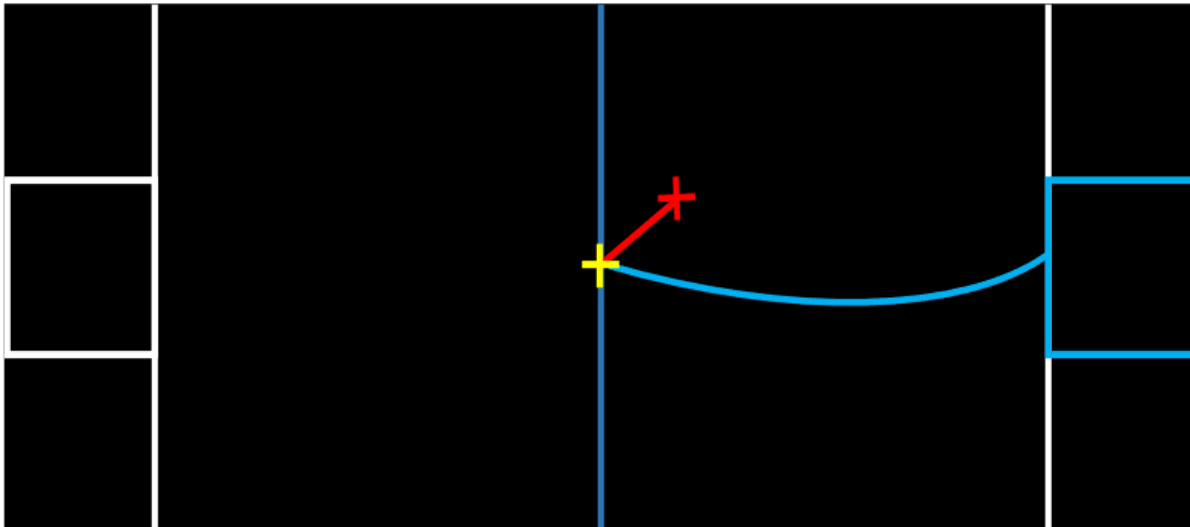


Figure 19: Representation of a reconstructed event with one electron (blue track) as well as an alpha (short red track), with an initial decay vertex on the source foil.



#### 4.2.4 $e\gamma$ Channels

The  $1e2\gamma$  channel is the main background channel for measuring the contamination of  $^{208}\text{Tl}$ . The  $1e2\gamma$  channel contains events with a single electron accompanied by two photons. The isotopic photon flux shown in figure ?? provides the chief photon energies and fluxes for the three external backgrounds. For  $^{208}\text{Tl}$ , the majority of the decays (99.8%) result in the emission of a high energy 2.6 MeV photon which is often emitted alongside a number of lower energy photons. The decay scheme of  $^{208}\text{Tl}$  is complicated (figure ??) and can result in more than two photons being emitted from the decay, however the most populated background channel is the  $1e2\gamma$  channel. Similarly,  $^{214}\text{Bi}$  decays can result in the emission of multiple photons although the addition of the delayed alpha in  $^{214}\text{Bi}$  beta decay allows for it to be measured in the  $1e1\alpha$  decay that will be discussed in the following section.

Isotope	$\gamma$ -ray Energy KeV	Flux $\text{cm}^{-2} \text{s}^{-1}$
$^{40}\text{K}$	1461	0.1
$^{208}\text{Tl}$	2615	0.04
$^{214}\text{Bi}$	1764	0.05
	1600	0.026
	1300	0.041
	1120	0.046
	609	0.109

Table 1: Simplified model of gamma flux in the LSM underground lab

By setting a high minimum energy the channel can be further optimised to measure  $^{208}\text{Tl}$ , removing some of the lower energy backgrounds from  $^{40}\text{K}$  and  $^{214}\text{Bi}$  which also contribute to the  $1e2\gamma$  channel. External  $eN\gamma$  backgrounds can be differentiated from the internal  $eN\gamma$  events by setting time of flight constraints set using the internal and external probability cuts from Sensitivity Module. Measuring  $eN\gamma$  channels combines the reconstructed topologies of the electron and gamma from sections ?? and ??, with the following additional constraints:

- i For internal events, the electron and gamma share a vertex, located on the source foil
- ii For external events, there must be an incident photon which interacts with the source foil to generate an electron

#### 4.2.5 $1e1\alpha$ Channel

The  $1e1\alpha$  channel is used to measure the contamination of beta decaying  $^{214}\text{Bi}$ , also known as the BiPo activity. The BiPo activity is measured throughout the detector, including the bulk and surface of the source foil and tracker wires. The rate of  $1e1\alpha$  decays and consequently the BiPo activity within the different parts of the detector can be used to determine the contamination level of  $^{214}\text{Bi}$  at those locations. For the  $1e1\alpha$  channel, the reconstructed variables outlined for the electron and alpha, in sections ?? and ??, are combined with the following additional constraints in order to probe the  $1e1\alpha$  channel:

- i There only being one prompt track
- ii The delayed alpha track occurs at least  $4\mu\text{s}$  after the prompt electron track
- iii The two tracks share a vertex

As no other SuperNEMO background produces a delayed alpha, the  $1e1\alpha$  channel can be precisely measured to determine the BiPo activity.

### 4.3 Internal/External Hypothesis

Any internal contribution, whether signal ( $0\nu\beta\beta$ ) or background, must originate from within the source foil and should not be induced by interactions originating from a source external to the  $^{82}\text{Se}$  source foil. Time of flight information is used to establish the origin of the initial decay. The time of flight cuts used are the internal and external probabilities, which estimate the probability that a reconstructed event was induced by a decay interior or exterior to the source foil. The external probability does not differentiate between an event originated from radon in the tracker or one of the many external background sources outlined earlier. For  $0\nu\beta\beta$ , time of flight information is most useful for identifying and removing double beta like events that may have originated from a source external to the source foil, whilst simultaneously the internal probability is used to ensure that any real double beta decays originated from within the source foil.

The internal hypothesis assumes a measured particles originated from within the source foil and the probability of this hypothesis can be calculated using the calorimeter hit timing of the particles. To calculate the internal probability, given two different calorimeter hit times  $t_1^{\text{meas}}$  and  $t_2^{\text{meas}}$ , first the theoretical time of flight  $t_i^{\text{tof}}$  is calculated using

$$t_i^{\text{tof}} = \frac{l_i}{\beta_i} \quad (2)$$

with  $l_i$  the length of the particle track which is curved for charged particles and straight line for photons. Additionally, for photons  $\beta_i = 1$  and for electrons is calculated using

$$\beta_i = \frac{\sqrt{E_i(E_i + 2m_e)}}{E_i + m_e} \quad (3)$$

with  $E_i$  the calibrated energy recorded by the calorimeter and  $m_e$  the rest mass of an electron. The emission time of a particle,  $t_i^{\text{int}}$ , takes into account the measured time in the calorimeter as well as the theoretical time of flight and is given as

$$t_i^{\text{int}} = t_i^{\text{meas}} - t_i^{\text{tof}} = t_i^{\text{meas}} - \frac{l_i}{\beta_i} \quad (4)$$

A  $\chi^2$  test representing the approximately Gaussian timing distribution is used with the corresponding  $\chi^2$  variable

$$\chi_{\text{int}}^2 = \frac{\left( \left( t_1^{\text{meas}} - \frac{l_1}{\beta_1} \right) - \left( t_2^{\text{meas}} - \frac{l_2}{\beta_2} \right) \right)^2}{\sigma_{t_1^{\text{int}}}^2 + \sigma_{t_2^{\text{int}}}^2} \quad (5)$$



where  $\sigma_{t_i^{\text{int}}}^2$  represents the variance of the emission timing  $t_i^{\text{int}}$ .  $\sigma_{t_i^{\text{int}}}^2$  depends on multiple factors including the uncertainties on the measured time, particle speed and distance travelled. For photons, the particle speed is  $c$  and so there is no uncertainty on this value, however the uncertainty surrounding the path length is unknown as photons are not tracked in SuperNEMO.

$\chi_{\text{int}}^2$  is converted into a probability by transforming the Gaussian distribution into a flat distribution between 0 and 1. The internal probability is therefore defined as

$$P(\chi_{\text{int}}^2) = 1 - \frac{1}{\sqrt{2\pi}} \int_0^{\chi_{\text{int}}^2} x^{-\frac{1}{2}} e^{-\frac{x}{2}} dx \quad (6)$$

Unlike the internal hypothesis, the external hypothesis assumes an incident external photon interacts with the detector to produce either a  $1e1\gamma$  event or a crossing electron. The external background results in the generation of an event in the  $2e$  channel via a number of mechanisms that will be outlined later on. Calculating the external probability is done in a similar manner to the internal probability, but the time of flight  $t^{\text{tof}}$  is given as

$$t^{\text{tof}} = \frac{l_1}{\beta_1} + \frac{l_2}{\beta_2} \quad (7)$$

which sums the timing for both particle tracks.

The  $\chi^2$  for the external hypothesis is then

$$\chi_{\text{ext}}^2 = \frac{\left( (t_2^{\text{meas}} - t_1^{\text{meas}}) - \left( \frac{l_1}{\beta_1} + \frac{l_2}{\beta_2} \right) \right)^2}{\sigma_{t_1^{\text{ext}}}^2 + \sigma_{t_2^{\text{ext}}}^2} \quad (8)$$

where  $\sigma_{t_i^{\text{int}}}^2$  is the equivalent variance of emission for the external hypothesis. Like the internal probability in equation ??, the external probability is calculated with

$$P(\chi_{\text{ext}}^2) = 1 - \frac{1}{\sqrt{2\pi}} \int_0^{\chi_{\text{ext}}^2} x^{-\frac{1}{2}} e^{-\frac{x}{2}} dx \quad (9)$$

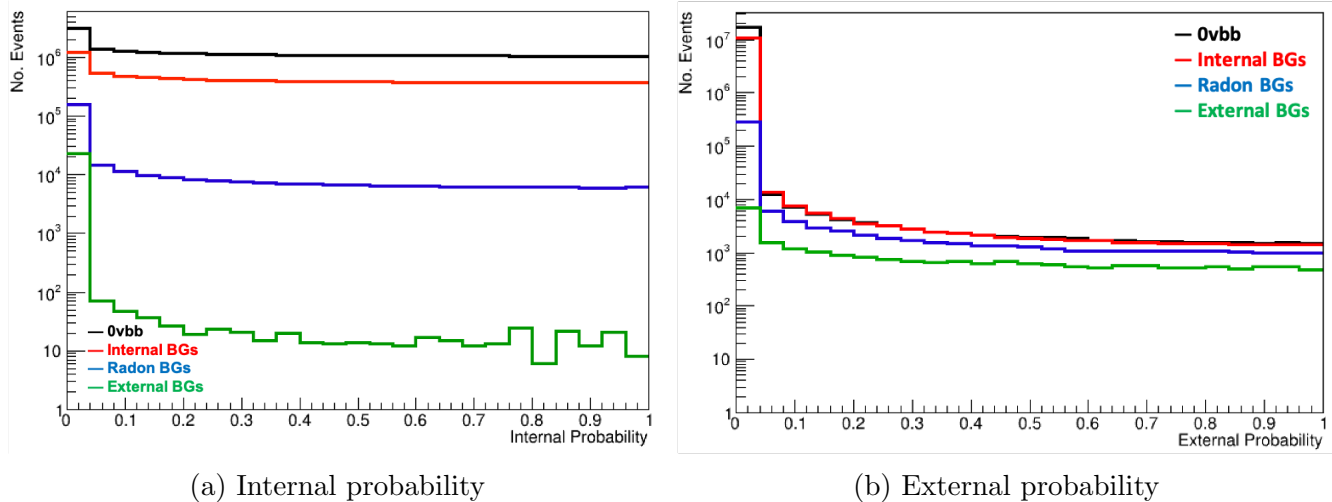


Figure 20: Internal probability for  $0\nu\beta\beta$ , internal, radon and external backgrounds with reconstructed 2e topologies. The internal probability distributions were calculated using the equation above

## 4.4 Identifying Double Beta Events



The search for  $^{82}\text{Se}$  neutrinoless double beta decay is measured in the two electron channel, but as mentioned previously not all events found in the two electron channel are not necessarily from real double beta decays and may in fact materialise from particular background decays. The reconstruction topology of electrons was established in section ??, so for a double beta candidate event in the 2e channel, the reconstructed topologies of two electrons are combined with additional constraints, all of which are outlined below. The double beta decay criterion together form the basis of the cut flow and takes the form of data cuts that are applied to the reconstructed Sensitivity Module nTuples to determine the total number of double beta candidate events. The requirements established for double beta candidate events in the two electron channel are selected in order to maximise the reconstruction efficiency of true double beta decays, whilst reducing the prevalence of background induced two electron events.



### 4.4.1 2e Channel Selection

#### i Two calorimeter hits

Two calorimeter hits above 50 keV, with at least one hit above 150 keV, measuring the energies of the two double beta decay electrons. The minimum energy requirement is determined by the trigger energy of the detector.

#### ii Two tracker clusters and two tracks

Two tracks, derived from two tracker clusters are selected to represent the tracks of the two emitted electrons during double beta decay.

iii Each track associated to a unique calorimeter

Each track is associated to a calorimeter ensuring the two beta electron tracks correspond to the two calorimeter hits. Additionally the two calorimeter hits belong to two unique calorimeters. One of the main benefits of SuperNEMO is that it allows the energy of each individual electron to be measured which can only be achieved when electrons hit separate calorimeters.

iv Two vertices on the source foil

The two electron vertices should be located on the source foil, ensuring a reconstructed path from the foil, through the tracker and finally into the calorimeters for the two electrons.

v Internal and External Probability

The timing of the calorimeter hits must be within a certain boundary to ensure the electrons originated from within the source foil and did not enter the tracker from an external source. Internal and external probability essentially act as time of flight cuts.

vi No Positrons

The double beta decay charged particle tracks can belong to either electrons or positrons. The charge of each track can be identified from the curvature of the track so electrons and positrons can be differentiated. Identifying both tracks as electrons is the final step for  $2e$  selection.

#### 4.4.2 $2e$ Channel Optimization

The  $2e$  channel cuts help to identify double beta candidate events however additional cuts are necessary for improving the overall detection efficiency of double beta decay simulations. Three additional optimization cuts are,

i Maximum vertex separation

The maximal separation between the vertices is  $\Delta R < 1\text{cm}$  and  $\Delta Z < 3\text{cm}$ , where  $\Delta R$  represents the radial separation and  $\Delta Z$  the vertical separation.

ii No delayed alphas

No delayed/alpha tracks.

iii Energy Window or Region Of Interest (ROI)

No events are allowed outside of the predefined energy window (ROI). The nominal ROI is 2.8 - 3.2 MeV for  $^{82}\text{Se}$ , however the ROI itself is subject to change via optimization.

Together, the two electron channel and optimization cuts combine to form the double beta decay cut flow, which is sequentially applied to reconstructed data in order to calculate the number of remaining double beta candidate events and the corresponding detection efficiency. For both signal and background simulations, the cut flow extracts the efficiency of reconstructing double beta candidate events from the initial simulated isotope. This efficiency is used to calculate the total number of expected events in the  $^{82}\text{Se}$  ROI from a particular decay and the proportionate contribution of the decay to the  $^{82}\text{Se}$  neutrinoless double beta decay sensitivity.

## 4.5 Number of Expected Events

The number of expected events provides an estimate of the total number of decays we expect from individual radioactive sources during the detectors operational lifetime. The number of expected events is calculated differently for backgrounds simulated in different parts of the detector in order to correctly represent the exposure which changes throughout the detector. The ratio of successfully reconstructed events in a given channel, from a known number of Monte Carlo simulations is denoted the detection efficiency and is given as the following,

$$\epsilon = \frac{N_{MC}}{N_{TOTMC}} \quad (10)$$

with  $N_{MC}$  equal to the number of successfully reconstructed candidate events and  $N_{TOTMC}$  equal to the total number of simulated events. The number of expected events of  $^{82}\text{Se}$  two neutrino double beta decay, in the source foil, is given by,

$$N_{2\nu\beta\beta} = \frac{N_A \times \ln 2 \times \epsilon \times m \times t}{T_{1/2}^{2\nu\beta\beta} \times M(^{82}\text{Se})} \quad (11)$$

where  $N_A$  is Avogadro's constant,  $\epsilon$  is the previously quoted reconstruction efficiency ratio,  $m$  is the total mass of the  $^{82}\text{Se}$  source foil (6.23 Kg),  $t$  is the total run time of the experiment,  $T_{1/2}^{2\nu\beta\beta}$  is the half life of  $^{82}\text{Se}$  and  $M(^{82}\text{Se})$  is the mass number for  $^{82}\text{Se}$ . For other internal backgrounds, such as  $^{208}\text{Tl}$  and  $^{214}\text{Bi}$ , the number of expected events is

$$N_i = A_i \times \epsilon_i \times m \times t \quad (12)$$

with  $A_i$  and  $\epsilon_i$  designated as the activity and reconstruction efficiency respectively, for background  $i$ .

Radon induced backgrounds are calculated using the activity of the background within the volume of the tracker chamber. The volume of the tracker replaces the source foil mass in equation ?? and so the number of expected events for Radon simulations is given by,

$$N_i = A_i \times \epsilon_i \times V \times t \quad (13)$$

with  $V$  as the volume of the tracker chamber. External backgrounds were only simulated on the PMT glass bulbs, so the activity is a proportion of the total activity from the entire PMTs. The number of expected events for external backgrounds is given by,

$$N_i = A_{Glassbulb,i,j} \times \epsilon_i \times t \quad (14)$$

with  $A_{Glassbulb,i,j}$  the activity of the PMT glass bulb for a given background  $i$  and PMT location  $j$ .

The number of expected events represents the total contribution of a decay to a particular channel. For SuperNEMO, the signal detection efficiency and the contribution of different backgrounds in the 2e channel are used in order to estimate the overall  $0\nu\beta\beta$  half-life sensitivity of the demonstrator.

## 4.6 Half-Life Estimation

The half-life estimate of  $0\nu\beta\beta$  represents the sensitivity of the experiment to neutrinoless double beta decay. A greater half-life sensitivity demonstrates an improved probability of observing neutrinoless double beta decay, whilst also setting improved limits for both the neutrinoless and two neutrino decay.

There are various methods to approximate the half-life, the most common of which use the entire energy spectrum of both signal and background, attempt to separate them, and finally determine the signal and background contributions to the half-life limit. In this thesis, some of the methods used to determine the sensitivity to neutrinoless double beta decay involve the application of a 'window', that is, a selected energy region that comprises part of the energy spectrum, focused around the peak signal energy. For  $^{82}\text{Se}$  neutrinoless double beta decay, the initial window was established as 2.8 to 3.2 MeV (highlighted in figure ??), encompassing the  $^{82}\text{Se}$  Q value. Window methods are less precise than the more thorough complete energy spectrum methods, however as the objective of this thesis is to determine which of the three magnetic field is most suitable for detector operation, a less precise but relative study between the three magnetic fields is beneficial. ~~By attempting to compare the relative performance of the three magnetic fields, the precision of the sensitivity estimation can be compromised in order to increase the speed of the analysis.~~

### 4.6.1 Gaussian Window Approximation

As mentioned, it is possible to estimate the  $0\nu\beta\beta$  half-life using both a full energy spectrum or window energy method. The first window approximation is the Gaussian window approximation

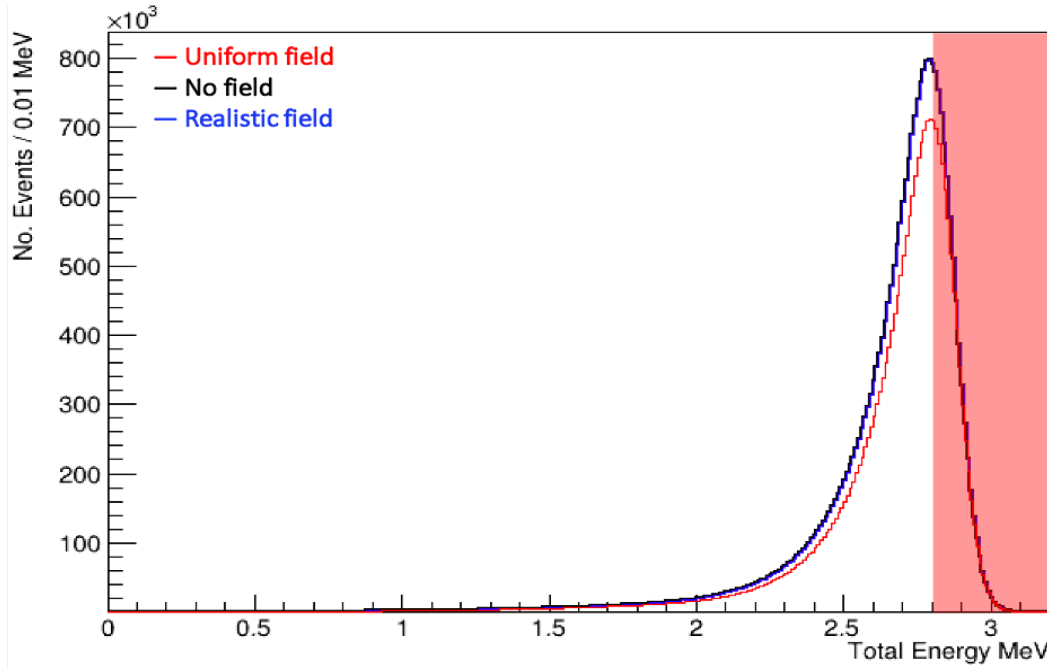


Figure 21: Energy spectra of  $0\nu\beta\beta$  for all three magnetic field configurations, highlighting the region of interest (2.8 - 3.2 MeV)

which is particularly useful for studies with low numbers of expected backgrounds. Additionally, although not as precise as the other methods, the Gaussian approximation is a simple and fast approach for comparing the three magnetic field configurations. For the Gaussian approximation,  $T_{1/2}^{0\nu}$  is defined as,

$$T_{1/2}^{0\nu} > 4.16 \times 10^{26} \text{yr} \left( \frac{\epsilon a m t}{M(^{82}\text{Se})} \right) \left( \frac{1}{1.64 \sqrt{N_B}} \right) \quad (15)$$

with  $\epsilon$  the efficiency of detecting  $0\nu\beta\beta$  (from equation ??),  $a$  the isotopic abundance (given as 1 for the refined source foil),  $m t$  the exposure,  $M(^{82}\text{Se})$  the  $^{82}\text{Se}$  mass number and  $N_B$  the number of expected background events. The  $\sqrt{1.64}$  denominator term represent a 90% confidence level (CL).

From equation ??, increasing the signal detection efficiency and reducing the background increases the half-life limit. Moreover, the non-linear relationship between the signal and background can result in an increase in sensitivity when both the signal and background are reduced as long as the reduction in background events is not outweighed by a large reduction in the signal detection efficiency. Practically, additional data cuts and optimization of the window region are two approaches to maximising the half-life sensitivity, both of which will be investigated hereafter.



### 4.6.2 Poissonian Window Approximation

An alternative to the Gaussian approximation is the Poissonian approximation which provides greater precision for an analysis with increased statistical data. Firstly, the half-life formula is derived, starting with the exponential decay of a radioactive isotope, given as,

$$N(t) = N(0)e^{-\lambda t} \quad (16)$$

with  $N(t)$  the number of remaining atoms of the isotope at time  $t$ ,  $N(0)$  the number of atoms at the beginning of the experiment and  $\lambda$  the decay constant.  $\lambda$  is related to the half-life  $T_{1/2}$  by the following

$$\lambda = \frac{\ln(2)}{T_{1/2}} \quad (17)$$

The half-life of two neutrino  $^{82}\text{Se}$  double beta decay is approximately of the order  $10^{20}$  years and even greater for neutrinoless double beta decay so equation ?? can be Taylor expanded in  $\lambda t$  to give the approximation

$$e^{-\lambda t} \simeq (1 - \lambda t) \quad (18)$$

The number of observed events can therefore be written as

$$N_{\text{obs}} = \epsilon N(0) (1 - e^{-\lambda t}) \simeq \epsilon N(0) \lambda t = \epsilon N(0) \frac{\ln(2)}{T_{1/2}} t \quad (19)$$

with the  $\epsilon$  the detection efficiency of  $0\nu\beta\beta$  and  $t$  the running time of experimentation. The number of atoms at the beginning of the experiment,  $N(0)$  is given by

$$N(0) = \frac{N_A m}{A} \quad (20)$$

and by inserting the definition of  $N(0)$  into equation ??, the half life of  $0\nu\beta\beta$  can be calculated using

$$T_{1/2} = \frac{\epsilon}{N_{\text{obs}}} \frac{N_A m}{A} \ln(2) t \quad (21)$$

The selected energy window is equivalent for the two sensitivity approaches, however, unlike the Gaussian approximation, equation ?? uses the number of observed events,  $N_{\text{obs}}$ , instead of the

number of expected backgrounds  $N_B$ , encompassing both the signal and background distributions. In order to estimate the half-life in equation ??, the number of observed events is first calculated and then entered into the equation. For this work, the methods used to calculate the number of observed events include the Helene method from [?] and the Feldman-Cousins method found in [?], both of which are outlined below.

### 4.6.3 Helene Method

The Helene method described in [?] outlines three different variables:

- A - which is the upper limit of the peak and the value used for  $N_{obs}$ .
- B - the number of background events
- C - the total event count in a known bin

Using a defined confidence limit (usually 90%), the value for A can be determined from the graphs shown below, where B takes the X axis and C is the curve from which the corresponding value of A can be extrapolated from. In this case  $C \approx B$  as the number of backgrounds is calculated the region of interest which is also the binned region for C.

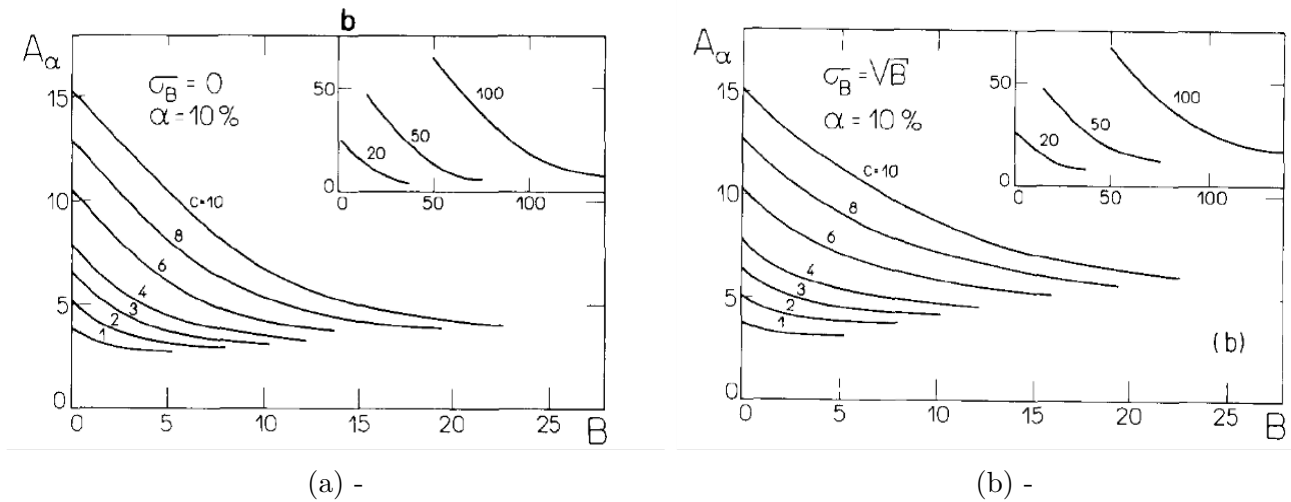


Figure 22: Helene where  $\sigma_b$  is the error on the background and  $\alpha$  is equal to 1 - CL

### 4.6.4 Feldman-Cousins

The Feldman-Cousins approach is often used to quote limits on the size of a signal, given the background contamination. For a known background and confidence limit, for a Poissonian signal



such as equation ??, Feldman-Cousins provides an estimate for  $N_{\text{obs}}$  which is then used to calculate equation ??.

$$P(s | b, N) = \frac{e^{-(s+b)}(s+b)^N}{N!} \quad (22)$$

## 4.7 Limit Setting Procedure

## 4.8 Minimum Detectable Activity

In this thesis, the definition used for the minimum detectable activity is the definition given in ‘Radiation Detection and Measurement’ by G. F. Knoll. Knoll uses a binary pretence of whether the detector output represents a background only or that there is also the presence of signal.

the probability of a false positive is established as the probability a signal event is present even though only background is present and a false negative is established as the probability a signal event is misidentified as a background.

To determine the presence of signal, a critical count number  $n_c$  is defined and if the total observed count number is greater than  $n_c$ ,

the definition of Minimum Detectable Activity (MDA) given in ‘Radiation Detection and Measurement’ by G. F. Knoll is used

G. Knoll, Radiation Detection and Measurement, ISBN-9780470131480 (2000)

\*\*\* Yet to complete \*\*\*



# Chapter 5

## Double Beta Decay Event Selection

The sensitivity to neutrinoless double decay is the primary metric of success for the magnetic field analysis described in this work. The results from the double beta decay simulations (signal) will be discussed, including the impact of the 2e topology cuts from chapter ?? on the concurrent and final detection efficiency for each of the three magnetic field scenarios. For the  $0\nu\beta\beta$  analysis,  $2\nu\beta\beta$  is treated as a background and contributes to the total background contamination. The high energy window/region of interest established in the previous chapter ensures the contamination of  $2\nu\beta\beta$  is suppressed however a very small number of  $2\nu\beta\beta$  events still remain. Additionally, the scenario of **an ideal** SuperNEMO detector will be discussed, that is, a radiopure detector with only  $2\nu\beta\beta$  as an irreducible background to  $0\nu\beta\beta$ . With improved processing methods it may be feasible to reduce all other sources of backgrounds close to zero, providing the **ideal detector conditions** for probing neutrinoless and two neutrino double beta decay.

### 5.1 Neutrinoless Double Beta Decay ( $0\nu\beta\beta$ )

The primary goal of the SuperNEMO experiment is to **detect and measure the neutrinoless double beta decay of  $^{82}\text{Se}$** , however, more realistically, it is to set improved limits on the decay half-life. Parallel to this, SuperNEMO aims to improve on the previous half-life measurement for the two neutrino decay of  $^{82}\text{Se}$  and increase the precision of the two neutrino decay nuclear matrix elements. In order to determine the neutrinoless double beta decay sensitivity, the detection efficiency of  $0\nu\beta\beta$  (equation ??) must first be extracted using the 2e topology cut flow from section ??.



For each of the three magnetic fields,  $10^8$  **events** were simulated using the official Falaise 4.0.0 reconstruction with both helical and straight line fitting available. As mentioned previously, the cut flow is applied to the Sensitivity Module nTuples in order to measure the change in detection efficiency with each consecutive cut. The number of remaining events after the final cut is used to calculate the detection efficiency as shown in equation ??.



Cut Descriptions	Magnetic Field Configuration		
	Uniform Field	No Field	Realistic Field
Only two calorimeter hits above 50keV, at least one >150keV	0.562	0.594	0.589
Two tracker clusters with 3 or more cells	0.380	0.446	0.436
Two reconstructed tracks	0.378	0.443	0.433
Remove events with multiple hits to the same calorimeter	0.373	0.438	0.429
Each track associated to a calorimeter	0.338	0.400	0.390
Two vertices on the source foil	0.337	0.399	0.389
Vertex $\Delta R < 1\text{cm}$ and $\Delta Z < 3\text{cm}$ (separation between vertices)	0.240	0.281	0.274
Internal Probability >1% and External Probability <4%	0.226	0.265	0.259
Delayed Alpha Hits (no hits allowed after 13 $\mu\text{s}$ )	0.226	0.265	0.259
Remove Positrons (unavailable for no field)	0.211	- <sup>†</sup>	0.179
Energy Cut (between 2.8 and 3.2 MeV)	0.0653	0.0790	0.537

Table 2:  $0\nu\beta\beta$  cut flow for the three B field configurations. Each row lists a short description of the cut as well as the concurrent detection efficiency.

<sup>†</sup>For no field, the no positron cut is not applied as without a magnetic field, the charges of the particle tracks are indeterminable. The magnetic field curves electrons and positrons in opposite directions as a result of their differing charges and so without a magnetic field, the charged particle tracks are expected to be straight, ignoring any low energy scattering within the tracker.

The breakdown of the  $0\nu\beta\beta$  cut flow is provided in table ??, illustrating how the detection efficiency changes with each sequential cut. A short description of each of the cuts is provided. The cut flow follows the ordering shown in section ??, however the three additional optimization cuts; the maximum vertex separation, no delayed tracks and the energy window (or ROI) are added to the cut flow as cuts seven, nine and eleven respectively. The order of the cut flow is important for studying the impact of each individual cut on the concurrent detection efficiency and importantly, understand how the different magnetic fields influence the overall final detection efficiency. In the following section, a short explanation for the difference in detection efficiency between the three fields is given for the most impactful cuts.

### 5.1.1 Most Impactful Cuts

	Detection Efficiency $\epsilon$		
	Uniform Field	No Field	Realistic Field
No calorimeter hits	0.049	0.041	0.042
1 calorimeter hit	0.307	0.273	0.278
2 calorimeter hits	0.562	0.594	0.589
3+ calorimeter hits	0.081	0.092	0.090

Table 3: Distribution of calorimeter hits for reconstructed  $0\nu\beta\beta$  events. The numbers provide the concurrent detection efficiency from the original  $10^8$  simulated events which have the selected number of reconstructed calorimeter hits.

Applying the two calorimeter cut results in large reduction in the number of remaining events for all three magnetic fields. For the uniform field, a larger reduction is observed, primarily caused by the increased magnetic field strength increasing the length charged particles need to travel to reach a calorimeter. From table ??, the reduced number of two calorimeter hits with the uniform field gives rise to an increased number of events with one or fewer calorimeter hits. Of the 30.7 million uniform field events with 1 calorimeter hit, over 70% have at least two charged particle tracks, illustrating that the electrons are being reconstructed but are not reaching the calorimeters as often. Similarly, for the two clusters cut, the increased field strength of the uniform field results in a greater number of events with 3+ clusters.

Additional noteworthy cuts include the vertex separation, no positron and finally the ROI window cut. The vertex separation cut applies a harsher constraint compared to previous studies. In [?],  $\Delta R$  is required to be  $<6\text{cm}$  and  $\Delta Z <7\text{cm}$ , culminating in over 95% of double beta candidate events from the source foil surviving the cut, compared to the approximately 70% survival rate with  $\Delta R <1\text{cm}$  and  $\Delta Z <3\text{cm}$ . The appointed constraint is a consequence of the expected spatial resolution of roughly 8% , with an effective maximum longitudinal resolution of  $\approx 1.1\text{ cm}$  at the mid length of a cell [?].

The penultimate no positron cut is used to remove double beta candidate events that have at least one charged particle labelled as a positron. As previously stated, the no positron cut is inapplicable for the no field scenario. Moreover, the cut removes a large number of events for the realistic field, around 30%, and close to 7% of events for the uniform field, as the increased field strength increases the efficiency of labelling charged particles correctly. Finally, the energy window

removes the majority of remaining events as the ROI encompasses only a small segment of the overall energy spectrum. Between the three magnetic fields, the shape of the spectra is unchanged, resulting in a similar proportion of events removed.

## 5.2 Two Neutrino Double Beta Decay ( $2\nu\beta\beta$ )

Cut Descriptions	Detection Efficiency $\epsilon$		
	Uniform Field	No Field	Realistic Field
Only two calorimeter hits above 50keV, at least one >150keV	0.237	0.287	0.279
Two tracker clusters with 3 or more cells	0.147	0.205	0.195
Two reconstructed tracks	0.146	0.204	0.194
Remove events with multiple hits to the same calorimeter	0.143	0.201	0.191
Each track associated to a calorimeter	0.125	0.179	0.170
Two vertices on the source foil	0.125	0.178	0.169
Vertex $\Delta R < 1\text{cm}$ and $\Delta Z < 3\text{cm}$ (separation between vertices)	0.072	0.101	0.096
Internal Probability >1% and External Probability <4%	0.068	0.095	0.090
Delayed Alpha Hits (no hits allowed after 13 $\mu\text{s}$ )	0.068	0.095	0.090
Remove Positrons (unavailable for no field)	0.063	- <sup>†</sup>	0.060
Energy Cut (between 2.8 and 3.2 MeV)	$3 \times 10^{-8}$	$2 \times 10^{-8}$	$1 \times 10^{-8}$
Number of Expected Events	0.15 $\pm 0.09$	0.10 $\pm 0.07$	0.05 $\pm 0.05$

Table 4:  $2\nu\beta\beta$  cut flow and number of expected events for all three magnetic field configurations. Each row lists a short description of the cut as well as the concurrent detection efficiency for each magnetic field.

<sup>†</sup> No positron cut for no field scenario.

The cut flow for  $2\nu\beta\beta$  double beta candidate events is shown in table ??, alongside the number of expected events with 2.5 years of exposure. The overall detection efficiency is significantly lower

for  $2\nu\beta\beta$  compared to  $0\nu\beta\beta$ , particularly in the ROI, where the detection efficiencies are of the order  $10^{-8}$ . A low detection efficiency for  $2\nu\beta\beta$  is important when measuring the sensitivity to neutrinoless double beta decay as  $2\nu\beta\beta$  is the single irreducible background for the neutrinoless search.

### 5.2.1 Ideal Detector Conditions

Prior to investigating the contributions from the other background sources, it is useful to consider the case of the ideal detector, which only includes the irreducible  $2\nu\beta\beta$  as a background. Although SuperNEMO has a number of different backgrounds that contribute towards the  $^{82}\text{Se}$  ROI, from internal, radon and external sources, it may be possible to further reduce and perhaps eliminate all of the reducible backgrounds. To reduce the internal contamination, the source foils can undergo increased processing which is made easier by the modular structure of the SuperNEMO demonstrator, allowing the source foils to be easily removed and replaced. Radon and external backgrounds can be reduced by the improving the radon flushing inside the tracker and increasing shielding prowess respectively. For the ideal detector this would result in a reduction or elimination of all backgrounds leaving only the irreducible  $2\nu\beta\beta$ . Using the associated cut flows and expected events, the sensitivity of the idealistic detector setup with no reducible backgrounds is shown in figure ??.

	Sensitivity $\times 10^{24}$		
	Uniform Field	No Field	Realistic Field
Sensitivity Gaussian $e^{24}$	7.966	11.803	1.135
Sensitivity Helene ( $A \approx 1$ )	-	-	-
Sensitivity Feldman-Cousins	2.217	2.625	1.747
MDA	-	-	-

Table 5:  $0/2\nu\beta\beta$  detection efficiency as well as the number of expected events for  $2\nu\beta\beta$

As mentioned in section ??, the Poissonian approximation provides greater precision with higher statistics but struggles with a number of expected backgrounds close to zero. However for a relative study between the three magnetic field scenarios it can still be useful for determining which magnetic field delivers the greatest detector sensitivity. Of the three fields, no field has the highest sensitivity with all three estimation methods, culminating in a sensitivity of  $1.180 \times 10^{25}$  with the Gaussian approximation, owing to the much greater detection efficiency of  $0\nu\beta\beta$ .

### 5.3 $0/2\nu\beta\beta$ Distributions

The sum of the two electron distribution is shown in figure ???. For neutrinoless double beta decay, the total energy correlates well with the expected Landau distribution seen for charged particles traversing a thin film. The distribution peaks around the decay energy of  $^{82}\text{Se}$  (\*\*reference Q energy from intro\*\*) and the Landau tail extends back to the 200 keV trigger energy. The shape of the distribution is unchanged between the three magnetic fields. The tail of the two neutrino distribution barely penetrates into the  $^{82}\text{Se}$  ROI, resulting in the low detection efficiencies for the three fields as shown in table ?. The majority of  $2\nu\beta\beta$  events are found at lower energies, with the peak of the distribution close to 1 MeV when taking into account the undetectable energies carried away by the neutrinos.

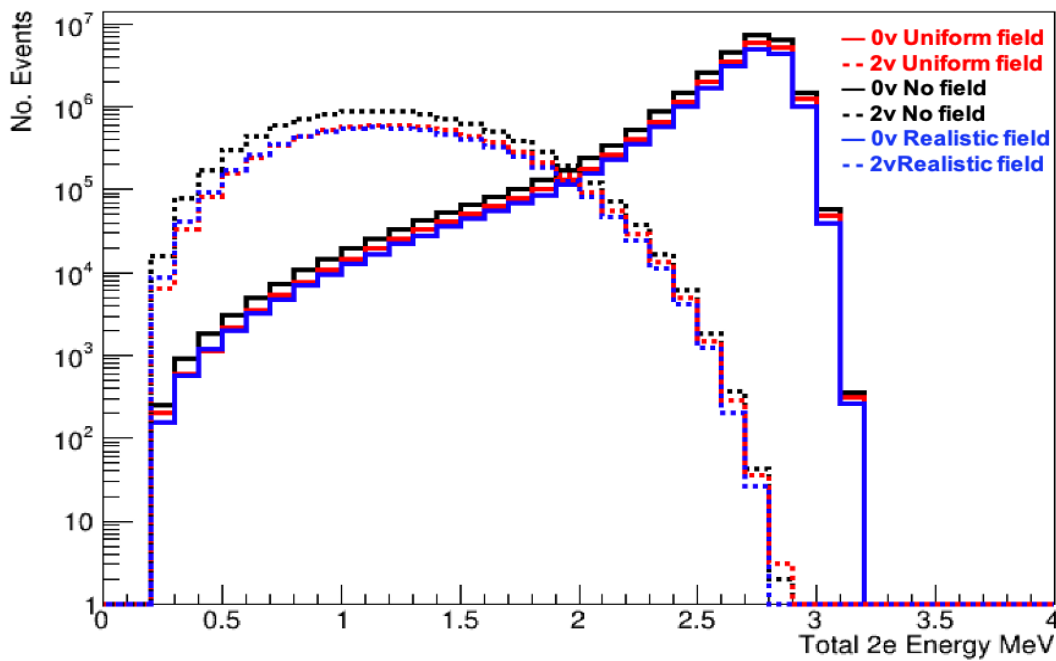



Figure 23: 2e energy spectra for  $0/2\nu\beta\beta$  double beta candidate events.

SuperNEMOs modular structure provides the ability to reconstruct the entire topology of individual particles. One of the most important variables for studying the intermediate decay mechanism of  $^{82}\text{Se}$  double beta decay, is the single electron energy.. The single electron energy distribution is presented in figure ??, for both  $0$  and  $2\nu\beta\beta$ . For  $0\nu\beta\beta$ , the single electron energy distribution peaks and is symmetric around 1.3 MeV for all three magnetic fields. Whereas for  $2\nu,\beta\beta$  the distribution peaks at 0.4 MeV and is skewed towards  $E_{\text{electron}} < 1$  MeV. Again, the distribution shape is independent of the magnetic field choice, for both the neutrinoless and two neutrino decays. 

The two electron angular distribution is important for distinguishing the different  $0\nu\beta\beta$  mechanisms discussed in chapter \*\*reference introduction\*\*. The cosine( $\theta$ ) curve for  $0\nu\beta\beta$  is expected

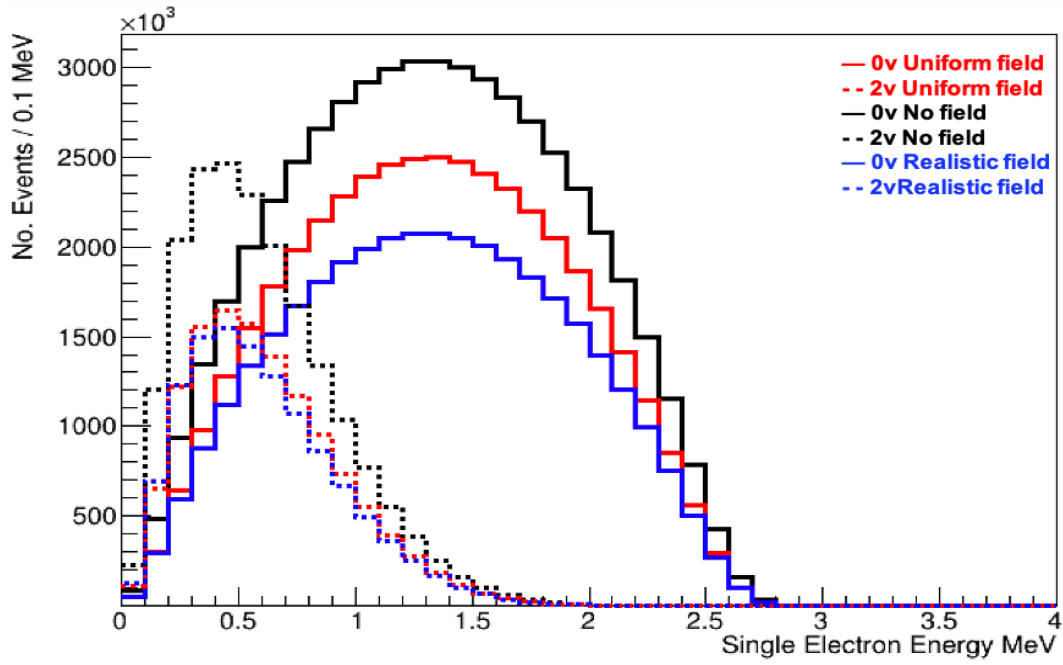


Figure 24: Single electron energy spectra for  $0/2\nu\beta\beta$  double beta candidate events.

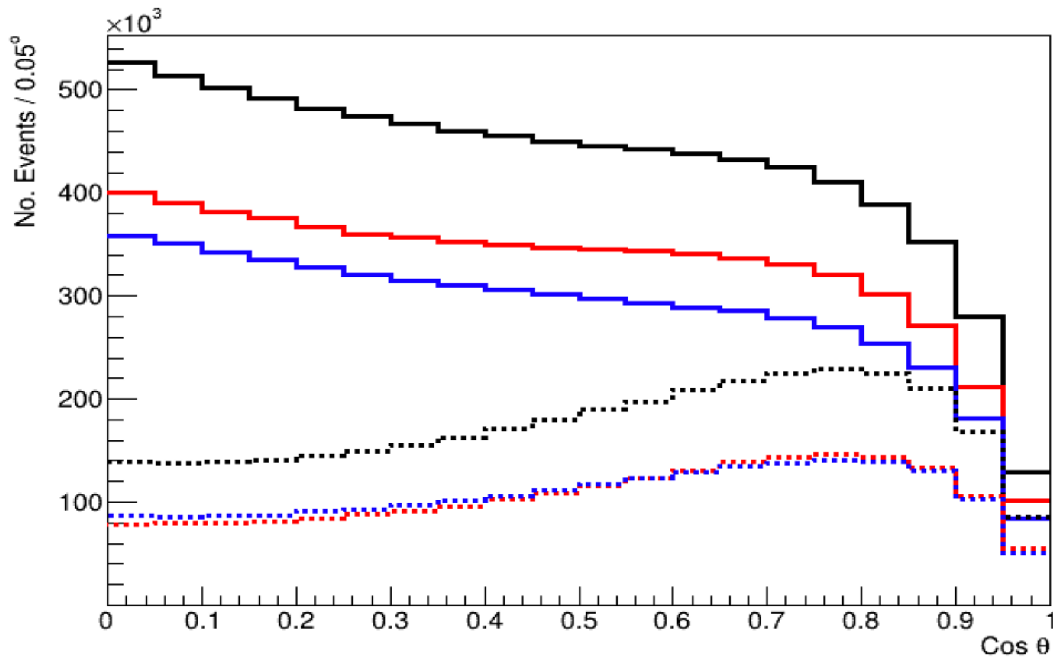


Figure 25:  $\text{Cos}\theta$  spectra for  $0/2\nu\beta\beta$  double beta candidate events of all energies.





to follow a  $1 - \cos(\theta)$  distribution, however, as shown in figure ??, the number of events reduces as you get closer to  $\cos(\theta) = 0$ . For  $2\nu\beta\beta$ , the angular distributions skew towards lower angles, peaking at  $\cos(\theta) = 0.8$ . Again, the different magnetic fields do not bring about any change in the shape of the distribution.

## 5.4 Summary of Double Beta Decays

	Magnetic Field Configuration		
	Uniform Field	No Field	Realistic Field
$0\nu$ Detection Efficiency	0.0653	0.0790	0.0537
$2\nu\beta\beta$ Detection Efficiency	$3 \times 10^{-8}$	$2 \times 10^{-8}$	$1 \times 10^{-8}$
$2\nu\beta\beta$ Number of Expected Events	$0.15 \pm 0.09$	$0.10 \pm 0.07$	$0.05 \pm 0.05$
Sensitivity Gaussian $e^{24}$	7.966	11.803	1.135
Sensitivity Helene	-	-	-
Sensitivity Feldman-Cousins	2.217	2.625	1.747
MDA	-	-	-

Table 6:  $0/2\nu\beta\beta$  detection efficiency as well as the number of expected events for  $2\nu\beta\beta$

Of the three magnetic field configurations, the no field scenario maintains the greatest detection efficiency after applying the two electron cut flow outlined in section ?. Additionally, as a result of the high energy region of interest, the two neutrino detection efficiency is suppressed and accordingly the background contribution is extremely small. When considering the ideal detector scenario, the highest sensitivity is achieved for no field as a result of the superior 0.0790 detection efficiency. The Poissonian approximations of the sensitivity are imprecise for low background statistics, nonetheless, when taking into account the additional background sources, the precision should improve. Although the idealistic detector assumes zero non DBD backgrounds, the current demonstrator module has non-zero background contributions from all different parts of the detector. To measure the sensitivity inclusive of the other backgrounds, the same procedure carried out to determine the  $2\nu\beta\beta$  background count will be used for the remaining reducible backgrounds.

# Chapter 6

## Estimation of Backgrounds for SuperNEMO



As demonstrated in section ??, the sensitivity to neutrinoless double beta decay is inversely proportional to the background level, therefore in order to maximise the sensitivity, the background contamination should be reduced or eliminated without significantly suppressing the signal detection efficiency. Additionally, the non-linear dependence between the sensitivity and background indicates an increase in sensitivity can still be achieved with a reduced signal detection efficiency as long as the background is reduced proportionally. The sensitivity can also be improved with an increased exposure (Activity  $\times$  Time), usually involving an increase in the source mass and run time of the experiment. Nevertheless, for the SuperNEMO demonstrator, the initial run time is expected to be around 2.5 years, with a  $^{82}\text{Se}$  source foil mass of 6109.62g \*\*\*ref demonstrator chapter\*\*\*.

This chapter is devoted to identifying the different sources of backgrounds as well as concluding how they materialise within the different parts of the detector. The topology of double beta decay candidate events is mentioned alongside the mechanisms underlying the production of double beta candidate events from non double beta decay backgrounds. For the three magnetic fields, the contribution of the different backgrounds to the  $0\nu\beta\beta$  sensitivity will be determined and the most significant backgrounds will be identified. To estimate the different background contributions, they will first be divided by their location. As stated in chapter 3, the three background locations are internal, radon and external, which will first be examined separately and combined to give the total background contamination for each magnetic field configuration.

In the previous chapter, the sensitivity for the ideal detector, with zero non double beta decaying backgrounds, was investigated. In this chapter, the non  $2\nu\beta\beta$  background contributions will be integrated into the total background count in order to calculate the total background contamination for the three magnetic fields, putting together all the pieces needed for the final sensitivities to be calculated in the chapter ??.

## 6.1 Background Classification

### 6.1.1 Internal Backgrounds

Internal backgrounds are defined as backgrounds which originate within the confines of the source foil. The most substantial backgrounds found within the source foil are  $^{208}\text{Tl}$  and  $^{214}\text{Bi}$ , from the decay chains of  $^{232}\text{Th}$  and  $^{238}\text{U}$  respectively, as shown in figures 9 and 8.  $^{232}\text{Th}$  and  $^{238}\text{U}$  are two naturally occurring backgrounds found in small amounts within all materials. Source foils underwent processing in order to reduce the contamination of these naturally occurring radioisotopes, however a small amount of contamination still remains.

$^{208}\text{Tl}$  and  $^{214}\text{Bi}$  undergo beta decay generating pseudo double beta candidate events via a number of mechanisms that will be explained shortly. The mechanisms include;

- i Møller Scattering of the beta electron
- ii Compton scattering of a photon produced during beta decay (figures ?? and ??)
- iii Internal conversion of an excited nuclei

The final source of internal backgrounds is the two neutrino double beta decay of the same isotope. At higher energies, within the region of interest, two neutrino double beta decay is an irreducible background for  $0\nu\beta\beta$ . In the ROI,  $2\nu\beta\beta$  is indistinguishable from  $0\nu\beta\beta$  and can only be suppressed by maximising the precision of the  $2\nu\beta\beta$  energy spectrum and half-life estimates. The results from  $2\nu\beta\beta$  decays were shown in the previous chapter and will be reintroduced in order to complete the total background contamination subsequently.

### 6.1.2 Radon Backgrounds

Radon is a highly diffusive gas and readily enters the tracker volume via emanation from detector components or during construction.  $^{222}\text{Rn}$  has a lifetime of roughly 3.8 days, allowing plentiful time for the gas to diffuse into the detector and undergo alpha decay into  $^{218}\text{Po}$  (figure 8). The ejected alpha particle is able to remove electrons from the outer shell of the atom resulting in the positive ionisation of  $^{218}\text{Po}$ .  $^{218}\text{Po}$  ions are neutralised by the gas within the tracker chamber, eventually depositing  $^{214}\text{Pb}$  on the tracker wires and surface of the source foil.  $^{214}\text{Pb}$  decays into  $^{214}\text{Bi}$ , resulting in a large concentration of  $^{214}\text{Bi}$  being deposited.  $^{214}\text{Bi}$  undergoes beta decay, utilizing the same mechanisms as the internal backgrounds, to produce two electron events.

The most significant difference between the pseudo double beta events generated from internal and radon backgrounds is the surrounding environment. The increased density of the source foil amplifies the rate at which the decaying radioisotopes interact with the source foil. Whereas for the radon backgrounds, particularly on or inside of the tracker wires, the surrounding density is much lower, reducing the rate at which the beta decay progeny interact with matter. Additionally, the

volume of the tracker itself is filled with tracking gases <sup>\*\*\*ref from detector\*\*\*</sup> further reducing the interaction rate.

The SuperNEMO target activity for radon in the tracker volume is  $<0.15\text{mBq/m}^3$  and to achieve this target three additional procedures were selected to reduce and control the radon level within the detector volume;

- i Screening of materials to ensure only the highest radiopure materials were used
- ii Monitoring of the radon background levels
- iii Purification of the tracker gas

The most significant reduction in radon levels is achieved by flushing out the contaminated tracker gas with clean gas at a controlled rate. At a certain point, increasing the rate at which gas flows through the detector becomes detrimental to the performance of the detector and so a compromise between the performance and radon levels is met at a maximal flow rate of  $2\text{m}^3/\text{h}$  <sup>\*\*\*ref fang thesis\*\*\*</sup>. The table of radon activity, with and without the standard tracker flushing rate, is given below.

	Tracker Volume mBq
$^{222}\text{Rn}$ activity (no flushing)	$41.3 \pm 4.7$
$^{222}\text{Rn}$ with $1\text{m}^3/\text{h}$ flushing	$4.25 \pm 0.48$



Table 7: Activity of  $^{222}\text{Rn}$  inside the tracker volume with and without flushing

### 6.1.3 External Backgrounds

External backgrounds are defined as any non-radon backgrounds originating outside of the source foil. The majority of external backgrounds come about as a result of decays within the detector components, radioactive decays in the rocks surrounding the laboratory and neutron capture. External backgrounds materialise in a variety of decay channels including  $1eN\gamma$ , however it is possible for external backgrounds to bring about double beta like decays reconstructed from the source foil.

An array of mechanisms can result in the production of double beta candidate events from external backgrounds. Unlike internal backgrounds which mimic double beta decay via mostly low angle scattering, external backgrounds primarily generate pseudo double beta decays by way of photonic interactions with the dense source foil and other detector components. Pair production

and Compton scattering from external photons provide the two principal mechanisms by which external backgrounds contribute towards the double beta decay channel.

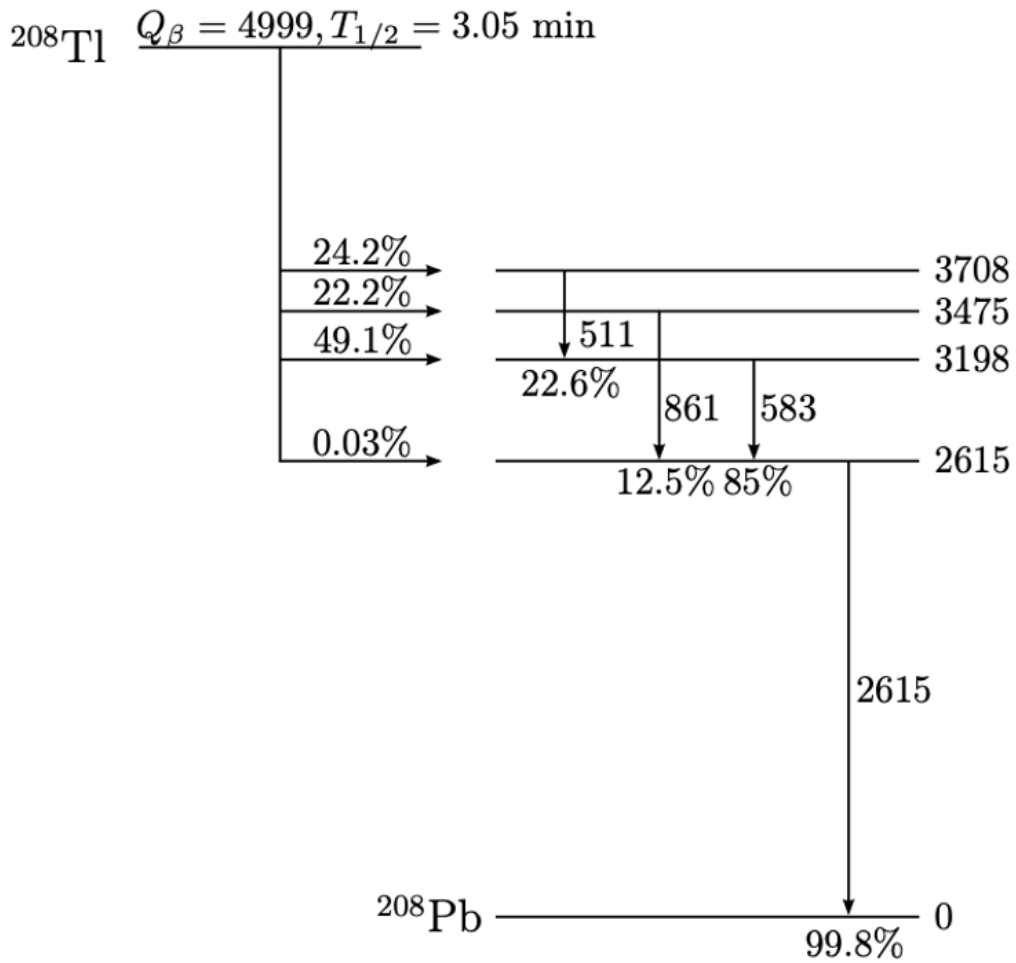


Figure 26: Simplified decay scheme for  $^{208}\text{Tl}$  undergoing beta decay into  $^{208}\text{Pb}$ , illustrating the most common transition lines, with the energies in keV.

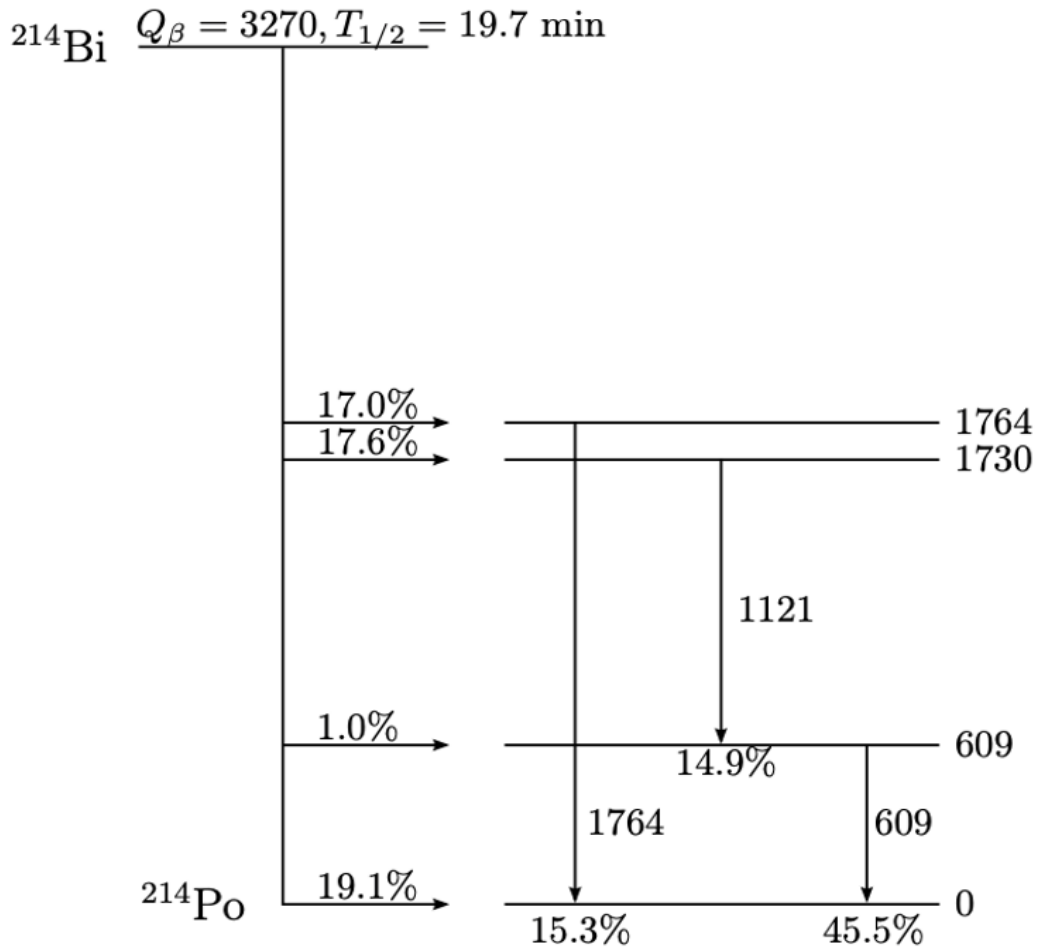


Figure 27: Simplified decay scheme for  $^{214}\text{Bi}$  undergoing beta decay into  $^{214}\text{Po}$ , illustrating the most common transition lines, with the energies in keV.



## 6.2 Background Mechanisms for Generating Double Beta Events

Many of the naturally occurring backgrounds for the SuperNEMO demonstrator provide a significant barrier to the sensitivity of the  $^{82}\text{Se}$  neutrinoless double beta decay search. Backgrounds generate pseudo double beta decays through a variety of different mechanisms as mentioned in section ???. The mechanisms for each background location are described in detail below.

### 6.2.1 Internal Backgrounds

The aforementioned sources of internal backgrounds, for  $^{82}\text{Se}$  neutrinoless double beta decay, include the naturally occurring radioisotopes  $^{208}\text{Tl}$  and  $^{214}\text{Bi}$ . Both isotopes undergo beta decay within the source foil and it is the interaction of the beta electron with the source foil that brings about events in the 2e channel as illustrated in figure ???. The first double beta generating mechanism is Møller scattering, which is a low angle electron-electron scattering where two electrons exchange a virtual photon transferring momentum between the two electrons. The beta electron emitted during the decay scatters an electron found within the dense source foil, resulting in the emission of two electrons from the source foil. As Møller scattering is a prompt interaction, the two electrons are emitted from the foil in parallel.

Compton scattering is the scattering of light by a charged particle, transferring momentum from the photon to the electron, ejecting the electron if the momentum transfer is sufficiently high. During beta decay, both  $^{208}\text{Tl}$  and  $^{214}\text{Bi}$  radiate photons of various energies (figures ?? and ??) which can initiate Compton scattering within the foil. The final mechanism for generating pseudo double beta events from internal backgrounds is internal conversion. Following the initial beta decay, the decaying isotope may reach an excited intermittent state during which it releases a photon for the purpose of de-excitation. Certain isotopes are able to de-excite via internal conversion, with an electron from one of the inner shells of the atom ejected from the unstable atom. The internal conversion electron can provide the second electron for the 2e topology although as a result of the de-excitation mechanism the electron emission is slower compared to prompt scattering interactions.

Although the density of the source foil increases the rate of electronic interactions, the foil also inhibits the charged particles from exiting, trapping them within the source foil or causing them to lose energy prior to emission. For this reason the source was processed into long thin sheets (foils) with the intention of minimising the energy loss for electrons prior to emission. \*\*\* ref thickness of sf from detector chapter \*\*\*

### 6.2.2 Radon Backgrounds

The mechanisms for generating double beta candidate events from radon backgrounds are similar to those observed for internal backgrounds (shown in figure ??), with scattering being the dominant process. Unlike internal backgrounds, radon induced backgrounds can be found on both the surface

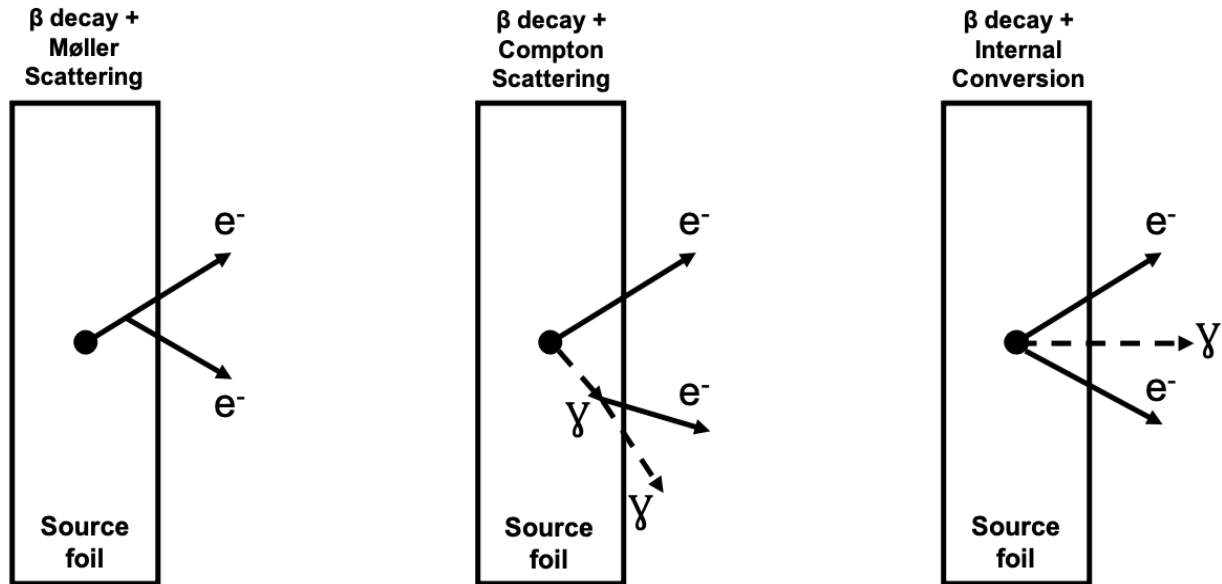


Figure 28: Internals interacting with foil



of the source foil and the tracker wires, resulting in vastly different environments. The high density of the source foil increases the cross section for both photonic and electronic interactions, increasing the rate at which internal backgrounds generate additional electrons. Whereas on the surface of the tracker wires, the lower density of the wires is less likely to generate extra electrons, resulting in fewer two electron topologies. Additionally, charged particles originating on wires in the outer layers of the tracker are unlikely to have their vertices extrapolated back to the source foil. Consequently, those events do not pass the two electron cut flow as a result of their reconstructed vertices not originating from the source.

### 6.2.3 External Backgrounds

For external backgrounds, the mechanisms for producing two electron topologies more often involve photonic interactions as opposed to the internal and radon backgrounds which mostly produce two electrons via beta decay plus low angle electronic scattering. Multi energy photons from external sources (figure ??) first interact with the source foil, producing an electron positron pair or a single Compton electron. The electron can then Møller scatter to eject a second electron from the source foil. Additionally, the incident photon can directly beget two electrons via double Compton scattering as the photon pass through the foil. Pair production (figure ??) requires a photon of energy greater than 1.022 MeV to interact with dense source material and produce an electron positron pair. The minimum energy threshold of 1.022 MeV, represents twice the rest mass energy of an electron, so it is impossible for lower energy photons to pair produce. Both  $^{208}\text{Tl}$  and  $^{214}\text{Bi}$  beta decays produce high energy ( $>1.022$  MeV) photons capable of pair producing as shown by the



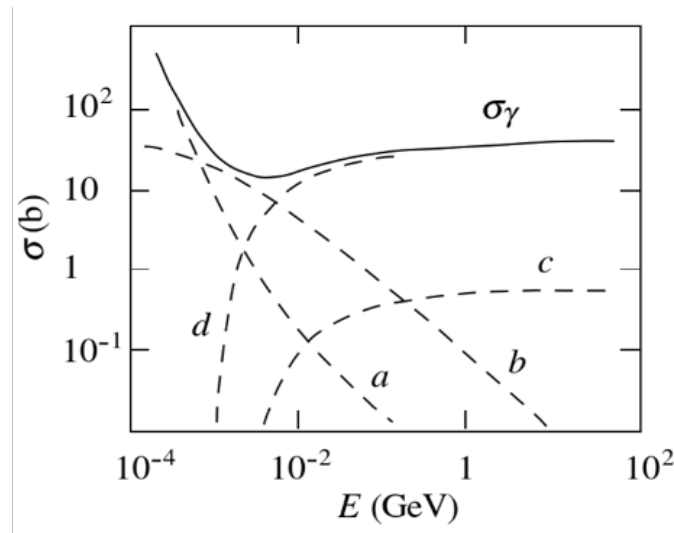


Figure 29: A

decay schemes in figures ?? and ?.  $^{208}\text{Tl}$  in particular, produces a 2.615 MeV photon at a rate of 99.8%. The electron positron pair emitted from the source foil, can be misconstrued as a two electron event if the positron is labelled as an electron. For no field this is particularly troublesome, as the absence of magnetic flux within the tracker volume results in straight tracks that cannot be differentiated by charge. At lower energies, the likelihood of Compton scattering and the photoelectric effect increases, although from the external photon flux in table ??, Compton scattering and pair production are the likely processes associated with externally induced double beta candidate events.

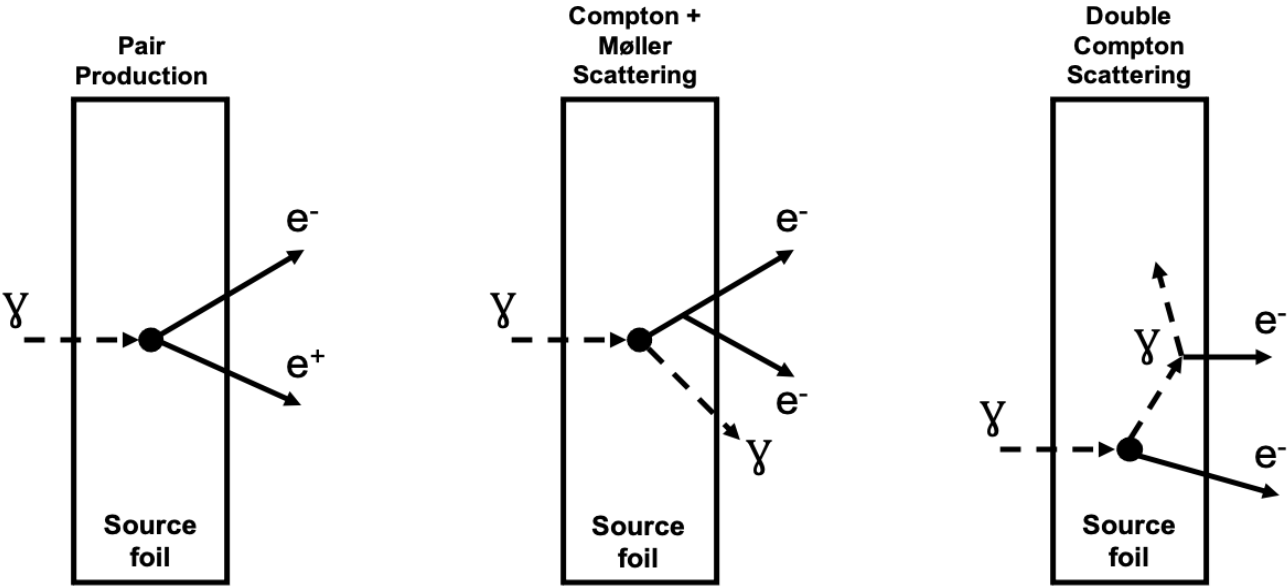


Figure 30: Internals interacting with foil



### 6.3 Background Activities

#### 6.3.1 Table of Activities

Isotope	Location	Activity mBq	No of Decays From Nominal Exposure
$2\nu\beta\beta$	Source Foil Bulk	X	X
$^{208}\text{Tl}$	Source Foil Bulk	0.55 *	43,000
$^{214}\text{Bi}$	Source Foil Bulk	4.94 *	389,500
$^{208}\text{Tl}$	Tracker Wire Bulk	$0.24 \pm 0.05$	18,900
$^{214}\text{Bi}$	Source Foil Surface	$0.33 \pm 0.04$	26,000
$^{214}\text{Bi}$	Tracker Wire Bulk	$0.49 \pm 0.10$	38,600
$^{214}\text{Bi}$	Tracker Wire Surface	$3.92 \pm 0.44$	309,000
$^{40}\text{K}$	8" Main Wall PMT Glass Bulb	$230 \pm 23$	18,133,200,000
$^{40}\text{K}$	5" Main Wall PMT Glass Bulb	$23 \pm 2.3$	1,813,320,000
$^{40}\text{K}$	X Wall PMT Glass Bulb	$37 \pm 3.7$	2,917,080,000
$^{40}\text{K}$	G Veto Wall PMT Glass Bulb	$19 \pm 1.9$	1,497,960,000
$^{208}\text{Tl}$	8" Main Wall PMT Glass Bulb	$41 \pm 4.1$	3,232,440,000
$^{208}\text{Tl}$	5" Main Wall PMT Glass Bulb	$1 \pm 0.1$	78,840,000
$^{208}\text{Tl}$	X Wall PMT Glass Bulb	$2 \pm 0.2$	157,680,000
$^{208}\text{Tl}$	G Veto Wall PMT Glass Bulb	$1 \pm 0.1$	78,840,000
$^{214}\text{Bi}$	8" Main Wall PMT Glass Bulb	$136 \pm 13.6$	10,722,240,000
$^{214}\text{Bi}$	5" Main Wall PMT Glass Bulb	$18 \pm 1.8$	1,419,120,000
$^{214}\text{Bi}$	X Wall PMT Glass Bulb	$30 \pm 3.0$	2,365,200,000
$^{214}\text{Bi}$	G Veto Wall PMT Glass Bulb	$15 \pm 1.5$	1,182,600,000

Table 8: Total activities for all backgrounds simulated with an internal, radon and external vertex. The activity (mBq) for each isotope is given alongside the expected exposure of 6.25 Kg over 2.5 years of running time. For internal  $^{208}\text{Tl}$  and  $^{214}\text{Bi}$  the activities are provided as an upper limit. For the external backgrounds the listed activities are given in Bq.

All external backgrounds have a total error of 10% \*\*\*ref Ferederic \*\*\*

The internal background activities within the source foil were measured throughout the volume of the detector and this contamination level was noted at multiple intervals. For  $^{214}\text{Bi}$ , the activity is given as a maximum limit from a BiPo measurement, with a 90% confidence. The target activity for  $^{214}\text{Bi}$  is  $10\mu\text{Bq/Kg}$  and  $2\mu\text{Bq/Kg}$  for  $^{208}\text{Tl}$ .

Radon in the tracker provides the contamination level for  $^{214}\text{Bi}$  on both the surface of the source foil as well as the tracker wires. The most accurate prediction states that approximately 7.8% of the radon contamination in the tracker deposits onto the surface of the tracker wires and the remaining 92.2% on the source foil surface. The division of activity is based on the width of the tracker-source air gap and the width of the tracker *\*\*ref docdb papaer\*\*\**. As mentioned earlier in the chapter, the radon activity is given as a function of the flushing rate, which is expected to be  $1\text{m}^3/\text{h}$ . The tracker wire bulk activity was directly measured alongside the anode wire bulk, however anode wire events were not simulated so the activity data is not included.

## 6.4 Background Simulations

### 6.4.1 Table of Simulations

Vertex Location	$^{40}\text{K}$	$^{208}\text{Tl}$	$^{214}\text{Bi}$	$2\nu\beta\beta$	Number of Simulations on Vertex
Source Foil Bulk		✓	✓	✓	$10^8$
Source Foil Surface		✓	✓		$10^8$
Tracker Wire Bulk		✓	✓		$10^8$
Tracker Wire Surface		✓	✓		$10^8$
8" Main Wall PMTs*	✓	✓	✓		$1.1 \times 10^{9\dagger}$
5" Main Wall PMTs	✓	✓	✓		$10^9$
X Wall PMTs	✓	✓	✓		$10^9$
G Veto Wall PMTs	✓	✓	✓		$10^9$

Table 9: Simulation vertex locations and the isotopes simulated at those locations

<sup>†</sup> For the external  $^{208}\text{Tl}$  simulations, 15 billion events were simulated for no field and 11 Billion events for the remaining two magnetic fields.

All simulations were generated using Falaise 4.0.0 detailed in chapter ???. Simulated events were then reconstructed using the official Falaise 4.0.0 reconstruction configuration. For each isotope simulated at a vertex location, the number of simulations were generated for all three magnetic field configurations. In addition, although the tracker wire bulk activity is not derived from the radon contamination in the tracker volume, backgrounds in the tracker wires closely resemble those observed with other radon backgrounds and so it is included within the radon backgrounds.

## 6.5 Background Results

### 6.5.1 Internal Backgrounds

Cut Descriptions	Magnetic Field Configuration		
	Uniform Field	No Field	Realistic Field
Only two calorimeter hits above 50keV, at least one >150keV	0.2387	0.2342	0.2349
Two tracker clusters with 3 or more cells	0.0311	0.0239	0.0253
Two reconstructed tracks	0.0309	0.0238	0.0251
Remove events with multiple hits to the same calorimeter	0.0134	0.0119	0.0122
Each track associated to a calorimeter	0.0017	0.0024	0.0022
Two vertices on the source foil	0.0016	0.0023	0.0022
Vertex $\Delta R < 1\text{cm}$ and $\Delta Z < 3\text{cm}$ (separation between vertices)	0.0008	0.0012	0.0011
Internal Probability >1% and External Probability <4%	0.0007	0.0010	0.0009
Delayed Alpha Hits (no hits allowed after 13 $\mu\text{s}$ )	0.0007	0.0010	0.0009
Remove Positrons (unavailable for no field)	0.0006	-	0.0006
Energy Cut (between 2.8 and 3.2 MeV)	$1907 \times 10^{-8}$	$2527 \times 10^{-8}$	$1637 \times 10^{-8}$
Number of Expected Events	0.82 $\pm 0.02$ (stat)	1.09 $\pm 0.02$ (stat)	0.69 $\pm 0.02$ (stat)

Table 10: Internal  $^{208}\text{Tl}$  cut flow for the three magnetic field configurations. Each row lists a short description of the cut as well as the concurrent detection efficiency.

As defined in section ??, internal backgrounds are those which originate from within the bulk of the source foil. For SuperNEMO, this includes the  $2\nu\beta\beta$  contribution discussed in the previous chapter as well as  $^{208}\text{Tl}$  and  $^{214}\text{Bi}$ . The number of internal simulations generated for each magnetic field is shown in table ?. Following simulation and reconstruction, the two electron cut flows and number of expected events are shown for  $^{208}\text{Tl}$  and  $^{214}\text{Bi}$  in tables ?? and ?? respectively.

From table ??, the final detection efficiency and consequently the magnetic field with the greatest

number of expected events is the no field scenario, followed by the uniform and realistic fields respectively. The most significant reason for this is the impact of the charge cut on reducing the uniform and realistic field, specifically the realistic field, whereas for no field the cut is not applied. The reduced field strength of the realistic field reduces the overall radius of curvature for realistic field events, decreasing the rate at which electron tracks are successfully reconstructed. Straighter charged particle tracks are more likely to be reconstructed as positrons increasing the number of events removed by the charge cut for the realistic field. Prior to the associated tracks cut, the uniform field has the greatest detection efficiency, as the increased track radius of curvature increases the number of reconstructed tracks. For  $0/2\nu\beta\beta$ , the increased rate of track fitting for the uniform field resulted in an increased number of events with three or more reconstructed tracks, as the two double beta electrons generated three electron tracks. However, for the single beta decaying backgrounds, the poor track fitting procedure increases the number of tracks from one to two and the photon provides a second calorimeter hit, resulting in an increased initial detection efficiency for the uniform field. After applying the remaining cuts however, the difference in detection efficiency between the uniform field and the other two fields is reduced as these events are identified and removed by other cuts.

Cut Descriptions	Magnetic Field Configuration		
	Uniform Field	No Field	Realistic Field
Only two calorimeter hits above 50keV, at least one >150keV	0.2375	0.2392	0.2389
Two tracker clusters with 3 or more cells	0.0315	0.0261	0.0271
Two reconstructed tracks	0.0303	0.0251	0.0260
Remove events with multiple hits to the same calorimeter	0.0157	0.0148	0.0150
Each track associated to a calorimeter	0.0032	0.0042	0.0040
Two vertices on the source foil	0.0028	0.0036	0.0035
Vertex $\Delta R < 1\text{cm}$ and $\Delta Z < 3\text{cm}$ (separation between vertices)	0.0013	0.0017	0.0017
Internal Probability >1% and External Probability <4%	0.0012	0.0016	0.0015
Delayed Alpha Hits (no hits allowed after 13 $\mu\text{s}$ )	0.0012	0.0016	0.0015
Remove Positrons (unavailable for no field)	0.0011	-	0.0010
Energy Cut (between 2.8 and 3.2 MeV)	$362 \times 10^{-8}$	$477 \times 10^{-8}$	$315 \times 10^{-8}$
Number of Expected Events	1.41 $\pm 0.07$ (stat)	1.86 $\pm 0.09$ (stat)	1.23 $\pm 0.92$ (stat)

Table 11: Internal  $^{214}\text{Bi}$  cut flow for the three magnetic field configurations. Each row lists a short description of the cut as well as the concurrent detection efficiency.

The detection efficiency of  $^{214}\text{Bi}$  is inferior to  $^{208}\text{Tl}$ , however, as a result of the greater  $^{214}\text{Bi}$  activity in the source foil (table ??), the number of expected backgrounds from  $^{214}\text{Bi}$  is higher. On average, the detection efficiency of internal  $^{208}\text{Tl}$  is around  $5\times$  greater compared to  $^{214}\text{Bi}$ , but after normalising to the activity, the number of expected events is roughly  $1.7\times$  greater for  $^{214}\text{Bi}$ . From figure ??, the reduced detection efficiency of  $^{214}\text{Bi}$  can be explained from tail of the energy spectrum, which falls to zero within the region of interest, akin to  $2\nu\beta\beta$ . For internal  $^{208}\text{Tl}$ , the energy spectrum extends well beyond the  $^{82}\text{Se}$  ROI, increasing the total number of two electron events found within the region.

The results for  $2\nu\beta\beta$  were discussed in chapter ?? which completes the internal background



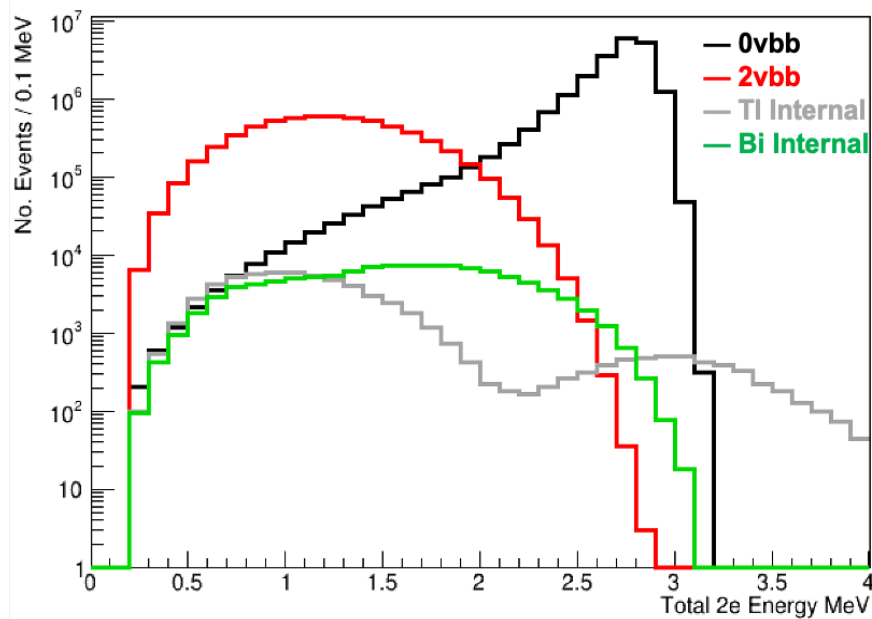


Figure 31: InternalSpectrum

contributions. The number of expected events from  $2\nu\beta\beta$  is shown in table ??, alongside the results from internal  $^{208}\text{Tl}$  and  $^{214}\text{Bi}$ . The total internal background count for each magnetic field configuration is also provided.

Internal Background	Number of Expected Events		
	Uniform Field	No Field	Realistic Field
$2\nu\beta\beta$	$0.15 \pm 0.09$ (stat)	$0.10 \pm 0.07$ (stat)	$0.05 \pm 0.05$ (stat)
$^{208}\text{Tl}$	$0.82 \pm 0.02$ (stat)	$1.09 \pm 0.02$ (stat)	$0.69 \pm 0.02$ (stat)
$^{214}\text{Bi}$	$1.41 \pm 0.07$ (stat)	$1.86 \pm 0.09$ (stat)	$1.23 \pm 0.92$ (stat)
Total	$2.38 \pm$ (stat)	$3.05 \pm$ (stat)	$1.97 \pm$ (stat)

Table 12: Number of expected events for all internal backgrounds for the three magnetic field configurations. The activities used to calculate the number of expected events are upper limits and so no systematic error is given.

Of the three backgrounds,  $^{214}\text{Bi}$  has the greatest number of expected events followed by  $^{208}\text{Tl}$  and  $2\nu\beta\beta$ . As a result of the low  $2\nu\beta\beta$  detection efficiency, the number of expected events is much lower compared to the other internal backgrounds whilst also having a high statistic uncertainty. Overall, the internal background contamination is highest for no field, followed by the uniform field and realistic field respectively.

## 6.5.2 Radon Backgrounds

Isotope	Location	Detection Efficiency ( $\times 10^{-8}$ ) & Number of Expected Events		
		Uniform Field	No Field	Realistic Field
$^{208}\text{Tl}$	Tracker Wire Bulk	30	53	34
		$0.006 \pm 0.001$ (stat) $\pm 0.002$ (syst)	$0.010 \pm 0.001$ (stat) $\pm 0.004$ (syst)	$0.006 \pm 0.001$ (stat) $\pm 0.002$ (syst)
$^{214}\text{Bi}$	Source Foil Surface	314	373	247
		$0.08 \pm 0.004$ (stat) $\pm 0.009$ (syst)	$0.10 \pm 0.005$ (stat) $\pm 0.011$ (syst)	$0.06 \pm 0.004$ (stat) $\pm 0.007$ (syst)
$^{214}\text{Bi}$	Tracker Wire Bulk	9	9	6
		$0.003 \pm 0.001$ (stat) $\pm 0.001$ (syst)	$0.003 \pm 0.001$ (stat) $\pm 0.001$ (syst)	$0.002 \pm 0.001$ (stat) $\pm 0.001$ (syst)
$^{214}\text{Bi}$	Tracker Wire Surface	6	9	6
		$0.019 \pm 0.008$ (stat) $\pm 0.002$ (syst)	$0.028 \pm 0.009$ (stat) $\pm 0.003$ (syst)	$0.019 \pm 0.008$ (stat) $\pm 0.002$ (syst)

Table 13: Detection efficiency of all radon simulations for the three magnetic field configurations.

Radon backgrounds contribute significantly fewer expected events to the  $^{82}\text{Se}$  ROI compared to those from the internal sources. For  $^{208}\text{Tl}$  in the bulk of the tracker wires, both the detection efficiency and activity are lower than the corresponding internal background, resulting in the  $^{208}\text{Tl}$  radon contribution being roughly 1% of the total internal  $^{208}\text{Tl}$  expected events.

For  $^{214}\text{Bi}$ , there are three sources of radon backgrounds, including the surface of the source foil,

tracker wire bulk and tracker wire surface. The combined contribution from the three radon sources is dwarfed by internal  $^{214}\text{Bi}$ , accounting for only 7% of the internal contribution. Primarily this is a consequence of the lower  $^{214}\text{Bi}$  activity on the surface of the source foil and the low detection efficiency of the tracker wire simulations. The detection efficiency of  $^{214}\text{Bi}$  on the source foil surface is similar to that observed with  $^{214}\text{Bi}$  inside of the source foil however, as the activity is an order of magnitude lower the number of expected events is similarly reduced. The detection efficiencies for  $^{214}\text{Bi}$  on the surface and within the bulk of the tracker wires are significantly lower than that seen for  $^{214}\text{Bi}$  on the source foil surface because the event vertices are less likely to be reconstructed back to the foil.

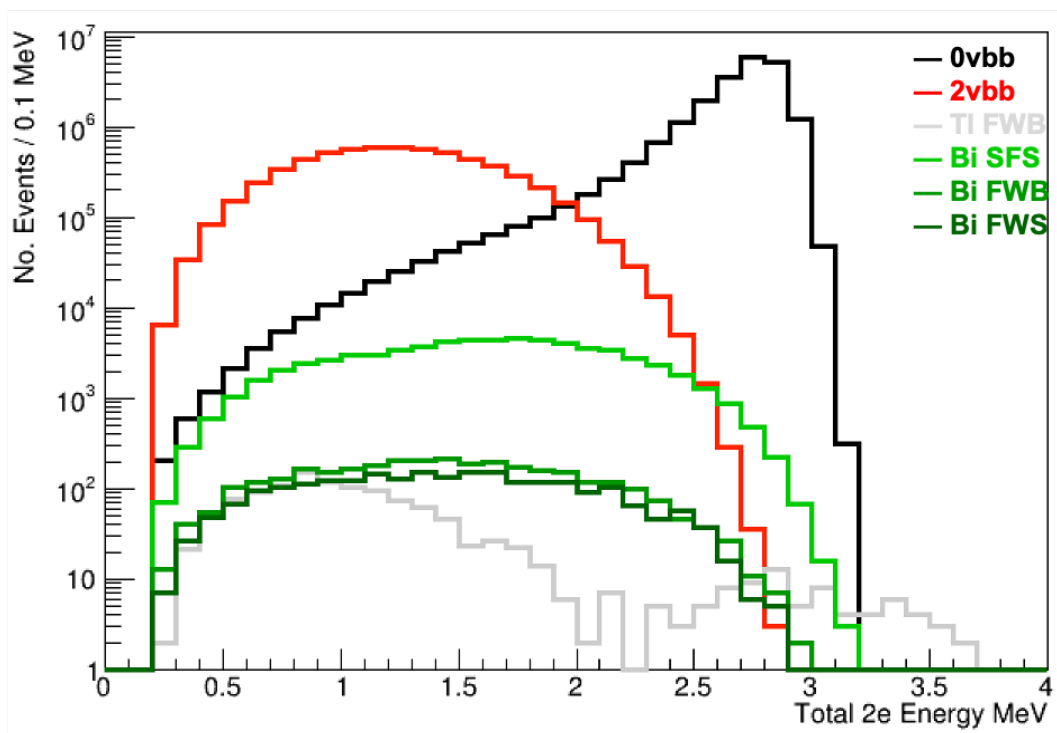


Figure 32: 0

Like internal  $^{214}\text{Bi}$ , the radon  $^{214}\text{Bi}$  energy spectra curtail within the  $^{82}\text{Se}$  ROI, reducing the detection efficiency compared to  $^{208}\text{Tl}$ . Additionally, the energy profile for  $^{214}\text{Bi}$  on the surface of the source foil is extremely similar to the internal  $^{214}\text{Bi}$  spectra.

### 6.5.3 External Backgrounds

Isotope	Location	Detection Efficiency & Number of Expected Events		
		Uniform Field	No Field	Realistic Field
$^{208}\text{Tl}$	8" Main Wall PMTs	$\frac{2^*}{1.1 \times 10^{10}}$	$\frac{110^\dagger}{1.5 \times 10^{10}}$	$\frac{10^*}{1.1 \times 10^{10}}$
		$0.58 \pm 0.41$ (stat) $\pm 0.06$ (syst)	$23.5 \pm 2.24$ (stat) $\pm 2.35$ (syst)	$2.91 \pm 0.92$ (stat) $\pm 0.29$ (syst)

Table 14: Number of simulations and expected events for external  $^{208}\text{Tl}$  on the 8" Main wall PMTs for the three magnetic field configurations.

From  $^\dagger 15$  billion and  $*11$  billion simulated events.

From the external PMTs, the sole background contribution to the  $^{82}\text{ROI}$  came from  $^{208}\text{Tl}$  on the 8" Main wall PMTs. No Monte Carlo simulated events were found in the ROI for any of the other isotopes simulated in all of the external locations. As a result of the non-zero contribution from external  $^{208}\text{Tl}$  on the 8" Main wall PMTs, an increased number of events were simulated (from the original  $10^9$ ) in order to reduce the statistical uncertainty on the simulated data. For no field, including the additional secondary particle simulations, a total of 15 billion events were simulated, whereas for the uniform and realistic fields, 11 billion decays were simulated, with no secondary particle simulations.

Following simulation and normalization to both the exposure as well as the number of simulated events, the cut flow detection efficiency and total number of expected events for  $^{208}\text{Tl}$  on the 8" Main wall PMT glass bulb is shown in table ???. The number of expected events of 23.5 for no field represents almost 90% of the total backgrounds for the no field scenario. Although the detection efficiency is much lower for external  $^{208}\text{Tl}$ , the much greater activity from external sources (table ???) results in an increased number of expected backgrounds compared to other background sources. Similarly, for the realistic field, external  $^{208}\text{Tl}$  is the largest background however it only represents approximately 60% of the total activity. For the uniform field external  $^{208}\text{Tl}$  is the third largest background contribution behind internal  $^{208}\text{Tl}$  and internal  $^{214}\text{Bi}$ . The extremely large contribution from external  $^{208}\text{Tl}$ , particularly for no field and the realistic field requires further multi variate analysis in order to create additional, targeted cuts for reducing this particular background. In the following chapter, the underlying mechanism producing the background will be discussed and used to rationalize the extra cuts and finally the impact of these cuts will be exhibited.

The energy spectra for the four simulated sources of external  $^{208}\text{Tl}$  are shown in figure ?? alongside the energy spectra for 0 and  $2\nu\beta\beta$ . The remaining three external  $^{208}\text{Tl}$  vertex locations

lead to the generation of double beta candidate events however no such events has energy greater than 2.5 MeV.

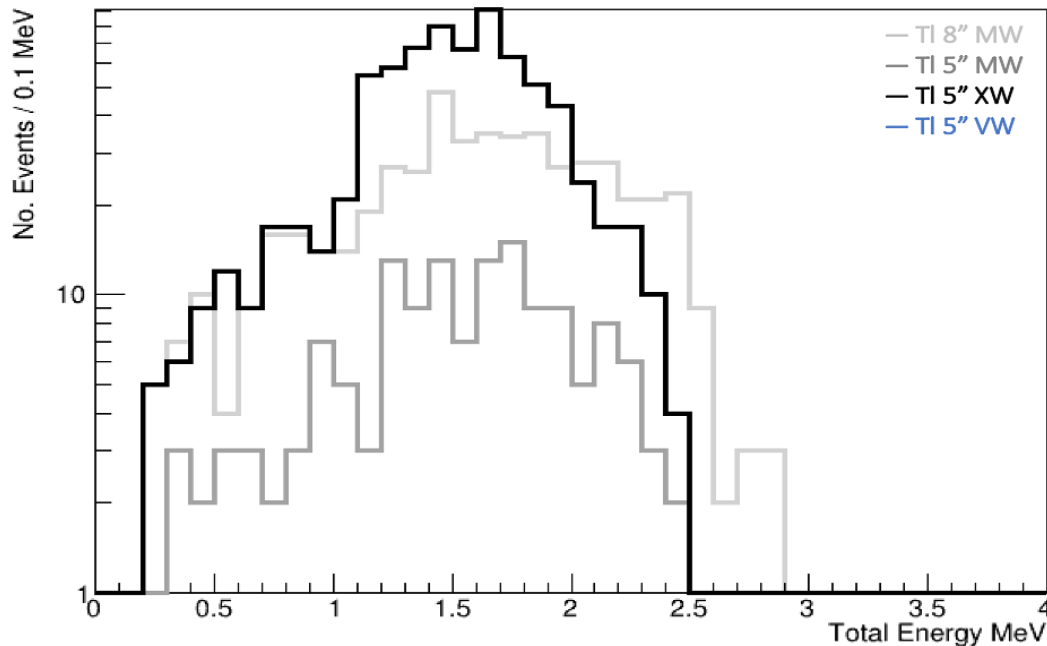


Figure 33: Energy spectra of all external  $^{208}\text{Tl}$  double beta candidate events.

There were no background contributions from any of the isotopes simulated on the 8" Main Wall, 5" Main wall, X wall and Veto wall PMT glass bulbs. Backgrounds from the two rows of 5" Main wall PMTs, located at the top and bottom of the Main walls, are encumbered by their location, reducing the number of external backgrounds reaching the source foil. A similar but more severe impact is observed for the G Veto simulations with no double beta candidate events of any energy being generated. Although the X wall events are less suppressed by their location within the detector, the double beta candidate events have energies outside the region of interest.

The energy spectra of the three isotopes simulated on the 8" Main wall PMTs is shown in figure ??, with only the  $^{208}\text{Tl}$  tail surpassing 2.8 MeV. The lower energy decays of  $^{40}\text{K}$  and  $^{214}\text{Bi}$  results in the potential double beta candidate events to be removed by the 2.8 - 3.2 MeV energy cut. Additionally, the low energy spectra shown in figure ?? indicate no double beta candidate events would be found from simulating on the X and G Veto walls and so no events were simulated. The Main wall represents the most probable external vertex location for inducing two electron events and so it is not expected for either external  $^{40}\text{K}$  or  $^{214}\text{Bi}$  to contribute to the  $^{82}\text{Se}$  ROI.

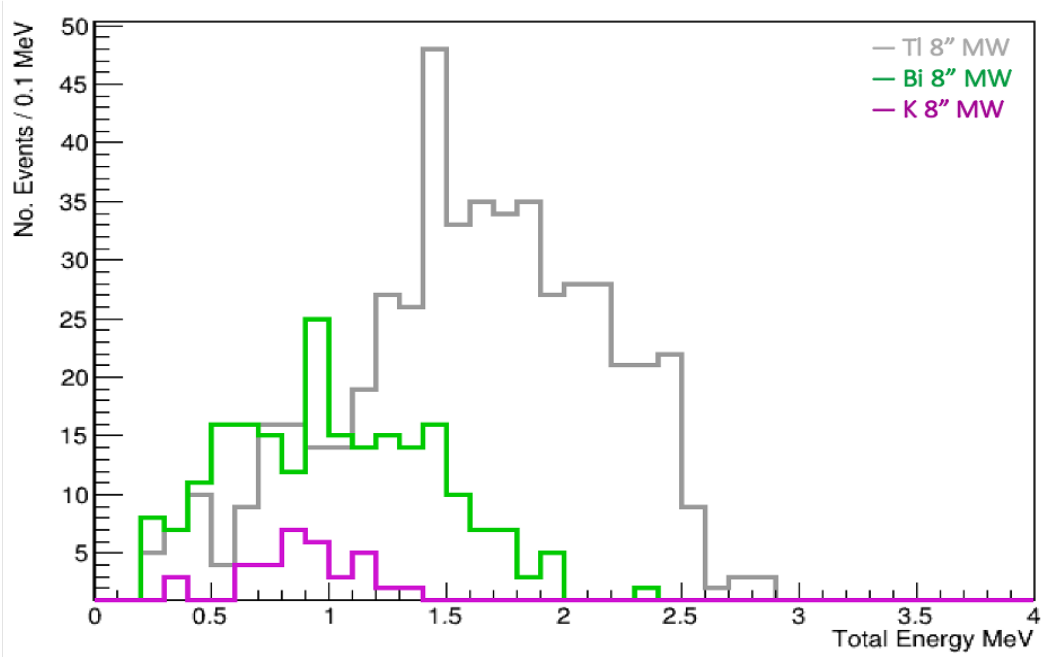


Figure 34: Energy spectra of all 8" Main wall backgrounds for no field. 1 billion

#### 6.5.4 Total Background Contributions

Background	Number of Expected Events/ $10^8$ MC Simulations		
	Uniform Field	No Field	Realistic Field
Internal $^{208}\text{Tl}$	0.82	1.09	0.69
Internal $^{214}\text{Bi}$	1.41	1.86	1.23
Radon $^{208}\text{Tl}$	0.006	0.010	0.006
Radon $^{214}\text{Bi}$	0.104	0.128	0.086
*External $^{208}\text{Tl}$ 8" Main Wall PMTs	0.58	23.5	2.91
Total Number of Expected Events	2.92	26.5	4.92

Table 15: Number of expected events of the different background isotopes and their locations within the detector. The total number of expected backgrounds for all three magnetic fields is also provided.

Table ?? gives the total number of expected events for each isotope that contributes a non-zero amount to the  $^{82}\text{Se}$  region of interest. Of the three magnetic field configurations, no field has the greatest number of expected backgrounds, roughly 5x greater than the realistic field and close to 9x the uniform field. The discrepancy between the three fields is largely a result of the contribution from external  $^{208}\text{Tl}$  on the 8" Main Wall PMTs which contributes significantly more for no field. Overall, the number of expected events from each background is highest for no field, largely as a result of the increased rate of associated calorimeter hits for charged particle tracks but also the inability to cut particles based on their charge.

For the realistic field, the number of expected events from each background source is the lowest amongst the three fields except for external  $^{208}\text{Tl}$ , which increases the total backgrounds for the realistic field to be greater than the uniform field. From the cut flows in tables ?? and ??, the detection efficiency of double beta candidate events is greater for the realistic field until the charge and energy cuts are applied at which the lower magnetic field strength of the realistic field reduces the efficiency at which electrons charges are accurately reconstructed therefore reducing the number of possible double beta candidate events.

Additionally, the increased contribution from external  $^{208}\text{Tl}$  is a result of the incredibly high activity of the external backgrounds as the detection efficiencies of the external backgrounds are generally much lower compared to the internal or radon simulations. By identifying the mechanism behind the external  $^{208}\text{Tl}$  it may be possible to target and remove the small number of reconstructed

---

events that result in the large background contribution. At the same time it may also be possible to reduce the other backgrounds, in particular, internal  $^{208}\text{Tl}$  and  $^{214}\text{Bi}$ , however it should not come at the cost of significantly reducing the signal detection efficiencies shown in the previous chapter, in order to maintain a high sensitivity to  $^{82}\text{Se}$  neutrinoless double beta decay.



# Chapter 7

## Sensitivity And Optimization

From the previous chapter it was shown that the major background contributions came from internal  $^{208}\text{Tl}$  /  $^{214}\text{Bi}$  as well as external  $^{208}\text{Tl}$  on the 8" Main wall PMTs. Of the three magnetic field configurations being investigated, the no field scenario had the highest detection efficiency for reconstructing two electron events from all backgrounds. Consequently, the no field scenario had the greatest number of expected backgrounds, followed by the realistic and uniform field (table ??). Furthermore, the discrepancy in the number of expected backgrounds between no field and the other two magnetic fields was found to be extremely stark, with the number of expected events for no field being 5 and 9 times greater than the realistic and uniform field respectively. The primary reason for this was the greater detection efficiency of external  $^{208}\text{Tl}$  with no magnetic field. Additionally, in chapter ??, the detection efficiency of  $0\nu\beta\beta$  was shown to be highest for no field, followed by the uniform and realistic field. However, the difference in detection efficiency of  $0\nu\beta\beta$  across the three magnetic fields was much lower compared to the expected backgrounds.

In order to measure the performance of three magnetic field configurations, the sensitivity to  $^{82}\text{Se}$  neutrinoless double beta decay is calculated for each magnetic field and the magnetic field with the highest sensitivity is likely to provide the best performance during the detectors operational lifetime. The sensitivity is dependant upon multiple factors, including the  $0\nu\beta\beta$  detection efficiency and number of expected backgrounds discussed in the previous chapters. To maximize sensitivity, the  $0\nu\beta\beta$  detection efficiency should be as large as possible whilst simultaneously suppressing the background count. During this chapter, additional optimization cuts will be rationalised using the underlying mechanism generating the 2e events from external  $^{208}\text{Tl}$ . The impact of the additional optimization cuts on both the background contamination and signal efficiency will be presented. Subsequently, the current 2.8 - 3.2 MeV ROI will be optimised to minimise background and maximise the signal and finally the sensitivities of the three magnetic field scenarios will be approximated, using both Gaussian and Poissonian methods, with a view to determine which of the three magnetic field scenarios provides the greatest  $0\nu\beta\beta$  sensitivity.

### 7.0.1 External Background Mechanism for DBD Candidates

The initial beta decay of  $^{208}\text{Tl}$  on the PMT glass bulbs results in the emission of an electron, as well as a number of gammas dictated by the decay scheme in figure ???. However, after generating additional simulations with true secondary particle information, the two reconstructed electron tracks were brought about by a single secondary electron emitted from the initial PMT. The single electron generates two reconstructed tracks by propagating from the primary PMT, to the source foil and backscattering off the foil before finally coming to rest in a second calorimeter close to the initial decay. This results in two reconstructed charged particles that appear to have a shared vertex on the foil.

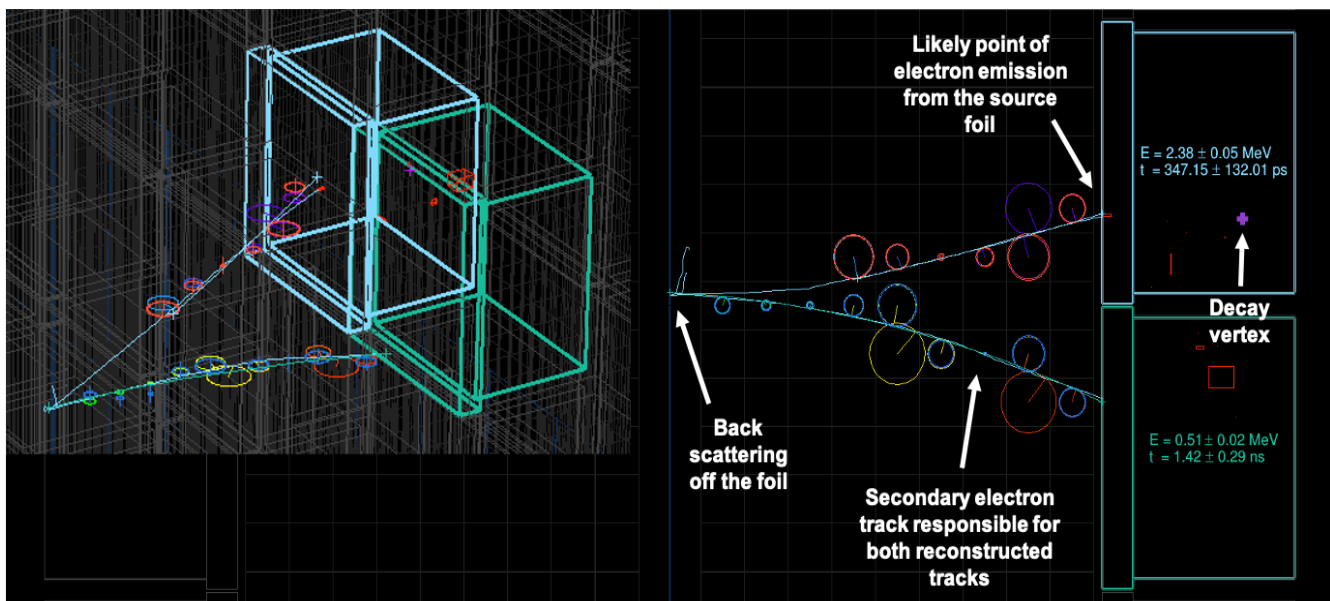


Figure 35: Event display illustrating the mechanism resulting in external  $^{208}\text{Tl}$  producing a double beta candidate event.

The mechanism resulting in the emission of the secondary electron is unclear as the interactions inside of the optical modules are often very complicated, although the electron is most likely to be emitted via Compton or low energy electron scattering. The emitted secondary electron is of low energy, but additional energy is provided by the primary photons, including the 2.6 MeV photon produced in almost all  $^{208}\text{Tl}$  decays as shown in figure ???. This additional energy is registered by either the initial or adjacent PMT, raising the total energy of the event into the  $^{82}\text{Se}$  ROI. Falaise only registers the timing of the first calorimeter hit, hence the initial primary decay inside the PMT provides the timing information for both calorimeters if energy is deposited during the initial decay. Therefore the separation in timing is determined by the time taken for energy to be deposited in the neighbouring calorimeter and not the time taken for the secondary electron to backscatter off the foil, allowing the events to pass the time of flight cuts (internal and external probability). This

combination of factors allows for external  $^{208}\text{Tl}$  events to pass all of the current cuts and contribute significantly towards the total background count, particularly for no field.

Therefore, to successfully generate a double beta candidate event from external  $^{208}\text{Tl}$ , the incident secondary electron must interact head on with the source foil so that the electron returns to the locale of the initial decay. For simulations on the X and G Veto wall PMTs, it is impossible for secondary electrons to strike the foil at an angle that can backscatter towards the initial vertex location because the X and G Veto walls do not face the exposed side of the source foil. Moreover, as the strength of the magnetic field increases, the number of double beta decay candidates generated from external  $^{208}\text{Tl}$  decays decreases as the probability of an electron backscattering off the foil and striking an adjacent calorimeter diminishes.

## 7.1 Background Optimization

As a result of the excessive number of expected events for external  $^{208}\text{Tl}$  on the 8" Main wall PMTs, further cuts are necessary for reducing the prevalence of the background. From chapter ??, external  $^{208}\text{Tl}$  was shown to represent over 90% of the total background for the no field scenario and increased the total background for no field to over 5 and 9 times the background count observed for the realistic and uniform field respectively. To explicitly target the external  $^{208}\text{Tl}$  background, three additional cuts were identified and include:

- i Setting a minimum opening angle for the 2e topology
- ii Removing events with adjacent calorimeter hits
- iii Removing events in specific energies regions based on the decay scheme of  $^{208}\text{Tl}$

### 7.1.1 Minimum Opening Angle

As previously mentioned, pseudo double beta decays from background simulations, often results in 2e events with low opening angles. As shown in figure ??,  $0\nu\beta\beta$  follows a  $1 - \cos\theta$  angular distribution, with the majority of events found at large angles. However, cutting on smaller angles does still remove a significant number of signal events so it pertinent to measure if there is an overall improvement in sensitivity when cutting out double beta candidate events with small angles. From the angular distributions shown in figures ?? and ?? the proportion of events at lower angles ( $\cos\theta \approx 1$ ) is greater for the backgrounds, particularly, external  $^{208}\text{Tl}$ . Cutting out events at low angles should disproportionately target these backgrounds whilst maintaining a high  $0\nu\beta\beta$  detection efficiency. The angular distributions for internal backgrounds is less skewed to lower angles (figure ??), relative to the radon and external contaminations, therefore they are not expected to have as many events removed at low angles.

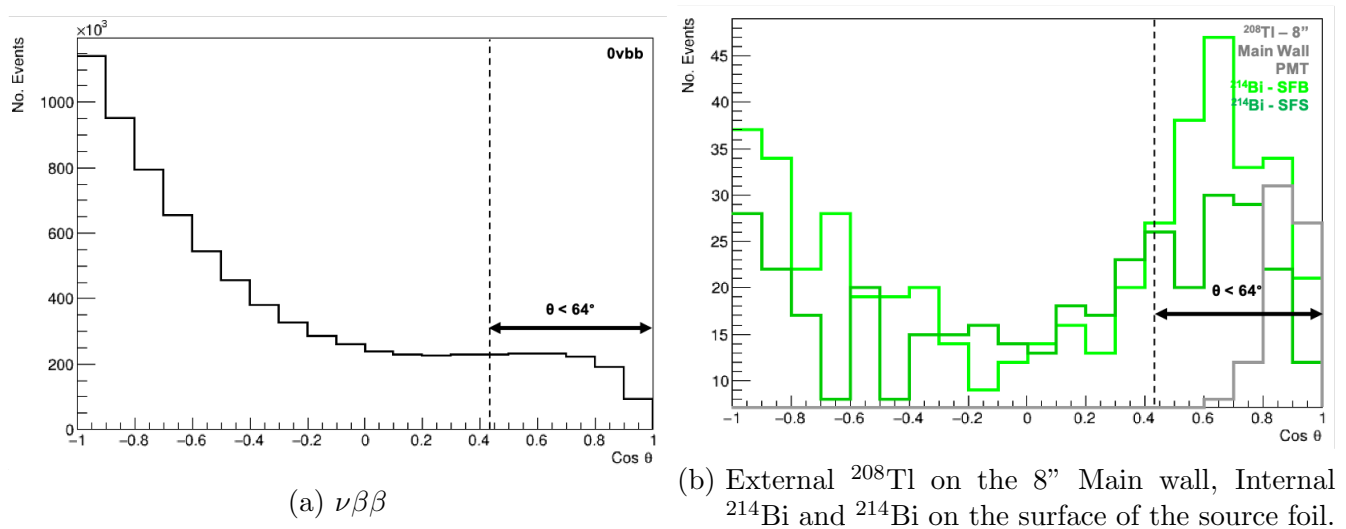


Figure 36: No field angular distributions for signal and backgrounds, including the theoretical maximum angle for two charged particles striking adjacent calorimeters (dashed line).

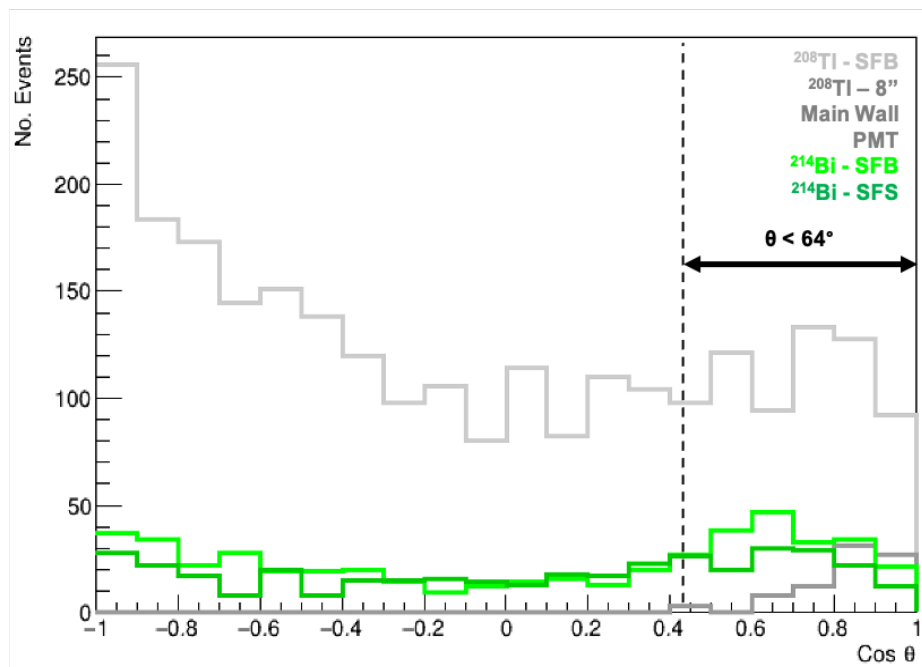


Figure 37:  $\text{Cos } \theta$  distribution for different backgrounds, including the theoretical maximum angle for two charged particles striking adjacent calorimeters (dashed line).

### 7.1.2 Minimum Angle Optimization

Prior to applying the minimum angle cut, the optimum angle was first determined by investigating a number of different minimum angles, ranging from  $0^\circ$  (no minimum angle), to  $100^\circ$ , increasing

in increments of  $10^\circ$ . The signal detection efficiency and background contributions was measured for each of the minimum opening angles and a simple Gaussian approximation (displayed in section ??) was used to plot figure ?? below.

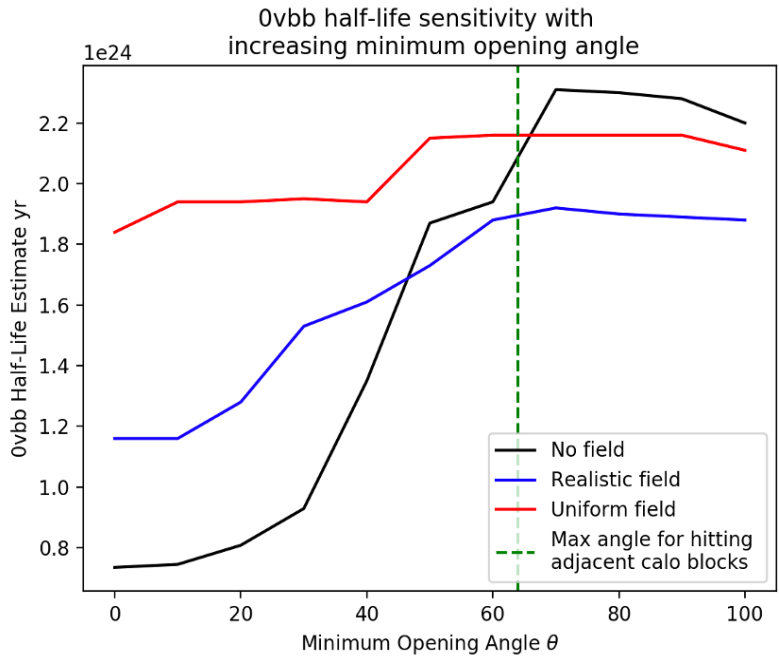


Figure 38: Minimum opening angle vs sensitivity for the three magnetic field configurations. Maximal sensitivity is achieved around a minimum angle of  $70^\circ$ .

For all three magnetic fields, the sensitivity to  $^{82}\text{Se } 0\nu\beta\beta$  was shown to increase as the minimum opening angle increased, until  $70^\circ$ , following which the sensitivity plateaus. Angles above  $100^\circ$  were not considered as they would begin to remove excessive amounts of signal events (figure ??). The increase in sensitivity with increasing minimum opening angle was most abrupt for no field as the excessive number of low angle external  $^{208}\text{Tl}$  are removed, unlike the uniform and realistic fields which have much lower contributions from external  $^{208}\text{Tl}$ . At higher angles ( $>50^\circ$ ), the cut removes a greater number of internal backgrounds but also begins to remove a significant number of signal events resulting in the sensitivity plateauing.

For no field and the realistic field, as the minimum angle increases, the internal backgrounds become the dominant background as the external contribution is removed. At around  $70^\circ$ , the number of external backgrounds for all three magnetic fields is reduced to zero, corresponding to the peak sensitivities. From this we can assert that the optimum minimum opening angle cut should be between  $65^\circ$  and  $75^\circ$  and is the consensus for all three magnetic fields. At higher angles, the reduction in signal limits any improvement in sensitivity and at angles below  $65^\circ$ , the external backgrounds, particularly for no field and the realistic field, significantly degrade the sensitivity.

### 7.1.3 No Adjacent Calorimeter Hits

Double beta candidate events generated by external  $^{208}\text{Tl}$  are primarily low angle events, often resulting in events with hits in adjacent calorimeters. Adjacent calorimeter events are described as events with a second calorimeter hit, occurring in any of the horizontally, vertically or diagonally neighbouring calorimeters, to the first hit. A visual description of adjacent calorimeter hits is show in figure ?? below. The dashed line in figures ??-??, around  $64^\circ$ , represents the maximum theoretical angle for events with adjacent calorimeter hits, which is calculated using the angle between two maximally separated and diagonally adjacent calorimeter hits.

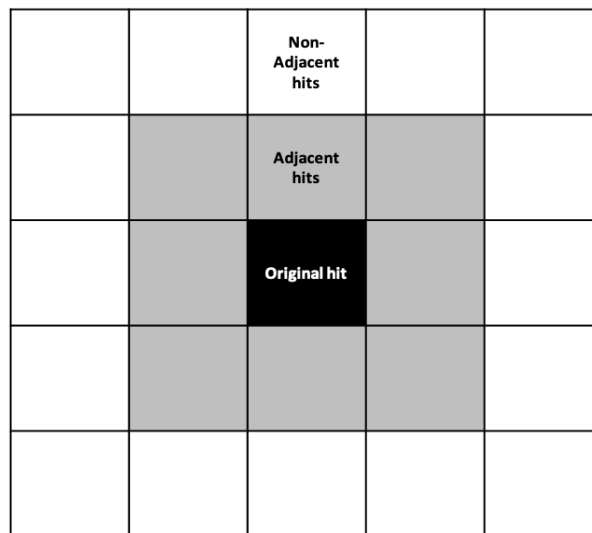


Figure 39: Illustration of the adjacent calorimeter hit definition. Any hit within a block horizontally, vertically or diagonally adjacent to the original hit is labelled an adjacent calorimeter hit.

Removing events with hits in adjacent calorimeters provides an alternate approach to the minimum opening angle cut, in the hopes of removing the external backgrounds without significantly reducing the signal detection efficiency. Evidently, there will be a large overlap between the low angle and adjacent calorimeter events, although, the orientation of the reconstructed electrons emitted from the foil can result in low angle events hitting non-adjacent calorimeters. By explicitly targeting the adjacent calorimeter hits commonplace with external  $^{208}\text{Tl}$   $2e$  events, the number of backgrounds may be reduced without reducing the signal efficiency as much as the angle cut. Preserving the detection efficiency whilst reducing the background count is guaranteed to result in an increase sensitivity.

The adjacent calorimeter cut had to be uniquely implemented into Sensitivity Module using multiple Falaise functions that extracted data from the various data banks. To determine whether an event consists of two adjacent calorimeter hits, the unique geometry identifier (GID) (found in the Falaise data banks ??) for the first calorimeter is extracted by the GetGID function. The

unique GID is then inputted into the GetNeighbourGIDs function, which provided the GIDs for all neighbouring calorimeters. If the second calorimeter hit GID matches one of the neighbouring GIDs, the event is designated as having an adjacent calorimeter hit.

#### 7.1.4 Tl Energy Split

$^{208}\text{Tl}$  beta decay occurs through the excited state of  $^{208}\text{Pb}$  with the emission of a 2.615 MeV photon (figure ??). As a result, there is an increased energy separation between the higher and lower energy calorimeter hits compared to  $0\nu\beta\beta$ , therefore, by exploiting this energy separation it may be possible to explicitly target the problematic external  $^{208}\text{Tl}$  background.

From [?], multiple exclusionary energy regions were selected for targeting  $^{208}\text{Tl}$  backgrounds. Upper and lower regions were identified, for the higher and lower electron energies respectively. For the purpose of this optimization process, the exclusion region for the lower energy electron was set as 0.2-0.9 MeV and for the higher energy electron, the exclusion region included electrons with energy between 2.3-2.59 MeV. Events with both the higher and lower energy electrons outside of these regions, pass the cut and contribute towards the total background count. From previous investigations for NEMO-2 and NEMO-3, this selective cut was shown not to result in an improved sensitivity for  $^{100}\text{Mo}$  neutrinoless double beta decay. The decay energy for  $^{82}\text{Se}$  is similar to  $^{100}\text{Mo}$  (table 2) and so the exclusionary energy regions are applicable for SuperNEMO.

### 7.1.5 Optimization Results

Similar to the minimum angle cut, the adjacent calorimeter hit cut was retrospectively applied to both signal and background to determine the influence of the cut on the sensitivity to neutrinoless double beta decay, for the three magnetic field configurations. Unlike the minimum angle cut, cut optimization was not required.

	$0\nu\beta\beta$ Detection Efficiency		
	Uniform Field	No Field	Realistic Field
Prior to optimization	0.0653	0.0790	0.0537
Angle $>70^\circ$	0.0551	0.0666	0.0451
No adjacent hits	0.0619	0.0754	0.0510
Tl energy separation	-	0.0470	-

Table 16:  $0\nu\beta\beta$  detection efficiency before and after the different optimization cuts.

Table ?? provides the detection efficiency of  $0\nu\beta\beta$  before and after the different optimization cuts. The highest detection efficiency, for all three magnetic field configurations, is with no additional cut and the lowest detection efficiency is observed with the  $^{208}\text{Tl}$  separation. Additionally, the  $^{208}\text{Tl}$  separation cut produces the highest number of expected backgrounds (table ??) whilst the minimum angle and adjacent calorimeter cuts successfully remove the external  $^{208}\text{Tl}$  events, significantly reducing the total background count.

Total Background Expected Events	Magnetic Field		
	Uniform Field	No Field	Realistic Field
Prior to optimization	2.92	28.4	4.92
Minimum Angle $70^\circ$	1.53	1.89	1.31
No adjacent hits	1.98	3.54	1.78
Tl energy separation	-	12	-

Table 17: Number of expected backgrounds before and after the different optimization cuts.



Although the detection efficiency of  $0\nu\beta\beta$  was reduced by the angle cut further than the adjacent calorimeter cut, the angle cut more successfully reduced the number of internal backgrounds. As show in figure ??, there are a significant number of internal backgrounds at smaller angles and so the minimum angle cut is able to remove a greater number of backgrounds, whether internal, radon or external. Unlike the minimum angle cut, the adjacent calorimeter cut is more targeted towards removing external  $^{208}\text{Tl}$ , which generates double beta candidate events with adjacent hits.

The minimum angle cut brought about the highest sensitivity for all three magnetic fields. Most notably, the increase in sensitivity for no field, as a result of the reduced background, makes it the magnetic field with the highest sensitivity. Removing the adjacent calorimeter hits also significantly improved the sensitivity, however the increased detection efficiency vs the minimum angle cut is outweighed by the higher background count, which continues to encompass a small number of external  $^{208}\text{Tl}$  events. Removing adjacent calorimeter events does not reduce the internal and external backgrounds at the same rate as the minimum angle cut, resulting in a higher background count. Applying the  $^{208}\text{Tl}$  energy separation optimization to the MC data reduces the total backgrounds from all sources, however the detection efficiency of  $0\nu\beta\beta$  is also reduced to roughly 60% of the original value. Critically, the energy separation cut fails to remove the majority of the remaining external  $^{208}\text{Tl}$ .

### 7.1.6 Window Region Optimization

Throughout this work, the region of interest for  $^{82}\text{Se}$  neutrinoless was stated as 2.8-3.2 MeV as a consequence of the 3 MeV  $^{82}\text{Se}$  decay energy. However it is possible to fine tune this window region to maximise the expected sensitivity. To optimize the ROI window, the lower end of the ROI was shifted from 2.8 MeV to 2.6 MeV in increments of 0.05 MeV and at the same time the upper limit was shifted from 3.2 MeV to 3 MeV. With each changing ROI, the sensitivity was calculated after applying all cuts as well as the additional minimum angle optimization cut, which produced the highest sensitivity as shown in the previous section. Additionally the window optimization was only complete for the no field scenario. \*\*\* subject to change \*\*\*.

From the table above, the energy region shown to have the highest sensitivity is the 2.7-3.1 MeV region. This is mostly a result of the much greater detection efficiency for  $0\nu\beta\beta$  at this lower energy region whilst still suppressing the background contamination, in particular, from the problematic external  $^{208}\text{Tl}$ . The peak of the  $0\nu\beta\beta$  spectrum is between 2.7-3 MeV, however after 3 MeV number of successfully reconstructed events rapidly drops off and so shifting the ROI closer to 2.7 MeV increased the total number of reconstructed  $0\nu\beta\beta$  events in the energy region without equally increasing the number of expected backgrounds.

Below the 2.7 - 3.1 energy region, the increase in backgrounds is largely a result of an increase in the number of internal  $^{214}\text{Bi}$  events as the contamination level of internal  $^{208}\text{Tl}$  remains stable. Similar to  $0\nu\beta\beta$ , the top end of the energy distribution is within the 2.8 - 3.2 MeV region (figure

Region of interest MeV	Signal Efficiency	Expected Backgrounds	Sensitivity $\times 10^{24}$ yr.
2.80 - 3.20	0.0666	$1.890 \pm 3.59\%$	2.289
2.75 - 3.15	0.0989	$3.279 \pm 8.29\%$	2.581
2.70 - 3.10	0.1261	$6.201 \pm 7.08\%$	2.393
2.65 - 3.05	0.1464	$11.677 \pm 5.19\%$	2.024
2.60 - 3.00	0.1609	$24.22 \pm 3.69\%$	1.545

Table 18: Signal detection efficiency, number of expected events and sensitivity to  $0\nu\beta\beta$  for different regions of interest in the range from 2.6 to 3.2 MeV. Values provided are for the no field scenario after the additional minimum angle optimization.

??) and so by reducing the lower limit of the region of interest the number of  $^{214}\text{Bi}$  backgrounds increases significantly. Whereas for internal  $^{208}\text{Tl}$ , the number of backgrounds around the original region of interest remains constant and so by moving the ROI to lower energies the contribution from internal  $^{208}\text{Tl}$  remains steady.

ROI MeV	No. Of Expected Events			
	Internal $^{208}\text{Tl}$	Internal $^{214}\text{Bi}$	External $^{208}\text{Tl}$	$2\nu\beta\beta$
2.80 - 3.20	$0.774 \pm 2.40\%$	$1.036 \pm 6.10\%$	0	$0.02 \pm 70.71\%$
2.75 - 3.15	$0.789 \pm 2.33\%$	$1.757 \pm 4.71\%$	$0.214 \pm 100\%$	$0.600 \pm 28.87\%$
2.70 - 3.10	$0.788 \pm 2.33\%$	$2.894 \pm 3.67\%$	$0.427 \pm 70.71\%$	$2.249 \pm 14.91\%$
2.65 - 3.05	$0.779 \pm 2.35\%$	$4.498 \pm 2.94\%$	$0.427 \pm 70.71\%$	$7.247 \pm 8.30\%$
2.60 - 3.00	$0.776 \pm 2.35\%$	$6.602 \pm 2.43\%$	$0.214 \pm 100\%$	$20.341 \pm 4.96\%$

Table 19: Number of expected events for the most significant backgrounds as a with changing ROI

In the 2.8-3.2 MeV there is no external  $^{208}\text{Tl}$  contribution, but when reducing the energy limits of the window a smaller number of external  $^{208}\text{Tl}$  events ( $<2$ ) were found although they are completely drowned out by the internal background contributions.

From the window or region of interest optimization, the energy window giving the greatest sensitivity to  $^{82}\text{Se}$  neutrinoless double beta decay is the region between 2.7 and 3.1 MeV. Predominantly,

this is the case because below this region, the increase in background, particularly  $^{214}\text{Bi}$ , is no longer offset by the increase in the signal detection efficiency from moving the energy window closer to the bulk of the signal energy spectrum. Below 2.6 MeV, the energy window no longer encapsulates the decay energy of  $^{82}\text{Se}$   $0\nu\beta\beta$ . As mentioned previously, one of the benefits of using  $^{82}\text{Se}$  as a double beta decay isotope, is that the relatively high decay energy removes a lot of the lower energy backgrounds that may plight lower energy double beta decay searches.

Simultaneously, the width of the window was also subject to change and the sensitivity measured. Using tables ?? and ??, the minimum energy was set to 2.7 MeV and the ROI ranged from 0.15 to 0.5 MeV. As shown in table ??, below 2.7 MeV the contribution from  $2\nu\beta\beta$  begins to rapidly increase and becomes the dominant background. 0.15 MeV was selected as the narrowest ROI as a result of the calorimeter resolution, which is approximately 6% at the  $^{82}\text{Se}$  decay energy. The results of the different ROI widths are shown in table ??.

Region of interest MeV	Signal Efficiency	Expected Backgrounds	Sensitivity $\times 10^{24}$ yr.
2.70 - 3.20	0.1261	$6.396 \pm -\%$	2.401
2.70 - 3.15	0.1261	$6.298 \pm -\%$	2.429
2.70 - 3.10	0.1261	$6.201 \pm -\%$	2.448
2.70 - 3.05	0.1261	$6.110 \pm -\%$	2.466
2.70 - 3.00	0.1257	$5.987 \pm -\%$	2.483
2.70 - 2.95	0.1234	$5.801 \pm -\%$	2.476
2.70 - 2.90	0.1141	$5.557 \pm -\%$	2.340
2.70 - 2.85	0.0924	$5.143 \pm -\%$	1.969

Table 20: Signal detection efficiency, number of expected events and sensitivity to  $0\nu\beta\beta$  for different regions of interest in the range from 2.6 to 3.2 MeV. Values provided are for the no field scenario after the additional minimum angle optimization.

Above 3.05 MeV the increase in signal detection is minimal, whereas there is a small increase in the background count from internal  $^{208}\text{Tl}$ . Regardless, the sensitivity remains relatively stable above 2.70 to 3.00 MeV. Below the 3.00 MeV upper limit, the signal efficiency drops faster than the expected backgrounds resulting in a decrease in sensitivity. Using the data shown in tables ??-??, the optimal lower limit is around 2.70 MeV, below which the background count of  $2\nu\beta\beta$  and  $^{214}\text{Bi}$  exponentially increase. The upper limit is less prone to variations in sensitivity as the majority of the signal events are found below 3.05 MeV and increasing the upper limit of the ROI merely increases the internal  $^{208}\text{Tl}$  contamination.

### 7.1.7 Final Sensitivities For The Three Magnetic Fields

Three methods, Feldman-Cousins, Helene and MDA.

# Chapter 8

## Conclusion

Conclusion

A

# References

- [1] R. Davis, *A Review of the Homestake Solar Neutrino Experiment*, **Prog. Part. Nucl. Phys.**, **Vol. 32 (1994) 13-32**.
- [2] SNO Collaboration, A. Bellerive et al., *The Sudbury Neutrino Observatory*, **Nuclear Physics B (2016) arXiv:1602.02469v2 [nucl-ex]**.
- [3] S. Agostinelli, et al., *Geant4—a simulation toolkit*, **Nuclear Instruments and Methods in Physics Research A 506 (2003) 250–303**.
- [4] O. Helene, *Upper Limit of Peak Area*, **Nuclear Instruments and Methods in Physics 212 (1983) 319**.
- [5] G. J. Feldman, R. D. Cousins, *A Unified Approach to the Classical Statistical Analysis of Small Signals*, **Phys.Rev.D57:3873-3889 (1998) arXiv:physics/9711021v2 [physics.data-an]**
- [6] D. Boursette, *Neutrino physics with SoLid and SuperNEMO experiments.*, **High Energy Physics - Experiment [hep-ex]**. Université Paris-Saclay, 2018. English.
- [7] D. L. Hall, *Development of a simulation model for the SuperNEMO tracker module*, PhD thesis, University of Manchester, 2012.`.text`
- [8] R. Arnold, et al., *Possible background reductions in double beta decay experiments*, **Nuclear Instruments and Methods in Physics Research A 503 (2003) 649-657**.